CONDUCTIVITY MEASUREMENTS OF SINGLE DNA MOLECULES USING CONDUCTIVE- ATOMIC FORCE MICROSCOPY

by

Shun Lu

B.Sc., Physics, Wuhan University, 2003

THESIS SUBMITTED IN PARTIAL FULFILLMENT

OF THE REQUIREMENTS FOR THE DEGREE OF

MASTER OF SCIENCE

IN THE DEPARTMENT

OF

PHYSICS

SIMON FRASER UNIVERSITY

Fall 2006

APPROVAL

Name: Shun Lu

Degree: Master of Science

Title of thesis: Conductivity Measurements of Single DNA Molecules Using Conductive- Atomic Force Microscopy

Examining Committee: George Kirczenow
Professor of Physics, SFU (Chair)

John Bechhoefer (Senior Supervisor)
Professor of Physics, SFU

Hogan(Hua-zhong) Yu (Supervisor)
Associate Professor of Chemistry, SFU

Eldon Emberly (Supervisor)
Assistant Professor of Physics, SFU

Patricia Mooney (Internal Examiner)
Professor of Physics, SFU

Date Approved: December 5, 2006

Abstract

DNA molecules possess structure and molecular recognition properties that make them excellent candidates for molecular electronics. Understanding the mechanism of charge transport along DNA is an essential step for developing DNA-based molecular electronics. In the experiments reported in this thesis, we applied the method developed by Cui *et al.* (self-assembled nano-junctions and conductive-AFM) to study DNA molecules. Double-stranded DNA (dsDNA) molecules were integrated between a gold substrate and gold nanoparticles (GNPs). We then use conductive-atomic force microscopy to study the conductivity of single dsDNA molecules labeled by the GNPs. We conclude that DNA molecules have semi-conductor characteristics, with a large band gap. In addition, we showed that an observed asymmetry of the current-voltage curves does not result from the DNA sequence. We propose instead a mechanism of conformation switching between "standing" and "lying" states of dsDNA molecules that arises because of the intrinsic negative charges on DNA strands.

This thesis is dedicated in memory of my grandparents.

Acknowledgments

First, I would thank to my supervisor Dr. John Bechhoefer for his help during the research process. I am really impressed not only by his knowledge but also by his enthusiasm in science, which would inspire me in the following study and research. I really appreciate his patient instruction and assistance in my thesis writing. I would also like to thank my supervisory committee members–Dr. Hogan Yu and Dr. Eldon Emberly for their assistance in my research and the suggestions for giving presentations. Special thanks to Dr. Patricia Mooney for her kindness giving us the accession to her fantastic AFM machine, which made most of the DNA measurements possible.

I also want to express my appreciation to Dr. Peter Williams, Dr. Yuekan Jiao, and Dr. Connie Roth for their previous work and results, especially for their instruction on AFM measurements. Meanwhile, I owe many thanks to co-workers in Dr. Yu's Lab. I want to thank Joe Wang for his diligent work on making DNA samples and the measurements. I learned many helpful chemical knowledges and ideas of this project during the discussion with him. Thanks to Dr. Bixia Ge for her marvelous work on the first successful DNA samples. I would also thank to the cooperation with Marcus Kuikka and Navanita Sarma on alkane and DNA molecules. Moreover, thanks also to Bryan Gormann and Ken Myrtle for their technical assistance in the thermal evaporation apparatus. Philip Grant in our lab also helped me a lot in using scanning tunneling microscopy to characterize the gold surfaces. I want to thank Margaret van Soest for her kind assistance with my defense too.

Thanks also to my friends at SFU for the fun in beautiful Vancouver. I would always remember the encouragement from my parents and twin-brother. At last, I would like thank my wife Quan He for her strong support during my research and life over the long distance.

Contents

List of Figures

Chapter 1

Introduction

Molecular electronics is a new approach to miniaturizing electronics components using the properties of individual molecules to perform the functions of traditional components (wires, diodes, transistors, etc.). This project is motivated by the idea of molecular electronics, which has been proposed as a "bottom up" approach to creating electronic components in nanometer scale. DNA can provide a pathway for charge transport because of the formation of π-stacking of base pairs in its double-helix structure. Our goal for the project in this thesis is to measure the conductance of single DNA molecules using conductive-atomic force microscopy (c-AFM). In Chapter 2, first, I will briefly describe the emergence of molecular electronics, the bottom-up approach, and the potential advantages that may come from such efforts. Then I will discuss materials that have been proposed to be candidates for molecular electronics, especially DNA molecules. Different mechanisms for charge transport are discussed in order to give perspective on the long-distance charge transfer in DNA molecules.

The study of single-molecule conductivity has been made possible by advances in nanotechnology. In Chapter 3, I will briefly discuss the different techniques used for measuring the electrical conductivity of single-molecules. These include the nanoelectrode-gap method, the self-assembled nanojunction method, and the mechanical break-junction method. Many of these techniques have already been applied to the study of electrical properties of DNA. In different experiments, researchers have found that DNA behaves as a conductor, a semiconductor, or an insulator. I will review these experiments and try to reconcile these contradictory results, showing how experimental details such as DNA base

sequence, length, counterions, electrode contact, and so on, can affect DNA conductivity.

Inspired by the reproducible measurements of single-alkane-molecule conductivity done by Cui *et al.*, we decided to use the self-assembled nanojunction method to study DNA molecules with c-AFM. In Chapter 4, I will first describe the procedures involved in sample preparation for this method, including the preparation of atomically flat gold substrates, formation of self-assembled monolayers, and labeling with gold nanoparticles. Then, I will discuss the various instruments we use, such as the thermal evaporator, scanning tunneling microscope (STM), and atomic force microscope (AFM). Since AFM is the tool we use for conductivity measurements, I will explain more specifically its working modes and other techniques (tip-bias scanning, current-voltage curve, and force-distance curve).

In Chapter 5, I will discuss the formation of atomically flat Au (111) films. We consider factors such as the mica substrate temperature, annealing, and contamination particles. Next, we examine the original system of Cui *et al.* (octanedithiol) to confirm their results. Finally, we present our results on dsDNA molecules including the thickness of ssDNA monolayer, topography of the GNPs-dsDNA-Au sample, current image obtained from tip-bias scanning, and the IV curves on GNPs. We also show that the asymmetry of IV curves is not from the DNA sequence and is possibly from a switching mechanism due to the interactions between intrinsic negative charges on DNA strands and induced charges on gold electrodes. Finally, I summarize the experimental results and give some suggestions for future work in Chapter 6.

Chapter 2

Molecular Electronics

In the semiconductor industry, the number of transistors on an integrated circuit has been doubling every 24 months for over 40 years, a fact which is known as Moore's Law [1]. However, this trend is thought not to be further sustainable using standard lithographic methods. The idea of molecular electronics—using a "bottom-up" approach— has been proposed as a new approach to solving this problem. In this chapter, I will first describe the emergence of molecular electronics, the bottom-up approach for fabricating molecular electronics and discuss its potential advantages. Then I will introduce several "candidates" for molecular electronics, such as carbon nanotubes, self-assembled monolayers, and DNA molecules. The structures of these candidate molecules will be also given, especially for the DNA molecules that are the subject of this thesis. Finally, I will discuss the charge-transport mechanisms present in molecules, such as coherent tunneling, "diffusive" tunneling, and thermal hopping. These will give the reader a better understanding of the possible mechanism for long-distance charge transfer in DNA molecules.

2.1 Emergence of molecular electronics

The electronics industry has been driven by the desire to fabricate smaller and more components (wires, resistors, capacitors and transistors) on a single chip. Until now, miniaturization in electronics has been achieved by the "top-down" approach of lithography. However, the lithographic process for miniaturizing of circuits is limited by technological difficulties to resolutions of tens of nanometers [2]. As of 2006, features of 32 nm have

been demonstrated in photolithography [3], and chips with 65 nm features are commercially available [4]. Meanwhile, as the number of components in a single chip increases, the amount of switching increases power dissipation [5]. Moreover, when the dimension of components is scaled down to the nanometer range, the valence and conduction bands break up into discrete energy levels, which changes the basic electron-transport mechanisms in circuits. Thus developing conceptually new devices is necessary to overcome the limitations of the top-down approach to fabricating semiconductor electronic devices.

Richard Feynman's 1959 lecture [7] has inspired efforts to replace the top-down approach to fabricate circuits components by a different, bottom-up approach that seeks to create electronic components out of individual atoms and molecules. In 1974, Aviram and Ratner took the first step towards "molecular electronics" when they predicted that single molecules with a donor-spacer-acceptor structure would show rectifying properties when connected between two electrodes [8]. Since then, molecular electronics has become one of the most active research fields, benefiting from the nanotechnology boom created by physicists, chemists, engineers, and other researchers over the past thirty years. Single or small groups of molecules have been integrated in device-based structures, which work as the fundamental units for electronic components such as wires, switches, memory and gain elements [9–11]. The naturally identical sizes and electronic levels of the molecules enable single molecules to be small building blocks for devices. Molecular electronics is totally a different strategy compared to the traditional top-down approach, which begins with wafers and creates progressively smaller components using lithography techniques. Molecular electronics, by contrast, starts from the smallest unit of molecules to construct functional devices using self-assembly [12].

2.2 Bottom-up approach

Self-assembly is the "autonomous organization of components into patterns or structures without human intervention" [13]. In fact, Nature shows a strong preference for spontaneously building up molecular assemblies. Nature efficiently builds structures by self-organizing a diverse range of small fabrication units into refined structures, materials, and molecular machines with a remarkable precision, flexibility, and error-correction capacity. Examples include cell membranes, enzymes, and DNA [14]. The goal of the bottom-up

approach is to mimic nature's building process using various kinds of self-assembly techniques. These approaches may be classified as being either chemical or biological.

The chemical approaches apply the rules of bonding and kinetics for chemical objects to form stable and useful structures. Most of the current self-assembly methods produce 2-dimensional surfaces or interfaces. For example, thiol (SH) bonds attached to molecular groups are used to form a self-assembled monolayer (SAM) on metal surfaces with desired surface properties [15]. Langmuir-Blodgett film deposition, organizing colloids into arrays and crystals, and liquid crystals are other processes incorporating chemical (and physical) self-assembly [16]. Meanwhile, the biological approach depends on the selectivity and recognition properties of biological bonds at the molecular level. Among the best-known examples are antibody-antigen interactions and complementary DNA strands. These interactions can be used to construct macroscopic materials with special structures by self-assembly [17, 18].

Self-assembly processes enable one to produce functional nanostructures from organic or inorganic molecules with low cost, high efficiency, and low power dissipation. The ability to show specific recognition enables some molecules to have interesting electronic functions. One can also design and realize new materials with different electrical properties, using highly developed molecular-synthesis techniques [19]. Thus, the bottom-up approach may have a significant impact in the future as a new fabrication method.

2.3 Candidates for molecular electronics

In the past few years, a variety of organic or inorganic molecules has been considered as candidates for molecular electronics because of their unique chemical and electrical properties [20]. The study of molecules forming donor-acceptor system has been greatly stimulated by advances in the fabrication of metallic electrodes with nanometer-scale separation. Two-terminal conductance measurements on single molecules have been achieved by scanning probe microscopy [21, 23]. Moreover, reliable two- or three-terminal molecular devices have also been demonstrated [24, 25]. For example, carbon nanotubes have been fabricated into transistors and simple logic circuits [26, 27]. In another approach, DNA (deoxyribonucleic acid) has recently drawn more and more attention as a candidate for a molecular wire, since the base-pair stacking in DNA's double helix structure is thought to

provide a possible pathway for charge transport. DNA has excellent recognition and self-assembly ability properties because of the complementary nature of its base pairs. Thus, DNA may have applications to molecular electronics, in the bottom-up approach. The electrical-conductivity properties of DNA molecules are the subject of this thesis.

2.3.1 Carbon nanotube electronics

Carbon nanotubes (CNT) were first fabricated by Iijima in 1993 [28]. They are tiny hollow cylinders composed of either a single wall or multiple walls, with concentric layers of carbon atoms in a hexagon lattice arrangement [25]. The single-walled nanotube (SWCNT) has a typical diameter around 1-2 nm and a length that can be several micrometers. SWCNTs can be thought of as a piece of rolled-up graphene with a hexagonal honeycomb lattice. Depending on its lattice structure, SWCNTs can be metallic or semiconducting. In one experiment, Dekker *et al.* positioned a semiconducting CNT across two Au electrodes on a SiO_2 substrate, with a doped Si back-gate [29]. They demonstrated the first carbon nanotube field-effect transistor (CNTFETs), where the nanotube was switched from conducting to insulating state after a voltage was applied to the back-gate . Using CNTFETs, Derycke *et al.* developed a CMOS-like voltage inverter as a logic NOT gate in 2001 [26]. Thus, CNTs are promising building blocks for molecular electronics, with advantages of simple one-dimensional charge transport, chemical-controlled fabrication, and controllable metallic or semiconducting electrical properties.

2.3.2 Self-assembled monolayers (SAMs)

Self-assembled monolayers are good examples of molecular electronics made using the bottom-up approach. SAMs are ordered surface structures formed by the molecules adsorbed to a solid substrate through functional groups on one end [30]. When a substrate (for example, gold or silver films) is exposed to a solution or vapor containing active molecules, a SAM can form on the substrate, with the molecules at a preferred orientation angle with respect to the surface (Fig. 2.1). In this process, the self-assembling system attempts to reach the global free-energy minimum. The bonding process is a chemical reaction between the molecule's active head group and the substrate. In the most commonly used case, molecules with a thiol (-SH) end group bond to a Au surface through a sulfur-gold bond.

Minimization of the free energy also means that the system can eliminate defects by itself. This error-correction mechanism makes the formation of SAMs attractive for molecular electronics.

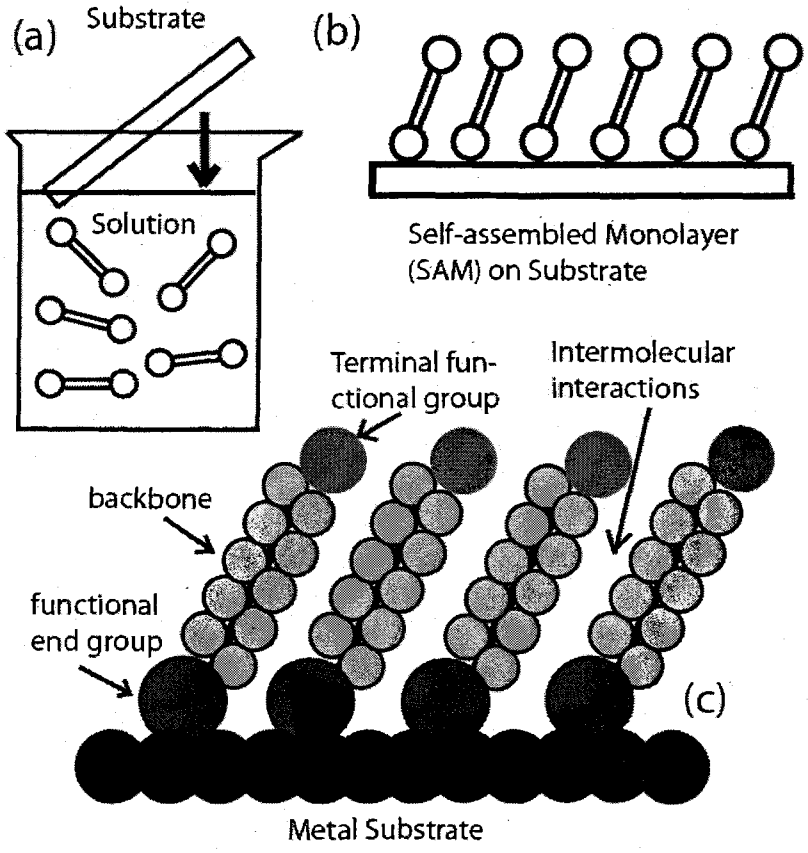

Figure 2.1: Schematic diagram of the formation of a self-assembled monolayer on a metal substrate.

SAMs can be used as either active or passive components for charge transport. Robertson *et al.* used SAMs to act as a stable switch by changing the molecular conformation [15]. The relative angle between two benzene rings in Au/Ti/ethyl-substituted 4,4′-di (phenylene-thynylene) -benzothiolate/Au junctions has a temperature-dependent transition from conductor to insulator. Thus, a SAM of this molecule can work as an active transistor. Meanwhile, the passive role of SAMs is also useful for the study of molecular electronics. To investigate the electrical properties of single molecules, one can insert the molecules into

a non-conductive SAM formed by another kind of molecule. The SAM not only helps the molecules of interested to stand up from the substrate but also isolates them from each other as a molecular insulator. This idea was used to make the reproducible conductivity measurements on alkanedithiol molecules by Cui *et al* [21, 22]. Moreover, it is also the basis for the conductivity measurements on single DNA molecules presented in this thesis.

2.3.3 DNA electronics

DNA (deoxyribonucleic acid), the blueprint of life, has been well-known mostly for its biological function as the repository of genetic information [31]. Its potential application in molecular electronics has also captured the attention of physicists, chemists, and biologists [18, 32]. A single DNA strand is composed of a polyanionic sugar-phosphate backbone, linking together four different kinds of bases adenine (A), thymine (T), guanine (G), and cytosine (C). The DNA double helix is formed when two single strands combine together if they are complementary to each other, where A-T and G-C base pairs are formed by hydrogen bonds between the purines (A, G) and pyrimidines (T, C) on two strands. The helix structure is held together by hydrogen bonding between the complementary strands [33]. This double-helix structure was proposed by Watson and Crick in 1953 [34], as shown in Fig. 2.2(a).

The most important form of DNA structure is called B-DNA. B-DNA is the DNA type found in cells of living organisms and is also the structure predicted by Waston and Crick. In B-DNA, the center of the base pairs lies along the helix axis (Fig. 2.2), and the two complementary strands wind around the helix axis forming a right-handed spiral. The distance between adjacent base pairs is about 0.34 nm, and there are about 10 base pairs in each turn of the helix. Thus, the average angle between two successive base pairs is about 36° [35]. Since the purine and pyrimidine are consisted of aromatic rings that form π-bonding, the base-pairs between the backbones can form in a structure called "π-stacking," where the electrons in the π-bonds are not tight bonded to specific bases but delocalized. The π-π interactions caused by the overlap of electron clouds between adjacent base pairs can stabilize the helix structure, and also provide a pathway for the charge transport in the DNA helix structure. Thus, DNA has been proposed to be a one-dimensional conductor that is used as a molecular wire.

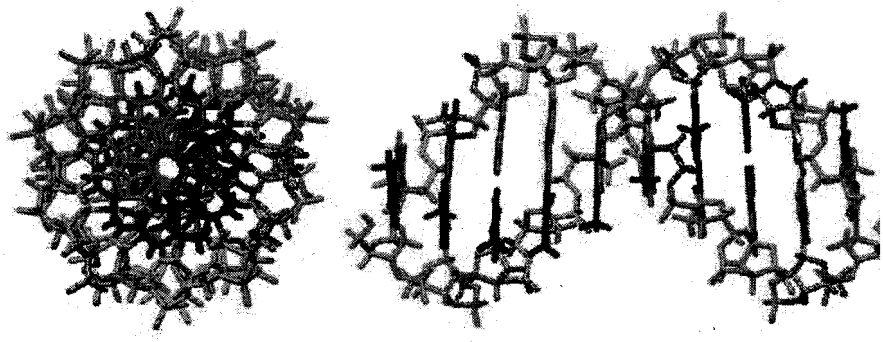

Figure 2.2: Top and side view of the structure of B-DNA. (from [35], copyright 2006, with permission from Elsevier.)

The highly developed DNA biotechnology enables one to form DNA nano-structures or nano-machine using single-stranded DNA with programmed base sequences [18, 36]. Seeman *et al.* demonstrated a two-dimensional DNA array, and cubic structures can also be self-assembled from suitable DNA units [18]. These structures of DNA have potential to form nano-scale devices or materials. We need to fully understand the electrical properties of DNA molecules if there is to be any hope of making DNA electronics. A variety of measurements has been done to study the charge transport in DNA molecules [32, 37–47]. As we shall see these measurements may be grouped into ones involving long DNA molecules and these involving short DNA molecules. Among the long molecules, a widely used DNA sequence is that of λ-DNA. Its length is about 16 μm, consisting of about 50,000 base pairs, and it is from the bacterial phage λ virus [35]. Among the short molecules, one often sees fragments of poly(dG)· poly(dC) or poly(dA) · poly(dT). The sequence is homogeneous and has only two kinds of nucleotides (G and C, or A and T) on both strands of the helix structure.

2.4 Charge transport in molecules

To understand the electronic properties of molecules better, we need to know the mechanism of charge transport in these molecules. This topic has been widely investigated in the context of donor-bridge-acceptor (DBA) molecular complexes [48]. The donor can be part of the molecule or metal electrode and donates electrons. Meanwhile, the acceptor, which

can also be part of the molecule or metal electrode, accepts electrons. In the DBA system, the donor and acceptor have the lowest unoccupied energy states and are separated by a bridging molecule that has different-energy molecular orbitals. Several mechanisms, such as coherent tunneling, incoherent tunneling, and hopping, have been proposed to explain the charge transport in DBA system [48]. Before discussing the actual charge transport in molecules, we first introduce the Landauer formula, which describes contact resistance arising from the interface between the molecule and the contact electrodes.

2.4.1 Contact resistance and the Landauer formula

Consider a conductor in contact with two large metal pads. The conductance of a macroscopic object obeys $G = \sigma A/L$, where σ is the conductivity , L the length, and A the cross-section area. If this ohmic scaling relation were to hold as the length of the conductor is decreased to nanoscopic scales, we would expect the conductance to increase indefinitely. The conductance would be infinity if the length of conductor were zero, (point contact). However, experiments [23, 37] show that there is a minimum that the measured resistance approaches as the size of this conductor decreases to zero, making a gold-gold point contact. The conductance of such a point contact is described by the Landauer formula,

$$G = \frac{2e^2}{h} \sum_{i=1}^{N} T_i, \tag{2.1}$$

where N is the number of conduction channels and T_i is the transmission coefficient for the i^{th} channel in the molecular wire [49]. T_i represents the probability that an electron coming through one of the leads will be transmitted to the other side of the constriction, traveling through the i^{th} channel. If the length of metal conduction channel is much smaller the mean free path of an electron in a metal ($\approx$ 10 nm) [49], it is reasonable to assume the scattering is elastic and T_i=1 for all channels. Then the Landauer formula takes the form $G = N(2e^2/h)$, where N is the total number of transmission channels. We can see the conductance is an integer multiple of a fundamental conductance $G_0 = 2e^2/h$. Conductance quantization has been observed in break-junctions between a Au surface and a gold STM tip by Tao *et al.* [23,37]. However, when the conductor is not ideal and inelastic scattering occurs, $T_i < 1$ for the transport process, and the contact has a larger resistance than the gold-gold contact resistance. This is the case for a contact between a metal electrode and other molecules (eg.

Au-S bond). In any case, the Landauer formula is widely used to study charge transport in mesoscopic systems [49, 50].

2.4.2 Coherent tunneling

The scattering of waves or carriers has two contributions: elastic scattering (coherent tunneling) and inelastic scattering (incoherent tunneling) [51]. In the case of elastic scattering, carriers will have a phase that has a relationship to the phase before scattering. In the case of inelastic scattering, the carriers will have a phase unrelated to that of the incident carriers. Coherent tunneling happens for a narrow barrier. When an electron transverses a barrier with a given height and thickness, one can use quantum mechanics to predict the probability for the electron to tunnel through the barrier and keep its phase (Fig. 2.3(a)). This process is called coherent tunneling, and the tunneling current density J is given by the Simmons relation [52].

$$J = \frac{q^2 V}{h^2 d}\sqrt{2m\Phi}\exp\left[\frac{-4\pi d}{h}\sqrt{2m\Phi}\right], \tag{2.2}$$

where q = electron charge, V = applied voltage, h =Plank's constant, m =electron mass, Φ = barrier height, and d = barrier thickness.

From this equation, we can see the coherent tunneling current decreases exponentially with the thickness of barrier, which is the length of molecule in the case of DBA system. The Simmons equation is usually simplified to:

$$J = Be^{-\beta d}, \tag{2.3}$$

where β is the decay constant, proportional to $\sqrt{\phi}$, with units of inverse angstroms, and B is constant. During this process, the charge wavefunction does not lose its phase coherence (coherent tunneling). If the system size is increased or if there is coupling to the environment, then the tunneling becomes incoherent: the wavefunction will lose its phase coherence after charge tunnels through a barrier.

From experiments with a vacuum gap between two electrodes with work functions of 5.0 eV, β is predicted to be 2.3 Å^{-1} by the Simmons equation [53]. However, the observed values of β for molecular junctions are usually around 1.0 Å^{-1} [54, 55]. This is a huge difference since β appears in the decay exponent. A smaller β means that the electron

transport rate is far larger. The explanation for the discrepancy is that there is another, "superexchange" mechanism where the molecule's electronic structure increases the electron transport rate in the molecule [53]. In other words, the tunneling is more efficient through molecular bonds than through bare space. Thus, superexchange is usually referred to as coherent tunneling in molecules.

2.4.3 Incoherent tunneling

Even for superexchange, tunneling is only effective for very short distances of less than a nm. However, electron transport in DNA helix over 4 nm was found in the 1990s [56]. The observations suggest that there must be other mechanisms for the charge transport. Incoherent, or "diffusive," tunneling was proposed to explain the electron's long-distance motion in molecules. In this model, the molecules are characterized by a series of sites forming potential wells. Unlike the unistep process of superexchange, each potential causes the charge to localize for a finite time, which disturbs the phase of the electron. After each tunneling process, the charge wavefunction loses its coherence through dephasing processes, such as scattering by molecular vibrations [35]. The process can be viewed as a series of discrete steps and is thus a multistep process, as shown in Fig. 2.3(b). Since the path of electrons between different sites in the molecule follows a random walk, it is also called diffusive tunneling. Incoherent tunneling does not depend on the length of molecules as strongly as coherent tunneling does, the length dependence of conductance goes as $1/L$ [57].

2.4.4 Thermal hopping mechanisms

Like incoherent tunneling, thermal hopping is a multistep process during which the electron traverses several energy barriers, as shown in Fig. 2.3(c). The thermal active transport is expressed in a classical form–Arrhenius equation:

$$k_{ET} = k_{ET}^{\circ} \exp\left(\frac{-E_a}{kT}\right) \tag{2.4}$$

where k_{ET} is the electron transport rate, E_a is the activation barrier, and k is the Boltzmann constant.

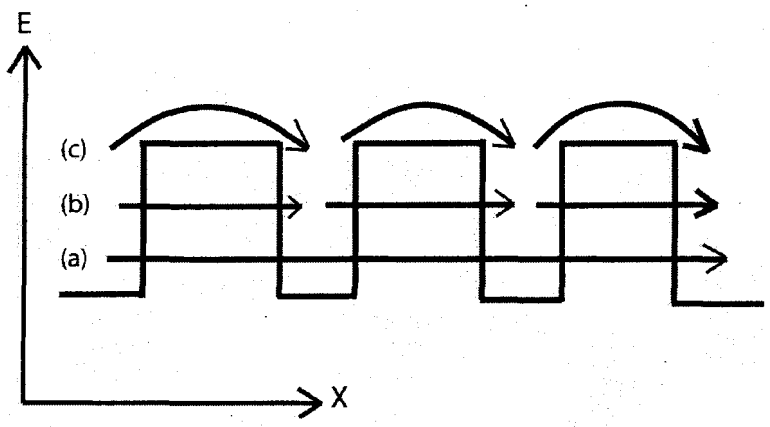

Figure 2.3: Schematic diagram of three charge-transport mechanisms in molecules containing energy barriers. (a) Coherent, or unistep, tunneling; (b) Incoherent, or diffusive, tunneling; (c) Thermal-hopping mechanism. The vertical axis represents energy E, and the horizontal axis represents the spatial position X.

From Eq. 2.4, we can see that the hopping process is temperature dependent. One important difference between incoherent tunneling and thermal hopping is the role of nuclei motion (nuclei refers to the body carrying the charge) [53]. In incoherent tunneling, electrons can tunnel through the energy barriers without nuclei motion. But charge transport only happens in the hopping mechanism when a favorable molecular configuration is (momentarily) created by nuclei motion. A series of transport events between stable sites, it does not exhibit an exponential dependence on transport length; instead, the hopping current is inversely proportional to the molecule length d. For larger length d, hopping is a more efficient way for charge transport than coherent tunneling. However, the molecules needs to be in solution in order to get favorable configurations for thermal hopping. Thus, one can expect this mechanism to be "turned off" if the configuration of the molecule is frozen, for example, by pinning it to a rigid substrate.

In experiments, DNA damage can occur under UV irradiation and in the presence of certain oxidants [58]. Since guanine (G) has the lowest ionization potential among the four DNA bases [59], it is the major target for oxidants. A guanine radical cation ($G^{+\cdot}$) will form once guanine is oxidized. Because GG and GGG sequences have lower ionization potentials than single G's [60], long-distance migration of charge transport from a guanine

radical cation ($G^{+\cdot}$) to a G-rich sequence can occur in DNA sequences, a process thought to result from a radical-cation hopping process [61]. The efficiency of the charge transport decreases dramatically as the number of A:T base pairs between $G^{+\cdot}$ and GGG increases. These $(A:T)_n$ bridges mediate the charge transfer, forming a coherent tunneling barrier. But in DNA strands where G's are located between the $G^{+\cdot}$ and GGG sequences, the efficiency of charge transport is increased. Long-distance migration can then occur, with the charge transfer a multistep hopping process [62]. More elaborate models such as ion-gated hopping of polaron-like distortions have also been proposed to explain the charge transport in DNA molecules more accurately [61].

Chapter 3

Electrical Measurement of Single Molecules

The goal of molecular electronics is the measurement and control of the electronic properties of single molecules [8]. Thus, conductivity measurements of single molecules are important not only for their fundamental interest but also for their application to molecular electronics. However, single-molecules measurements are difficult, and it was not until the late 1990s that reliable measurements of the conductance of single molecules were first achieved [63]. In this chapter, I begin by discussing different techniques used to study the electronic properties of single molecules. These include using nanoelectrode gaps fabricated by lithographic techniques, self-assembled nanojunctions probed by conductive-atomic force microscopy (c-AFM), and the break-junction method probed by scanning tunneling microscopy (STM). Next, I will briefly review the different conductivity measurements of DNA molecules, which have been done using the different techniques discussed in the first section. The experimental results from different groups vary widely, with claims of DNA conductivity that range from insulator, semiconductor, conductor, to superconductor. I will try to reconcile these different results. The subtleties and difficulties in these methods illustrate why single-DNA-molecule measurements are so difficult.

3.1 Techniques for measuring the electrical conductivity of single-molecule

Conductivity measurements of single molecules have been made possible by advances in nanotechnology. For example, electron-beam lithography and photolithography are used to fabricate nanoelectrodes, for connecting molecules into a circuit. Scanning probe microscopy (SPM) can also characterize and manipulate molecules with nanometer accuracy. Conductivity measurements of single molecules using different techniques have been published over the past 10 years [21,23,25,37,41–47,75]. However, reproducibly making single molecules physically or chemically contact two metal electrodes of mesoscopic scale is still an experimental challenge. Moreover, the electrical properties of single molecules even for the simplest molecules (e.g., alkanedithiol) are highly sensitive to changes in experimental conditions. In this section, I will briefly introduce single-molecule techniques and related experimental results. First, I will discuss the fabrication of nanoelectrodes to trap single molecules, a technique that is widely used in single-molecule measurements. Second, I will describe two other approaches using SPM that have been also very successful: forming self-assembled nanojunctions using c-AFM, and forming single molecule break-junctions using STM.

3.1.1 Nanoelectrode-gap method

Integrating single molecules into a circuit using metal electrodes is a straightforward way to perform conductivity measurements, as shown in Fig. 3.1. A gap to trap single molecules is formed either by two metal electrodes (Fig. 3.1(a)) or by a metal electrode plus a conductive SPM tip (Fig. 3.1(b)). Because of the small size of molecules, the separation of electrodes (size of gap) must be small too, preferably in the range of a few to tens of nanometers. Since such distances exceed the range of distance for direct tunneling currents, there is no parallel conduction path with respect to the conduction through molecules. Thus, this setup can measure the real electrical current through molecules. However, molecular conductivity may still depend on the measurement methods and on the environment of the samples, for example the humidity and temperature. In particular, the gap between electrodes is a critical factor for the conductivity measurements. Note that the separation of electrodes is fixed in

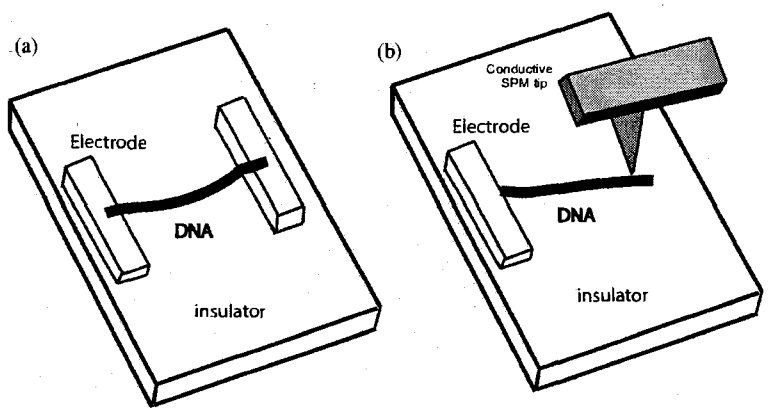

Figure 3.1: Schematic diagrams of the nano-gap-electrode method [64]. (a) single molecules are trapped between two metal electrodes; (b) single molecules are contacted by one metal electrode and a conductive SPM tip.

the case shown in Fig. 3.1(a) but can be changed by moving the SPM tip relative to the other electrode in Fig. 3.1(b).

The metal electrodes in Fig. 3.1(a) are usually fabricated by photolithography or electron-beam lithography on insulating substrates such as oxide-covered Si surfaces. Photolithography using a very short wavelength (currently 193 nm) laser source is the predominant fabrication method used in the semiconductor industry [65]. With the laser, one can transfer the pattern for electrodes from a photomask to the semiconductor substrate. Features less than 32 nm were imaged by IBM using high-index immersion lithography in 2006 [3]. Metallic electrodes with less than 1 nm separation were fabricated by Morpurgo *et al.* by combining conventional photolithography and electrochemical methods [66]. Electron-beam lithography can beat the diffraction limit of photolithography: a high energy-electron beam can produce a pattern with a line width currently 10 nm, or even smaller [67]. These two methods for fabricating electrodes can also be adapted to include backgates, which are important for the electronics industry. In contrast, the SPM-tip method (Fig. 3.1(b)) usually involves depositing a micron-size metal layer to cover one end of the molecules to form an electrode. The conductive SPM tip touches the molecules a short distance away from the metal layer and forms the other electrode. It is an easier way to integrate molecules into a circuit and is thus widely used in experiments.

3.1.2 Self-assembled nanojunctions and c-AFM

This technique, developed by Cui *et al.*, uses dithiolated molecules to form a bridge between a gold substrate and a gold nanoparticle [21]. Molecules of 1,8-octanedithiol are embedded in a self-assembled octanethiol monolayer on Au (111) using an exchange reaction [68]. The octanethiol monolayer electrically isolates the dithiolated molecules from each other. A solution of gold nanoparticles is incubated with the mixed monolayer, so that a single nanoparticle can form chemical Au-S bonds with the octanedithiol molecules. A conductive AFM tip is then brought into contact with the gold nanoparticles to measure the current. The basic idea is to form chemical bonds to the molecule of interest rather than a physical contact (e.g., when an SPM tip is pressed against the molecule in Fig. 3.1(b)). The physical contact is now between a gold-coated AFM tip and a gold nanoparticle, which will have a low resistance independent of the details of the contact. The hope is that this will be a more reliable and reproducible way of making contact to a single molecule.

In the experiments of Cui *et al.*, over 4000 individual nanoparticles were located with gold-coated conducting AFM probes in a reproducible manner with the setup shown in Fig. 3.2(a). Current-voltage (IV) curves measured on different nanoparticles were collected, and they produced five distinct families of IV curves (Fig. 3.2(b)). They found that the curves could be rescaled by a constant factor to fall on a single master cureve (Fig. 3.2(c)). Analyzing the histogram obtained for the values of the divisor X, they found sharp peaks at integer values (N=1, 2, 3, 4, and 5) (Fig. 3.2(d)). These are interpreted as corresponding to different numbers of octanedithiol molecules connected to single gold nanoparticles. These results strongly suggest that the IV curves represent the conductivity of individual or small number of molecules.

Cui *et al.* also showed that the IV curves were relatively insensitive to the force applied by the AFM probe on the nanoparticles (0–8 nN). This is an important advantage of chemically bonded contacts over non-bonded physical contacts, where the IV curves of alkanethiol ($HS(CH_2)_nCH_3$) monolayers show a strong dependence on the force applied by AFM probe [54]. This method enables one to make accurate and reproducible measurements of the conductivity of single molecules. Cui *et al.* also did similar IV measurements on other molecules such as decanethiol and dodecanethiol [22]. The fundamental curves for each molecule were used to calculate the current-decay constant, β_N, for alkane. By

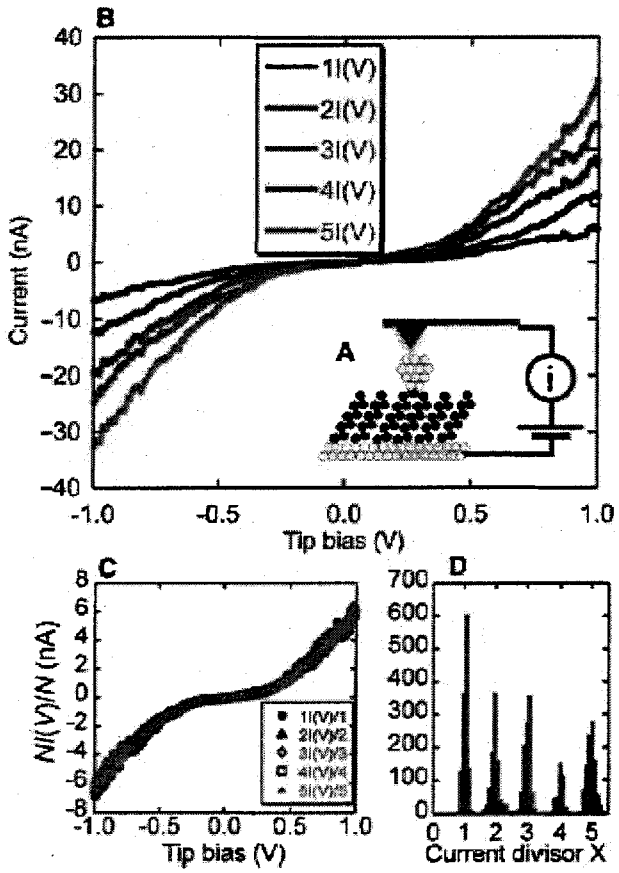

Figure 3.2: (a) Schematic representation of the experiments by Cui *et al.*, AFM tip contacts with the single octanedithiol molecules via a gold nanoparticle. (b) Current-voltage (IV) curves measured from the setup in (a). The five curves shown are representative of distinct families that are integer multiples (N =1, 2, 3, 4, and 5) of a fundamental curve. (c) Curves from (b) divided by 1, 2, 3, 4, and 5. (d) Histogram of values of a divisor, X (continuous parameter). It is sharply peaked at integer values. [Reproduced with permission from [21], copyright 2001 American Association for the Advanced of Science]

fitting the currents using $I(V) = I_0(V)\exp[-\beta_N(V)N]$ for N =8, 10, and 12, they reported that $\beta_N \approx 0.57$, which is significantly smaller than the number predicted by theory ($\beta = 1.0$) [22].

3.1.3 Mechanical break-junction using STM

The method of Cui *et al.*, while reliable, is difficult and time consuming to implement. Tao *et al.* developed a simple technique to wire individual molecules into an electronic circuit. Their idea is to repeatedly move a gold STM tip in and out of contact with a gold surface in a solution containing the molecules of interest [23, 37]. Their STM tip is specially covered by an insulating layer, except for the very end. Using this method, which can be repeated thousands of times, they form and break molecular junctions where molecules are directly connected to two gold electrodes through strong chemical bonds. As the tip is retracted from the gold surface, one observes a conductance quantization, which Tao *et al.* have attributed to the breaking of molecular junctions. In the initial stage of retraction, the junction is only a few gold atoms across, and the conductance decreases in discrete steps that are integer multiples of the conductance quantum $G_0 = 2e^2/h \approx 7.75 \times 10^{-5}\ \Omega^{-1}$ as shown in Fig. 3.3(a, b). The results implies the formation of quantum point contacts between gold tip and surface, where multiple strands of single atomic wires works as conduction channels. Landauer formula shows the number of channels determines the integer multiples of conductance. If the tip is retracted further and breaks the gold atomic chain, a new series of conductance steps appears in a lower-conductance regime. Each decreasing step corresponds to breaking a single or a few junctions formed by 4,4′ bipyridine molecules between the two gold electrodes (Fig. 3.3(c)). The histogram of conductance steps shows peaks near 0.01 G_0, 0.02 G_0, and 0.03 G_0 (Fig. 3.3(d)). The average tip displacement for these steps is 0.9 $\pm$ 0.2 nm, which is about three times longer than the value for contact quantization. A control experiment done in a solution without 4,4′ bipyridine molecules showed no conductance steps. The current just dropped exponentially (Fig. 3.3(e, f)). The result implies that the conductance steps in Fig. 3.3(c) were really from the 4,4′ bipyridine molecules. Moreover, Tao *et al.* also found the molecular conductance steps for 4,4′ bipyridine disappeared at negative potentials, where these molecules no longer bind to the gold surface. Thus, they reported that the conductance of 4,4′ bipyridine is 0.01 G_0.

Tao *et al.* also examined hexanedithiol, octanedithiol, and decanedithiol molecules. They found similar peaks in the conductance histograms of conductance steps, from which they determined that the resistances for those molecules were 10.5 ± 0.5, 51 ± 5, and 630 ± 50 MΩ, respectively. The relation $R = A \cdot \exp(\beta_N N)$ predicts that the molecular resistance increases exponentially with carbon chain length N. After fitting the data, they reported $\beta_N = 1.0 \pm 0.05$, which is consistent with theory [22]. The agreement indicates that no Coulomb-blockade effect is present in this method, where no nanoparticles was used for contact between the molecules and SPM tip, compared with the work done by Cui *et al.*

3.2 Direct electrical measurements of DNA

As discussed in Chapter 1, DNA molecules have potential applications in molecular electronics because of properties such as double-strand recognition and self-assembly. Any realistic application of DNA electronics, requires understanding the electrical properties of DNA molecules. As a matter of fact, charge transport in DNA molecules has been of interest to both chemists and physicists since the discovery of its double helix structure in 1953 [34]. Broadly, there have been two different approaches, one taken by the chemistry community and the other by the physics community.

The "solution chemistry" community usually attempts to measure electron transfer rates between a donor and an accepter as a function of the donor-acceptor distance and the interposed base sequence [70]. In this approach, one introduces a positive charge, or "hole," to the donor site of DNA. This is done either using intercalators to oxidize the DNA bases or forming radical ions on DNA bases by direct photo-induction using ultraviolet light. After the hole is injected into the structure, it then moves along the base-pair stack of the DNA strands. Later, the hole is trapped by an acceptor at some distance away, which can produce oxidative damage to that base. The oxidative site can be detected by fluorescence-quenching or by strand-cleavage techniques [62, 72]. From these experiments, chemists have inferred mechanisms of charge transfer in DNA, such as superexchange, G hopping, GA hopping, and domain hopping [62, 71, 72]. However, the data from these solution-chemistry experiments are an average over large numbers of DNA molecules. Thus, these electrochemical methods to study the charge transport in DNA molecules give only indirect information. Their advantage is that the holes are introduced into DNA structures without

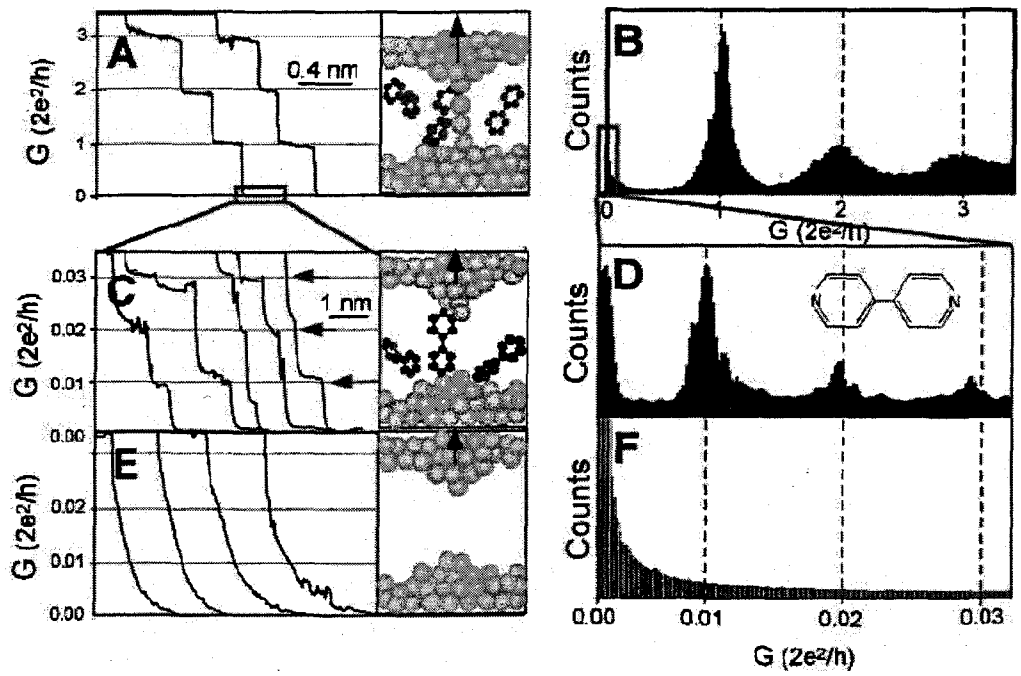

Figure 3.3: (a) Conductance between a gold STM tip and a gold substrate decreases in quantum steps near multiples of $G_0(= 2e^2/h)$ as the tip is pulled away from the substrate. (b) Corresponding conductance histogram for 1000 conductance curves in (a) shows well-defined peaks near 1 G_0, $2G_0$, and $3G_0$. (c) When the contact in (a) is completely broken, a new series of conductance steps appears if molecules such as 4,4′ bipyridine are present in the solution. These steps are arise from the formation of stable molecular junctions between the tip and the substrate electrode. (d) A conductance histogram obtained from 1000 measurements in (c) shows peak near $1\times$,$2\times$, and $3\times$ 0.01 G_0 that are ascribed to one, two, and three molecules respectively. (e and f) In the absence of molecules, no such steps or peaks are observed within the same conductance range. [Reproduced with the permission from [23]. (Copyright 2003 American Association for the Advanced of Science)]

a tunneling barrier for charges to overcome [70].

On the other hand, the "solid state" physics community aims to measure the electric current flux through DNA molecules under an external field. Using the techniques described in the last section, one can bring the DNA molecules into contact with two metal electrodes, separated by a gap of several nanometers. The current signal through DNA molecules can be measured at different external voltages to obtain a current voltage (IV) plot, which is very convenient for the study of DNA conductance. The current is usually small, because of the poor conductivity of DNA molecules. In contrast to the solution-chemistry method, solid-state methods measure more directly the conductivity of single DNA molecules. The roles of donor and acceptor are played by the metal electrodes in this method.

Since 1998, a series of direct electrical transport measurements conducted on single DNA molecules has been published, using techniques such as lithography and scanning probe microscopy (SPM). However, different groups have come to completely different conclusions: that DNA is an insulator [32, 38–40], a semiconductor [41–43], a conductor [37, 44–46], or even a proximity-induced superconductor [47]. In this section, I will discuss the details of the different experiments on DNA molecules and try to reconcile these contradictory results. Before reviewing the experiments, I want to distinguish between an insulator and a wide-band-gap semiconductor, a distinction that is important for DNA and other polymers: if a voltage is applied to a polymer and successfully induces charge transport without changing the polymer's structure and properties irreversibly, then it is a wide-gap semiconductor. If the structure is permanently altered by the voltage, then it is an insulator [70].

3.2.1 DNA is an Anderson insulator

The first direct electrical measurement of single DNA molecules was published by Braun *et al.* [32]. In their experiment, a single 16-μm-long λ-DNA molecule was stretched on a mica surface between two gold electrodes with a 12-16 μm gap. The λ-DNA was bridged between the electrodes through gold-sulfur bonds at its $3'$ ends. The existence of a single, free-hanging λ-DNA molecule was tested by fluorescence microscopy. They reported there was no observable current over a voltage range from -10 V to 10 V. Later, in 2000, de Pablo *et al.* confirmed the result of Braun *et al.* using scanning force microscopy (SFM) [39]. Two

gold electrodes with a 4 μm gap were thermally evaporated to cover 1.8-μm long-λ-DNA molecules, which were deposited on an insulating mica surface. They grounded the gold patches and brought a conductive SFM tip to mechanically contact the DNA molecules, forming another electrode. They did not detect any current even after a voltage up to 10 V was applied. In the experiments of Braun *et al.* and de Pablo *et al.*, the DNA molecules were several microns long and had nonperiodic base-pair sequences. Both features could result in static disorder and subsequent localization of molecular orbitals [73].

Motivated by this, Storm *et al.* used shorter DNA molecules (λ-DNA, as well as homogeneous poly(dG) · poly(dC) DNA) [40]. Noble-metal (platinum or gold) electrodes with spacings from 40 to 300 nm were fabricated on an insulating surface (SiO_2, mica) to bridge the 300 nm or 1.5 μm long DNA molecules ($(CH_2)_6$-SH modified). They measured no current through any of the DNA molecules. Storm *et al.* thus concluded that DNA is insulating at length scales longer than 40 nm. However, the height of DNA (0.5 nm) reported in Storm's AFM images was not the same as DNA's diameter in solution (2 nm) [73]. This suggests that the force that cause the soft DNA molecule to adhere to the substrate may also distort its structure [74]. In the distorted structure, the π-orbitals may no longer overlap, disrupting the conductivity mechanism [70]. Cai *et al.* confirmed this by showing that DNA molecules on mica, stretched by a flow, had a helical periodicity of 0.72 nm instead of the usual 0.34 nm [75].

The carbon-chain spacer (C3 or C6) between the thiol group and DNA used by Braun *et al* and Storm *et al.* may present barriers to charge transport from electrodes to DNA helix. To avoid the spacer problem, Zhang *et al.* formed thiol bonds between DNA and a gold substrate without any linker group [76]. They measured the conductance of DNA molecules at room temperature in a vacuum ($< 10^{-7}$ Torr), and concluded that DNA was an insulator with a resistivity of 10^6 Ωcm at bias voltages up to 20 V. Zhang *et al.* also showed the salt residues trapped between the DNA strands can cause a high conductance in the measurements and were a possible artifact in previous work claiming a high conductivity for DNA [45].

3.2.2 DNA is a wide-band-gap semiconductor

In a different experiment, Porath *et al.* concluded that individual 10.4-nm-long (30 base pairs), homogeneous poly(dG)·poly(dC) DNA molecules behave as a large-band-gap semiconductor [41]. They trapped single DNA molecules between two Pt nanoelectrodes by electrostatic trapping in a dilute aqueous buffer. Current-voltage (IV) curves measured on the trapped DNA oligomers show a bias voltage gap of about 2 V. Since the measurements were done in vacuum at low temperatures (down to 4 K), the possibility of ionic conduction was excluded. The DNA molecules used by Porath *et al.* have homogeneous π-stacking and are free of other uncertainties caused by twisting or bending, since the persistence length of double-stranded DNA molecules is about 50 nm at room temperature. Thus, the result of this experiment should be reliable. The observed voltage gap was interpreted as being the energy difference between the Fermi level of the Pt electrode and either the HOMO (highest occupied molecular orbital) or LUMO (lowest unoccupied molecular orbital) of the DNA molecule. Moreover, short oligomers were also used by Rakitin *et al.* to anchor free-hanging λ-DNA molecules on Au electrodes [42]. They measured a similar 1-2 V gap that originates from the short oligomers. From these experiments, we can see that short, homogeneous DNA molecules are wide-band-gap semiconductors. This is also what one might expect for short DNA molecules, if DNA has a rather large HOMO-LUMO gap ($\approx$ 4 eV) with the metal work function sitting inside the gap [73].

Watanabe *et al.* developed an innovative experiment using triple-probe atomic force microscopy (T-AFM) [43]. The T-AFM system was composed of a nanotweezer using two multiwalled cabon nanotubes (MWCNTs) and a conductive AFM using a conductive MWCNT probe. A solution of 200-nm-long DNA molecules was deposited on a SiO_2/Si(100) substrate and dried by nitrogen flow. They contacted the two MWCNTS of nanotweezer to DNA individually as drain and source. A single-walled carbon nanotube (SWCNT) was placed beside the DNA chain between source and drain as a gate (third terminal), which was contacted with the MWCNT probe of the conductive AFM. The IV curves for the DNA between drain and source with 25 nm separation at bias from 0 V to 5 V show voltage gaps decreasing from 2.0 V to 0.2 V. When the separation between the drain and source was about 5 nm, they observed staircases of Coulomb-blockade effects in the I_{ds}-V_{ds} curve, an effect not yet understood. The IV curves in this experiment were measured using carbon

nanotubes, which has a higher conductivity than that of the DNA molecules. Thus, they should have only a small effect on the IV curves of DNA molecules. However, the contacts of the nanotubes to the DNA molecules and AFM tip might have an effect on the results.

3.2.3 DNA is a conductor

In 1999, Fink *et al.* reported nearly ohmic conductance in a MΩ range, for λ-DNA molecules [44]. The conductance was comparable to that of polymers. They did the experiment using modified low-energy electron point source (LEEPS) microscopy, which can image native DNA molecules. The electron point source emitted a coherent electron beam, which had an energy between 20-300 eV. Instruments was also operated in an oil-free vacuum environment down to a pressure of 10^{-7} mbar, which can eliminate artifacts from other current paths such as ionic conduction. Ropes of λ-DNA molecules spanned 2-μm holes in gold-covered carbon foil (TEM grid), which was grounded to serve as an electrode. An additional tungsten tip was applied to contact a specific site of the DNA rope or break it. The current through the DNA rope was monitored as a potential was applied on the tip. They inferred a resistance of about 2.5 MΩ for a single 600-nm-long rope. However, their claim that the energy of electron beam from LEEPs is small enough to prevent contamination of DNA has been questioned by other groups. The claim was proved to be wrong by de Pablo *et al.* [39], who showed that there were doping effects on the DNA molecules from the electrons of LEEPS, which can induce an electrical conduction through DNA.

Direct electrical measurement of DNA was also performed by Cai *et al.* with conductive atomic force microscopy (c-AFM) at room temperature in 2000 [45]. Two different DNA molecules (poly(dA) · poly(dT), poly(dG) · poly(dC)) were separately used on freshly cleaved mica surface. Poly(dA) · poly(dT) DNA molecules forms a cross-linked network on mica, while poly(dG) · poly(dC) DNA molecules forms a uniform reticulated structure. A gold electrode was then evaporated to make contact with the DNA networks. A conductive AFM tip served as another electrode to make contact to different positions of the DNA bundles. Only noise current was detected when they put the AFM tip on mica surface without touching DNA molecules. For poly(dG) · poly(dC), linear ohmic behavior and p-type rectifying behavior were both observed when the tip was 100 nm away from the Au electrode. Meanwhile, only linear ohmic behavior was observed for poly(dA) · poly(dT)

DNA molecules, and with a much higher resistance. However, the ions (H^+, Na^+) from the buffer solution in this experiment may affect the π-stacking electric structure of DNA, as well as the charge transport.

In 2004, Xu *et al.* applied the elegant method of mechanical break-junctions using STM (Sec.3.1) to study the conductivity of single DNA molecules in aqueous solution, where the native conformation and thermal motion of the DNA is preserved [37]. They used two series of short (8, 10, and 12 bp) DNA sequences to separately form double helix structures terminated with $CH_2CH_2CH_2$-SH group at each end. The dsDNA molecules bind to a flat gold surface and a gold STM tip via strong Au-S bonds. Over 500 individual measurements of conductance steps were used to construct a conductance histogram for statistical analysis. The histogram for 8-bp dsDNA molecules showed defined peaks near integer multiples of $1.3 \times 10^{-3} G_0$. A control experiment using the same setup but in a solution without the DNA duplex showed no such conductance steps.

To obtain IV curves of a single DNA duplex, Xu *et al.* tried two different methods. The first was to construct several conductance histograms and obtain the fundamental peak at different bias voltages. The second was to stop the tip at the last conductance plateau and measure IV curves by sweeping the voltage. This corresponded to the case where a single DNA duplex bridged the gap between the tip and gold surface. The IV curves obtained in the second method agreed with those of the first method. The IV curves showed a linear ohmic behavior from -0.5 V to 0.5 V. Conductances of other DNA duplexes were also measured with the same setup. They found the conductance decreased very slowly with the length for $(GC)_n$ DNA sequences ($G \approx 1/n$), but the conductance decayed exponentially for $(AT)_m$ sequences ($G \approx A \cdot \exp(-\beta L)$, where $A = (1.3 \pm 0.1) \times 10^{-3} G_0$, $\beta = 0.43 \pm 0.01$ $Å^{-1}$). In this experiment, the DNA molecules kept their native structure and integrated into the electrodes through Au-S chemical bonds. Thus, their report is one of the most informative experiments on electrical properties of DNA molecules so far.

3.2.4 DNA is a superconductor

A unique result was reported by Kasumov *et al.* that claimed the observation of proximity-induced superconductivity of DNA in 2001 [47]. In their experiment, they sputtered 2-nm-thick carbon on a 2-nm rhenium layer deposited on a freshly cleaved mica substrate. This

resulted individual Re/C fibers up to 40 nm tall, which can serve as superconducting electrodes with a transition temperature at 1 K. The Re/C film was separated into two electrodes with a gap by a focused laser beam. 16-μm-long λ-DNA molecules were stretched between the Re/C electrodes by a flow of DNA solution. About 100-200 molecules were induced to bridge the gap between two Re/C bilayer. After the deposition of DNA, the overall resistance decreased from 1 GΩ to a few kΩ, which gave an estimate of the resistance of 300 kΩ per DNA molecule.

Using a low-powered focused laser beam to destroy some of the DNA molecules, Kasumov *et al.* prepared three samples with different numbers of DNA molecules (2-3, 10, and 40 chains). An external magnetic field was also applied on all three samples as temperature decreased from room temperature (RT) to 0.05 K. Their results showed that the resistances of all three samples increase as the temperature decreased down to 1 K. However, two samples displayed the properties of proximity-induced superconductivity (by nearby electrodes), where their resistances decreased below the superconducting transition point of Re/C electrodes at 1 K. The 2-3 chain sample, by contrast, had an increasing resistance even below 1 K, which was not the case of proximity-induced superconductivity. Kasumov's results showed that the resistance of DNA molecules does not increase with decreasing temperature. This suggested that thermal hopping is unlikely to be the mechanism for charge transport in λ-DNA. However, Kasumov's result is unique, and no similar experimental or theoretical results have been subsequently reported by this or other groups.

3.2.5 Conclusions from the DNA conductivity experiments

From all these different experiments, we can draw some conclusions about DNA conductivity. First, charge transport through short ($\leq$ 20 nm) molecules of DNA is possible. All of the measured currents were on nA scales, even up to a bias of 2 V. This is consistent with the mechanisms of coherent tunneling over a few base pairs (1 nm) and thermal hopping over a few nanometers. Second, long DNA molecules from a hundred nanometers to the μm scale are effectively insulating. De Pablo *et al.* reported the insulating behavior for 1.8 μm λ-DNA; Braun *et al.* applied 16 μm long λ-DNA molecules as non-conductive template for molecular wire; Storm *et al.* observed the absence of any electrical conduction through DNA molecules longer than 40 nm. This can be interpreted as implying that π-stacking

of base pairs in long DNA molecules is easily destroyed when the DNA conformation is distorted by the force between DNA strands and substrate. The charge transport in DNA is thus blocked because of the disturbance. Third, reports about conductive behavior of μm scale λ-DNA from Fink *et al.*, Cai *et al.*, and Yoo *et al.* raise many concerns about the experimental setups, which may possibly change the electrical properties of DNA molecules. For example, the low energy electrons of LEEPS can contaminate the DNA in the work of Fink *et al.*, and the ions from the buffer solution in the experiment of Cai *et al.* can induce another conduction channel beside the DNA molecules.

To be more specific, the uncertainties of conductivity measurements of DNA molecules originate from two different sources:

1. *Differences in DNA molecules and their environments* [73]. For example, the length of the DNA molecules can greatly influence the conductivity of DNA molecules as discussed for short DNA and λ-DNA; DNA sequences with different base pairs have different energy barriers for charge to overcome and thus have different electrical properties. Whether DNA molecules are in the form of ropes or of single molecules can also influence the results. Ions or counterions in the environment can also change pathways for charge transport in DNA molecules. Deformation of DNA molecules such as stretching will change the stacking of π-orbitals between base pairs in DNA, thus changing the resistance of the molecules. Whether the DNA molecules are free-standing or surfacebound, sample preparation, measurement conditions (humidity, thermal fluctuations in solution), and detection protocols are also important factors for the DNA conductivity measurements.

2. *The contacts between the electrodes and DNA molecules* [77]. Ideally, the contacts should be ohmic so that the measured conductivity is dominated by the DNA molecules and not by the interface. The contact is characterized by the work function of the electrode, as well as by the nature of the tunneling barrier [73]. However, it is still not clear what the DNA energy levels are, especially the DNA LUMO (lowest unoccupied molecular orbital), at an electrode/DNA junction. Moreover, it is still difficult to make a reliable and reproducible contact between single DNA molecules and metal electrodes in experiments, which is important for attaining highly reproducible data and an uncontroversial interpretation. A physical contact does not satisfy

this requirement. Chemical bonding between the electrodes and DNA molecules has been proved to form a better contact than direct physical contact. A good example is the reproducible chemical bonding of DNA molecules to a gold STM tip and gold surface via strong Au-S bonds in the work of Xu *et al.* [37].

To conclude, long DNA molecules have the conduction characteristics of insulators, while short periodic DNA molecules can be a wide-band-gap semiconductor. In early DNA conductivity experiments, the influence of DNA sequence, contacts, water, counterions, and other factors were not taken into account, which led to quite different results.

Chapter 4

Experimental Techniques

The most useful content in this thesis for future researchers may well be the detailed description of the experimental setup, sample preparation, and different measurement techniques. In this chapter, I will discuss the techniques and procedures of different aspects of the single-molecule conductivity measurements. In the sample-preparation part, the thermal evaporation of atomically flat Au (111) films on mica substrate is the important first step. I will discuss issues such as the source of mica, heating methods, temperature of the mica substrate, deposition rate and thickness, and annealing of gold films. Then I discuss briefly the preparation of alkanedithiol samples labeled with gold nanoparticles (GNPs) and double-stranded (dsDNA) samples labeled with GNPs using the self-assembled nanojunction method. These two parts were done by co-workers in Dr. Yu's Laboratory. Then I will discuss some of the associated instrumentation. Thermal evaporation was used for deposition of flat gold films; scanning tunneling microscopy for surface characterization, especially for gold surfaces; and atomic force microscopy (AFM) for the conductivity measurements on octanedithiol and dsDNA molecules. I will explain the basic principles and working modes of AFM, such as contact mode and AC mode. Different AFM techniques such as tip-bias scanning, current-voltage (IV) and Force-distance (FD) curves are also explained in detail. Hopefully, the content in this chapter will help future researchers to learn about the different aspects of these experiments.

4.1 Experimental method

As we discussed in Chapter 3, scanning probe microscopy (STM and AFM) is one of the most widely used techniques among the various approaches proposed to measure the conductivity of single molecules. The great advantage of a scanning-probe microscope is that it can perform both topographic imaging with nanometer resolution and electrical-transport measurements at the same time. It is very useful to correlate electrical properties to corresponding topographic features [12]. However, since an STM uses the tunneling-current signal to adjust the distance between sample and tip to construct the topography image, the position of the tip and the conductivity of the sample are coupled together. As a result, it is difficult to isolate the information about molecular conductivity from the STM data. Conductive AFM (c-AFM) can overcome this difficulty by using force rather than current to control the position of the tip. The c-AFM controls the position of a metal-coated tip relative to the sample by monitoring the bending of the cantilever, decoupling topographic information (probe position) from electrical conductivity data. Thus, c-AFM has an advantage over STM for research into the conductivity properties of surfaces.

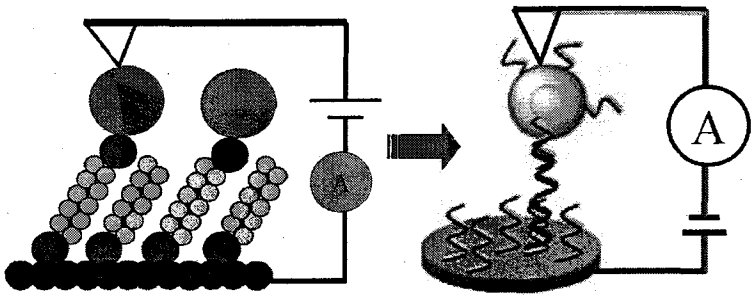

Figure 4.1: Schematic diagram for dsDNA conductivity measurement similar to the technique of Cui *et al.* using the self-assembled nano-junction method and c-AFM.

Inspired by the success of Cui *et al.* [21] and the work by Naaman *et al.* [78–80], we decided to use conductive-AFM and self-assembled nanojunctions to study the conductivity of double-stranded DNA (dsDNA) molecules, as shown in Fig. 4.1. The schematic diagram depicting a DNA sample is similar to that used for octanedithiol measurements. DsDNA molecules connect the gold surface to gold nanoparticles through Au-thiol bonds. Meanwhile, dsDNA molecules are electrically isolated from each other by the surrounding

single-stranded DNA (ssDNA) self-assembled monolayer. The ssDNA monolayer is bound to the gold surface though Au-thiol bonds. Since the dsDNA molecules are labeled by nanoparticles, they can be located by the AFM, allowing electrical measurements similar to those of Cui *et al.* and Naaman *et al.* In addition to investigating dsDNA molecules, we also repeated Cui's experiment on octanedithiol molecules, as described below.

4.2 Sample preparation

4.2.1 Au (111) and preparation of atomically flat gold substrate

Crystalline gold has a face-centered-cubic (FCC) structure, where the lattice constant is 0.408 nm, as shown in Fig. 4.2. In the unit cell, eight gold atoms sit at the eight vertices (0,0,0), (0,1,0), (1,0,0), (0,0,1), (1,1,0), (1,0,1), (0,1,1), and (1,1,1). At the same time, there are six extra atoms occupying the six center points of the faces: $(0,\frac{1}{2},\frac{1}{2})$, $(\frac{1}{2},0,\frac{1}{2})$, $(\frac{1}{2},\frac{1}{2},0)$, $(1,\frac{1}{2},\frac{1}{2})$, $(\frac{1}{2},1,\frac{1}{2})$ and $(\frac{1}{2},\frac{1}{2},1)$. The smallest distance between two gold atoms is 0.288 nm, and the FCC unit cell has (8/8+6/2=4) gold atoms in each cell [81].

The (111) plane forms a hexagonal lattice by passing through six atom positions: (0, 0, 1), (1, 0, 0), (0, 1, 0), (0, $\frac{1}{2}$, $\frac{1}{2}$), ($\frac{1}{2}$, 0, $\frac{1}{2}$) and ($\frac{1}{2}$, $\frac{1}{2}$, 0). The vector [111] is perpendicular to the (111) plane, which forms triangular facets on surface with (111) termination.

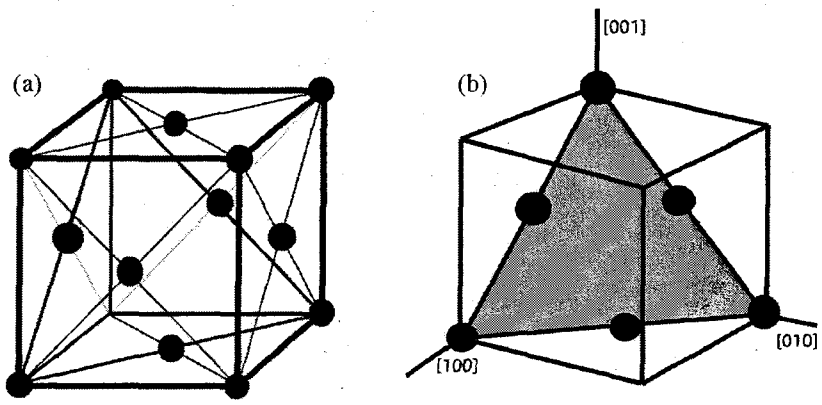

Figure 4.2: (a) Unit cell of face-centered-cubic (FCC) structure in an Au crystal. (b) Diagram of the (111) plane in the Au crystal structure.

Gold surfaces are chemically inert and highly conductive, which make them excellent

substrates for STM and other nanotechnologies. Recent work has shown that the chemical bonding between gold and thiol compounds makes Au (111) also an ideal crystalline surface for studying the formation of self-assembled monolayers (SAMs) [82]. In general, two types of gold substrates have been used: polished bulk crystals and thin films on a non-gold substrate. Single-crystal gold substrates are very expensive. Moreover, keeping the surface clean and flat after each use is difficult [83]. For all these reasons, we decided to use the thin-film geometry of gold on mica. In such a configuration, small crystallized islands with (111) termination form spontaneously [84]. In fact, epitaxial growth of Au on mica is a well-studied method for developing atomically flat gold films. There are many papers published that give protocols for the deposition of thin gold films [83–89, 91], often giving conflicting advice. One reason for this is that the published parameters often depend on apparatus-specific values that do not necessarily translate to different setups. To give but one example, we shall discuss below the important role of the substrate temperature. This is usually measured by placing a probe behind the evaporation surface. The actual temperature of the substrate is higher than the reported value. The difference depends on the thermal conductivity between different parts of the substrate, the heat losses, etc. For a fixed setup, these factors are constant and allow one to determine an optimum value, but this optimal value may differ on a different setup.

Source of mica

Mica is probably the most suitable substrate for epitaxial gold growth, as its crystal-lattice size is very close to that of gold. Mica surfaces are dominated by oxygen atoms of SiO_4, which combine with other compounds to form a mica crystal. The distance between the oxygen atoms is 0.255–0.286 nm, which is close to the 0.288 nm distance between two gold atoms in the (111) crystal structure [84]. Mica is a popular substrate choice because it is cheap and easy to cleave and cut. However, different types of mica contain different amounts and types of ions, which accounts for the distinct colors of different types of mica. DeRose *et al.* reported no obvious differences in the quality of gold films deposited on green or ruby mica [85]. However, Hwang *et al.* have claimed that mica quality (grade) can be important [86]. We evaporated gold film on two different types of mica (green and ruby mica), under the same conditions in the same set of experiments. We observed no obvious differences between the two deposited films. Thus, the type of mica was not a relevant

parameter in our work.

Heating of mica before evaporation

Mica is always cleaved before evaporation to get fresh layer for gold films. Further heating of mica in vacuum is also reported to help form Au (111) film [84, 87]. Since water and other contaminants disturb the growth and coalescence of the gold crystallites, heating mica before deposition can remove adsorbed molecules from the mica surface and water from the interior of the mica. When the mica is heated, dehydroxylation of the substrate influences the orientation and density of initial crystalline nuclei in deposition. However, the time for heating mica before gold evaporation reported in publications is quite different, ranging from 500 °C for 6 to 24 hours [85] down to roughly 200 to 300 °C for one hour [88]. We eventually found that overnight heating of mica substrates at 370 °C for about 12 hours gave good-quality gold films. We also found that we obtained films of similar quality after just 3 hours of heating. Still, the longer pumping time gave a lower vacuum (1×10^{-6} Torr vs. 7–8 $\times 10^{-6}$ Torr). Besides, it was convenient to leave the pumps on overnight.

Temperature of mica substrate during evaporation

Evaporation of gold on mica at room temperature results in gold films containing many small particles (typical grain size $\approx$ 10 nm). Heating the mica substrate during evaporation increases the size of gold grains and forms islands on the film. Heating the substrate decreases the energy difference between vapor gold atoms and substrate atoms, which aids the formation of larger crystals by increasing surface diffusion. In other words, heating provides the activation energy needed for atoms to reach their positions of minimal potential energy; thus, ordered crystal growth is achieved [87]. In the literature, a wide range of mica-substrate temperature has been reported, from 200 °C [88] to 600 °C [84]. This can be explained either by the difference between the apparatus designs for heating and temperature measurement or by cooperative effects including other evaporation parameters. In our experiment, mica substrates are fixed to an aluminum block, which is connected to the heater and an RTD temperature sensor [93]. Thus, the measured temperature refers to the back side of mica substrate. The optimal temperature for gold deposition we found is in the range of 360–380 °C, which is close to the reported temperature of 380 °C by Levlin

et al. [87] and Dishner *et al.* [89]. A temperature of 370 °C reliably produces a Au (111) surface in our experiments.

Evaporation rate and film thickness

In addition to the substrate temperature, the evaporation rate is another crucial parameter affecting the growth of atomically flat surfaces. Although a smaller evaporation rate in principle leads to larger crystals, other parameters such as the vacuum pressure can change this prediction [87]. The residual gas disturbs the crystal growth at pressures $\approx 10^{-6}$ Torr. Since our vacuum system consisted of mechanical and diffusion pumps that can only pump down the vacuum to 1×10^{-6} Torr, we need a minimum evaporation rate to compensate for the quality of the vacuum. Reports about evaporation rates from different groups again cover a large range, from less than 0.1 nm/s at 1.9×10^{-7} Torr [89] to greater than 5 nm/s at 1×10^{-5} Torr [84]. In our setup, we used a quartz-crystal located next to the mica sample holder to measure the evaporation rate and thickness with a precision of 0.1 nm/s and 0.1 nm repectively. We find that an evaporation rate smaller than 0.5 nm/s gave poor results (rough surfaces) and that the optimal rate is around 0.6-0.7 nm/s. Rates larger than 1.0 nm/s result in large vertical features and fail to give Au (111) reconstruction during annealing. On the other hand, the film thickness is not as crucial a factor as the evaporation rate. Good-quality films have been reported with thicknesses ranging from 50 nm [87] to 150 nm [84]. A larger thickness helps ensure that there are enough gold atoms to totally cover the mica substrate and helps connect the gold grains to form Au (111) during gold reconstruction. Our films were typically in the range of 85-100 nm thick.

Annealing of gold films after deposition

Annealing after deposition is the most important step in the formation of atomically flat gold surfaces. Annealing gives the gold atoms in the film enough thermal energy to move and find their lowest energy levels corresponding to their crystal structure. This reconstruction process causes grain boundaries to diffuse and merge together to form larger grains. After annealing, the gold grains form triangular facets that are a signature of the (111) surface of an FCC lattice. The film RMS roughness also decreases from 10–15 nm to 2–4 nm for 1 μm $\times$ 1μm areas. Dishner *et al.* reported that their flame-annealing technique can increase

the flat surface area by a factor of 25 relative to the unannealed film [89].

Two different successful methods of annealing have been reported: that of Dishner *et al.* [89], using a flame annealing technique, and that of Nogues *et al.* [83], using a furnace. The flame-annealing procedure suggested by Dishner *et al.* uses a Bunsen burner and butane gas. The gold film should have a size roughly equal to that of the flame so as to be covered totally by the flame. This gives the substrate a uniform temperature. The bright blue flame is passed over sample quickly until the gold film glows a faint reddish-orange color. This procedure should be done in a dark room to see the changing color of the film. In the tube-annealing procedure of Nogues *et al.*, one places the gold films into the bottom of a quartz annealing tube (15 cm long, 1.4 cm in diameter) at 650 °C for 1 minute and then 480 °C for 3 minutes. The tube is flushed with nitrogen gas during the whole process. Nogues *et al.* change the temperature from 650 °C to 480 °C by adjusting the distance between the Pyrex tube and the Bunsen flame. Since we found this hard to control, we replaced the Bunsen flame with a furnace, for better temperature control. The gold film is also contained in a Pyrex tube flushed with nitrogen. Then the tube is inserted in the furnace, which has been pre-heated to 660 °C. The gold film is heated by furnace to 660 °C for 4-5 minutes. Then we pull out the tube and let it cool down to room temperature, keeping it flushed with nitrogen. After annealing, the gold film also showed triangular facets.

Both the flame annealing and furnace annealing procedures yielded atomically flat gold surfaces. Furnace annealing is more controllable and reproducible, while flame annealing is faster and can remove contamination from the surface easily. Once mastered, flame annealing is the easier technique.

4.2.2 GNP-labeled alkanedithiol sample

As shown in Fig. 4.1, gold nanoparticles (GNPs) are used to label the single alkanedithiol or dsDNA molecules. The GNPs not only make single molecules easier to detect, they also provide a reliable chemical bond with the molecules of interest as a metal electrode in the experimental setup. Thus, the gold nanoparticle is a very important part of the self-assembled nanojunction method. We used two kinds of gold nanoparticles, with diameters of 2 nm and 10 nm. Chemical synthesis and characterization of these GNPs were done by Marcus Kuikka and Joe Wang in Dr. Yu's Lab (Department of Chemistry, Simon Fraser

Univesity). Joe was also in charge of the sample preparation of dsDNA molecules.

An octanethiol monolayer is self-assembled by immersing the fresh atomically flat gold surface in a 1-mM solution of octanethiol in toluene and letting it stand overnight. This produces a uniform, well-packed monolayer. Octanethiol molecules form a Au-S bond to the gold substrate, as shown in Fig. 4.3(a). The sample is then rinsed with toluene and immersed in a second solution of 1 mM 1,8-octanedithiol (the molecule of interest) in toluene. During this second stage, some of the dithiols attach to the gold substrate by exchanging Au-S bonds with the monothiols, as shown in Fig. 4.3(b). Then 2-nm gold nanoparticles (GNPs) can be attached to the dithiols by a second Au-S bond at the opposite end of the molecules, as shown in Fig. 4.3(c). This is accomplished by exposing the monolayer sample face-down to a solution of 0.25 g/L of nanoparticles in methylene chloride for three hours. The gold nanoparticles are stabilized with triphenylphosphine molecules, which exchange with the dithiols, which have a greater affinity for gold. We observed that the gold nanoparticles do not bond to the monolayer if dithiols are not present. The samples are then rinsed in methylene chloride and dried with nitrogen prior to electrical measurements (Fig .4.3(d)).

4.2.3 GNP-labeled dsDNA sample

Two kinds of purified complementary DNA strands with 26 base pairs were purchased [90]. In our experiments on DNA conductivity, ssDNA molecules (5′–CAT TAA TGC TAT GCA GAA AAT CTT–AG-3′–$(CH_2)_3$–SH) were adsorbed for two hours on a flat gold substrate via a propyl-thiol end linker to form a self-assembled monolayer, as shown in Fig. 4.4(a). Before this step, the 3′-ssDNA is maintained in its oxidized form- $(CH_2)_3$-S-S-$(CH_2)_3$-OH in order to protect the thiol group from undesired oxidation. The protection group is removed by reduction with tris (2-carboxyethyl) phosphine (TCEP). The reduced ssDNA oligomer is then separated and immediately pipetted onto a clean Au(111) surface. At the same time, the following complementary strands (5′-CTA AGA TTT TCT GCA TAG CAT TAA–TG-3′–$(CH_2)_3$–SH) are reduced from protection using the same method. The solution with reduced complementary oligonucleotide is stirred with the GNP (10 nm) suspension to connect with the particles via Au-S bonding, as shown in Fig. 4.4(b). The resulting complementary ssDNA–GNP derivative is diluted with Tris-NaCl buffer solution that contains

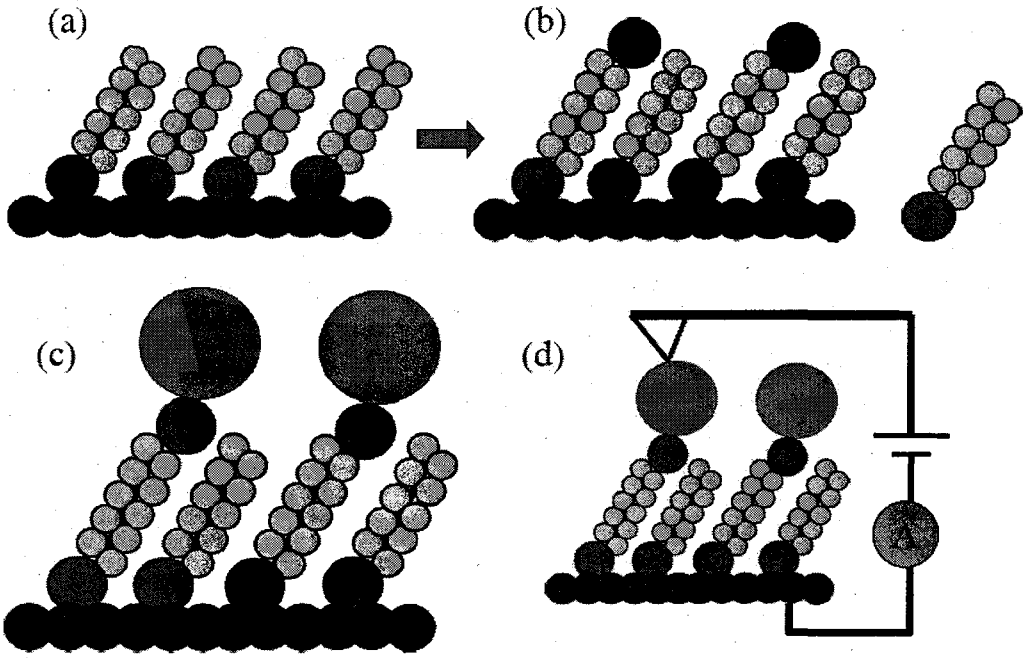

Figure 4.3: Procedures for preparing the GNP-labeled alkanedithiol sample. (a) Formation of a self-assembled monolayer on a gold surface by alkanethiol molecules. (b) Formation of a mixed layer of alkanethiol and alkanedithiol molecules. (c) Gold nanoparticles bound to the other end of the alkanedithiol molecules to form GNP-alkanedithiol-Au structure. (d) Schematic diagram for the electrical measurements on alkanedithiol molecules labeled by GNPs.

MCH (6-mercapto-1-hexanol) molecules, and pipetted onto the ssDNA monolayer. During the incubation at 100% relative humidity, the complementary strands were hybridized with the ssDNA adsorbed on the gold film to form double-stranded DNA (dsDNA) molecules that connect the GNPs and the Au (111) surface with two opposite thiol ending groups. The result is an embedded Au-dsDNA-GNP structures in a nonconducting ssDNA monolayer, as shown in Fig. 4.4(c). The ssDNA molecules help the dsDNA molecules extend away from the surface, avoiding direct interaction between dsDNA molecules and the metallic surface which can distort the DNA conformation and perturb the conductive channel [79, 92]. The MCH molecules in the solution can be adsorbed on the gold surface as a spacer for the ssDNA molecules. They are used to remove non-specifically adsorbed ssDNA from

the gold surface and help the hybridization between the complementary DNA strands [94]. Next, the samples are rinsed with fresh buffer solution to remove ssDNA-GNP derivatives bound to the sample surface non-specifically. Finally, excess salts are removed by rinsing the samples with deionized water.

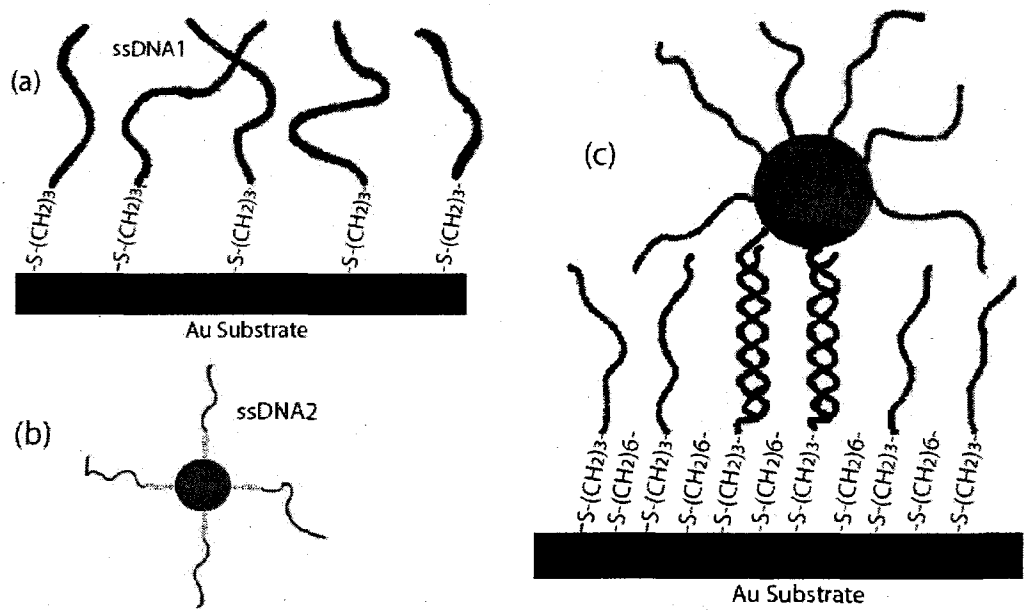

Figure 4.4: Schematic diagrams showing the preparation of dsDNA samples labeled with GNPs. (a) Single-stranded DNA molecules form a self-assembled monolayer on a gold surface. (b) Complementary ssDNA molecules bind with gold nanoparticles via their linkers to form a complex. (c) Complementary ssDNA molecules hybridize with the ssDNA strands on the gold surface to form a GNP-dsDNA-Au complex. The surface is also modified with MCH molecules to improve the DNA hybridization. The linker between the dsDNA and GNP is not shown for simplicity.

An important question is to what extent our measurements reflect the resistance of the DNA molecule itself, as compared to the contacts made to it. As shown in Fig. 4.4(c), the current measured on a GNP flows through a circuit that consists of two Au-S contact resistors, two 3-carbon-chain linker resistors, and a DNA resistor – all in series. Thus, we need to know the estimated resistance of the DNA molecule relative to the linker groups and to the contact resistance. From the Landauer formula, Eq. 2.1, we know that the resistance

of a single Au-S contact is larger than the gold-gold contact resistance (13 kΩ for 1 channel, smaller for more channels), because of a smaller transmission probability. At present, the precise resistance of the Au-S contact is not known, and we are assuming that it is small relative to the linker resistance. To estimate the resistance of the linker groups, we use the results of Cui *et al.*, who showed that a single octanedithiol molecule has a resistance of 900 MΩ [21, 22] and is an exponential function of the number of carbon atoms. We can then estimate the resistance of a 3-carbon-chain to be about 50 MΩ. Thus, as long as the DNA molecule under study has a resistance that is greater than 50 × 2 = 100 MΩ, it will create the largest voltage drop in the equivalent circuit. In our work, typical differential resistances are on the order of 100 MΩ near breakdown but are substantially higher when lower voltages are applied.

4.3 Instrumentation and apparatus

4.3.1 Thermal evaporator

The deposition of gold films on mica substrates was carried out in a thermal evaporator. The vacuum system of the thermal evaporator has a glass vacuum chamber, a rotary mechanical pump, and a secondary diffusion pump with liquid-nitrogen trap. The chamber reaches a base pressure at 1.0 $\times 10^{-6}$ Torr after 12 hours of pumping. Before evaporations, fresh mica slides (15 mm × 22 mm) were cleaved using adhesive tape or a knife to yield clean substrates. The mica slides were fixed on a sample holder as shown in Fig. 4.5 and immediately transfered to the vacuum chamber, which was then pumped down.

During vacuum pumping, the mica was heated to 370 °C by the heater inside the sample holder, where the temperature was measured by a digital multimeter [93] connected to a thermocouple [93] in the sample holder. Gold (99.99% purity level) [93] was used in all evaporations. It was filled in an alumina-coated molybdenum boat (inverted top-hat trough heater) shown in Fig. 4.5. After the chamber was pumped down to 1.0 $\times 10^{-6}$ Torr, gold was melted in the boat heated by an AC power supply to allow a stable gold evaporation rate of 0.6 nm/s until the film thickness reached 100 nm. The evaporation rate and thickness were monitored by a quartz-crystal resonator [93]. The principle for the thickness monitor is that piezoelectric quartz-crystals can produce an oscillating electrical charge, with the

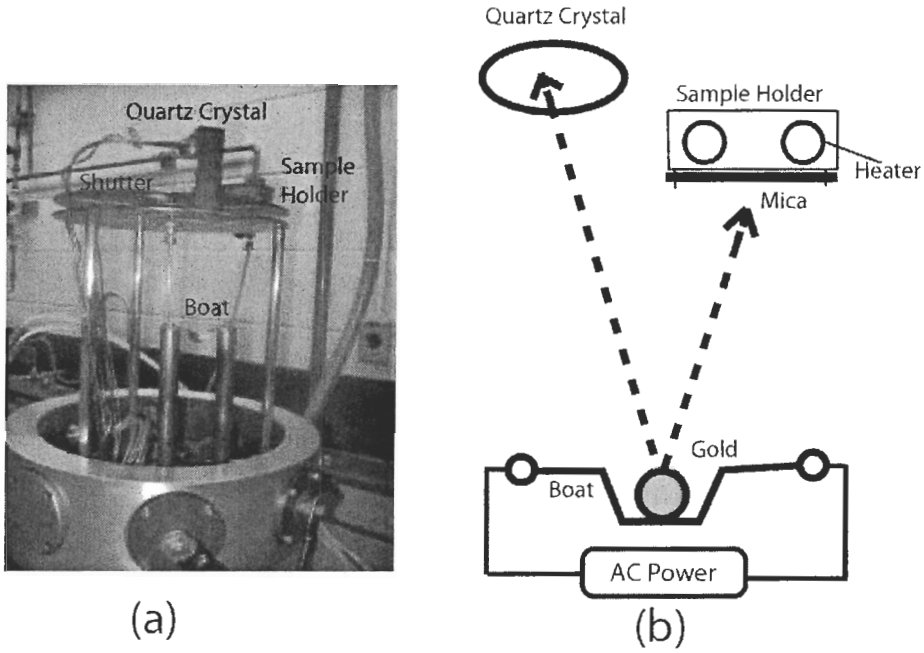

Figure 4.5: (a) Evaporator used for the thermal deposition of gold films on mica. (b) Side view (schematic).

oscillation frequency depending on the mass of the crystal. During the gold deposition, the frequency counter measures the decrease in oscillation frequency of the quartz crystal. Knowing the density and acoustic impedance of the deposited material, one can estimate the mass that has been deposited. After the desired thickness was reached, the power supply for boat and heater for mica were both turned off, to let the deposited gold film cool down to room temperature in vacuum. During evaporation, proper alignment of the gold in the boat was very important for measuring the evaporation rate and thickness accurately. After deposition, the films were removed from the evaporator, and kept in a vacuum container for further use.

4.3.2 Scanning tunneling microscopy (STM)

Scanning tunneling microscopy (STM) was invented by Gerd Binnig and Heinrich Rochrer in 1981 at IBM Zurich, Switzerland [95]. The STM allows one to image materials down to

the individual atomic level. Starting from the STM, many other scanning probe microscopes (SPM) such as the atomic force microscope (AFM), magnetic force microscope, and near-field scanning optical microscope have been developed [96].

STM uses a sharpened, conductive tip to approach a sample surface with a bias voltage applied between the tip and sample surface. When the tip is brought close enough to the surface (typically within several angstroms), a tunneling current flows across the gap between the sample and tip (Fig. 4.6(a)). Since the tunneling current depends on the gap distance, bias voltage, and electronic structure of the surface, the current signal can be used to construct images of the sample surface. The use of tunneling current for STM also implies a limitation: the tip and sample surface should be both conducting. In spite of this limitation, STM is widely used in surface and material studies for its high resolution and precision. The most important aspect of STM is that the tunneling current I_t decays exponentially with the tip-sample distance Z,

$$I_t \propto V\rho_s(E_F)\exp[-1.025\sqrt{\phi}Z], \tag{4.1}$$

where V is the bias applied to the tip, $\rho_s(E_F)$ is the density of states at the Fermi level of the sample, and ϕ is the tunneling barrier [95].

4.3.3 Atomic force microscopy (AFM)

Atomic force microscopy (AFM) is similar to STM, replacing the tunneling current tip with a force sensor. The force between a sample surface and a sharp tip, which is mounted on the end of a cantilever, is used to construct the surface topography. When the AFM tip scans over the sample surface, the force between them bends the cantilever. The deflection of the cantilever is measured to calculate the local surface profile. Since AFM is based on force measurements, it can be used to study surfaces of any conductivity, which is the most important advantage of AFM relative to STM. Two AFM machines were used in our measurements. Octanedithiol molecules were measured on a home-made contact-mode-only AFM. Later, a second AFM (MFP-3D Stand Alone Model, Asylum Research) became available and was used for conductivity measurements of single DNA molecules. Since we found that the contact-mode-only AFM was not suitable for scanning the dsDNA samples, all of the measurements of DNA molecules were done on the MFP-3D AFM.

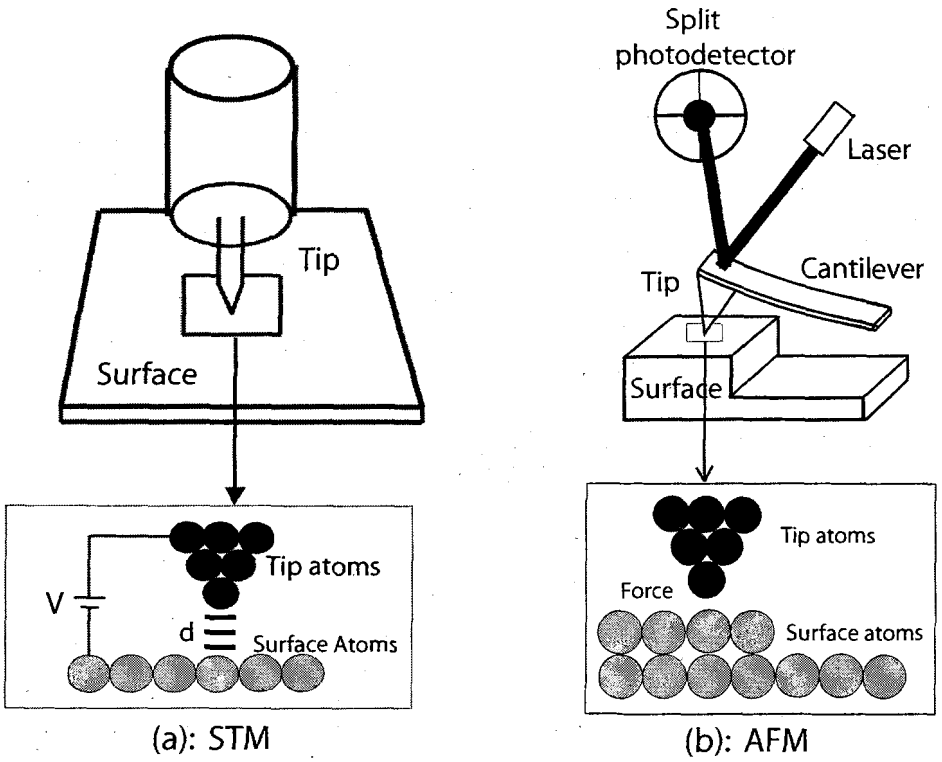

Figure 4.6: Schematic diagrams and basic principles of (a) STM and (b) AFM.

Most AFM instruments use a beam-deflection method to detect the small bending of cantilever due to the tip-sample forces (Fig. 4.6(b)). A laser beam is reflected by the top side of cantilever and falls on a split photodiode position-sensitive detector (PSD). Voltages on the four different quadrants of the PSD are proportional to the light intensity of laser that falls on them. Motions of the cantilever in both the normal and torsional directions can be calculated from the voltages on PSD. The mechanical amplification due to the large ratio ($\approx$1000:1) between the cantilever-detector distance and the cantilever size scale makes it possible to detect angstrom-scale movements of the cantilever. In an AFM, the highly accurate movements of the AFM tip relative to the sample surface in X, Y, and Z directions are also well controlled by piezo elements made from piezo-electric ceramic materials that change dimensions in response to applied external voltages.

There are several forces typically contributing to the deflection of an AFM cantilever

[96]. The different forces originate from different parts of the AFM tip or cantilever. For example, intermolecular forces act between the mesoscopic tip and the sample surface; electrostatic forces act between a charged surface and localized charges on insulating tips. Moreover, a liquid meniscus between tip and surface can be formed by water vapor in air. As a result, surface tension can exert a strong attractive force that holds the AFM tip in contact with the sample surface (capillary forces).

The intermolecular forces are usually described by a Lennard-Jones potential [97],

$$V(r) = 4\epsilon[(\frac{\sigma}{r})^{12} - (\frac{\sigma}{r})^{6}], \tag{4.2}$$

where ϵ is the well depth and σ is the hard sphere radius, which can both be determined by experimental data. In this potential, the attractive (negative) term is from the van der Waals interaction, and the other term is due to the short-range repulsion forces.

From the Lennard-Jones potential relation, the dependence of intermolecular forces on the distance between the tip and sample follows the sketch shown in Fig. 4.7, which has two important regimes: the contact regime and the non-contact regime. The interaction between tip and surface is a repulsive force if the distance between them is in the contact regime. When the distance is larger, the interaction becomes attractive. Corresponding to the different regimes of intermolecular forces, an AFM can be operated in three modes: contact mode (static mode), intermittent-contact mode (AC mode), and non-contact mode. In our experiment, the home-made AFM works only in contact mode, while the MFP-3D can also work in AC mode, which was better for the dsDNA measurements.

Contact mode (static mode)

In contact mode, the cantilever is held a few angstroms above the sample surface, which is in the contact regime of the intermolecular-force curve. There is therefore a repulsive force between the tip and the sample surface. Since the force slope in the repulsive region is very steep, the repulsive force increases strongly with decreasing tip-sample distance. Thus, the force causes the cantilever to bend rather than move further towards the surface. The repulsive force then balances the total attractive effect from capillary forces and the restoring bending force from cantilever. The cantilever used for contact mode usually has a low spring constant ($\approx$ 0.1 nN/nm) and low resonant frequency (10 kHZ). Thus in contact mode, the AFM tip actually makes a physical contact with the surface (force $\approx$2 nN).

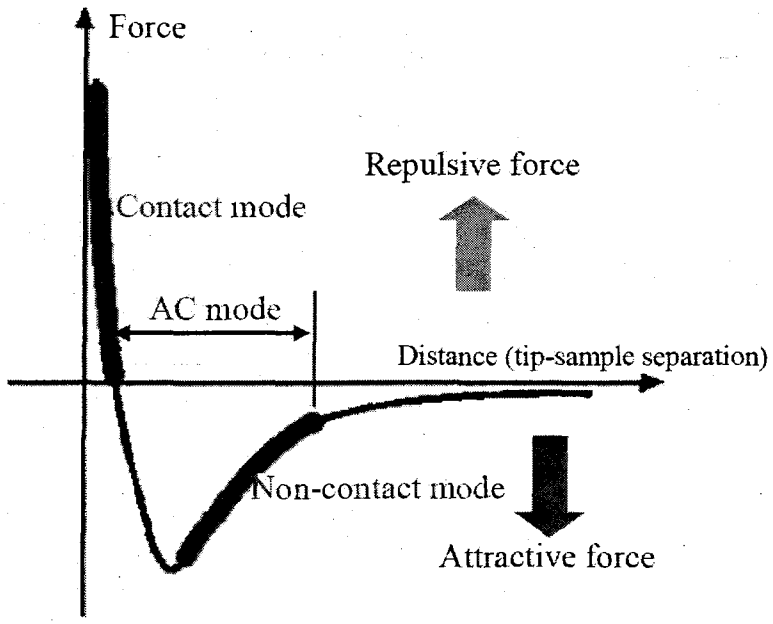

Figure 4.7: Schematic plot of the intermolecular force vs. distance between an AFM probe and the sample surface.

Generally, topographic data is obtained using either constant-height mode or constant-force mode. In constant-height mode, the height of the scanner is fixed when it scans over the sample, and the deflection of cantilever varies due to the changing tip-sample distance. The deflection measured by the PSD is used to generate the topographic image directly. The constant-height mode is often used to take images on atomically flat surfaces where the deflection variation is small. In the constant-force mode, feedback is used to keep the cantilever deflection (force) constant by moving the scanner up and down in the vertical direction during the scanning. The sample topography is inferred by recording the scanner's motion in the Z direction. Although the constant-force scanning rate is limited by the bandwidth of the feedback loop, the effects of force on the sample are better controlled. This method is thus usually preferred.

One problem with contact-mode AFM is that lateral contact forces on a large object, such as 10 nm gold particles, can be large enough to break the chemical bonds that hold the GNP to the surface. Moreover, lateral forces can also damage the soft materials on substrate in contact mode. That is why we found it essential to use the intermittent-contact

(AC) mode, which minimizes lateral forces, to image the GNP-dsDNA-Au samples and the ssDNA monolayer samples.

AC (Intermittent-contact, tapping) mode AFM

In contrast to the contact mode, AC-mode AFM (AC-AFM) uses a vibrating cantilever excited externally at a constant frequency near its resonance frequency for imaging. The cantilever is excited by an actuator, commonly a piezoelectric ceramic, directly attached to it. The piezo converts a voltage input into an oscillatory motion that drives the base of cantilever, causing it to oscillate in turn. At the bottom of vibration, the AC-AFM's tip is brought close to the sample surface so that it barely taps the surface. During scanning, the vertically oscillating tip alternately contacts the surface and lifts off, which corresponds to the range labeled as "AC mode" in the intermolecular-force-distance curve (Fig. 4.7). Since AC-AFM has a vertical oscillation of about 20 nm, it greatly reduces the lateral force or friction, which minimizes the damage to soft samples. AC-mode AFM is thus widely used to study soft materials, including our DNA samples.

The vibration of a cantilever excited near its resonant frequency in AC mode is reasonably approximated by a simple harmonic oscillation model (SHO) [96]. Effects on the amplitude and phase of the oscillating cantilever due to an external force $F_{drive} = k \cdot A_{drive} \cos \omega t$ are described by:

$$A(\omega) = \frac{A_{drive}\omega_0^2}{[(\omega_0^2 - \omega^2)^2 + \frac{\omega_0^2\omega^2}{Q^2}]} \tag{4.3}$$

$$tan\varphi(\omega) = [Q(\omega/\omega_0 - \omega_0/\omega)]^{-1}, \tag{4.4}$$

where A_{drive} is the driving amplitude of actuator, ω is the driving frequency, ω_0 is the resonant frequency of the cantilever, and Q is the quality factor.

Based on Eqs. 4.3 and 4.4, Fig. 4.8 shows the effect of forces on the amplitude and phase of the vibrating cantilever. The change of oscillation amplitude is measured by the photodetector and analyzed with a lock-in amplifier. In AC mode, the vibrational amplitude typically decreases when the tip is brought closer to the surface. The AFM's feedback loop tries to keep the vibrational amplitude constant by adjusting the position of Z piezo. Thus the topographic image is constructed from the Z-piezo signal. In addition, the phase shift

between excitation and vibration of the cantilever can be used to construct a "phase image," which gives information on the stiffness and dissipation of different areas. Since AC-AFM is usually used in an ambient environment, the Q factor for the cantilever oscillation is often low and dominated by the dissipative interaction between the cantilever and the medium outside.

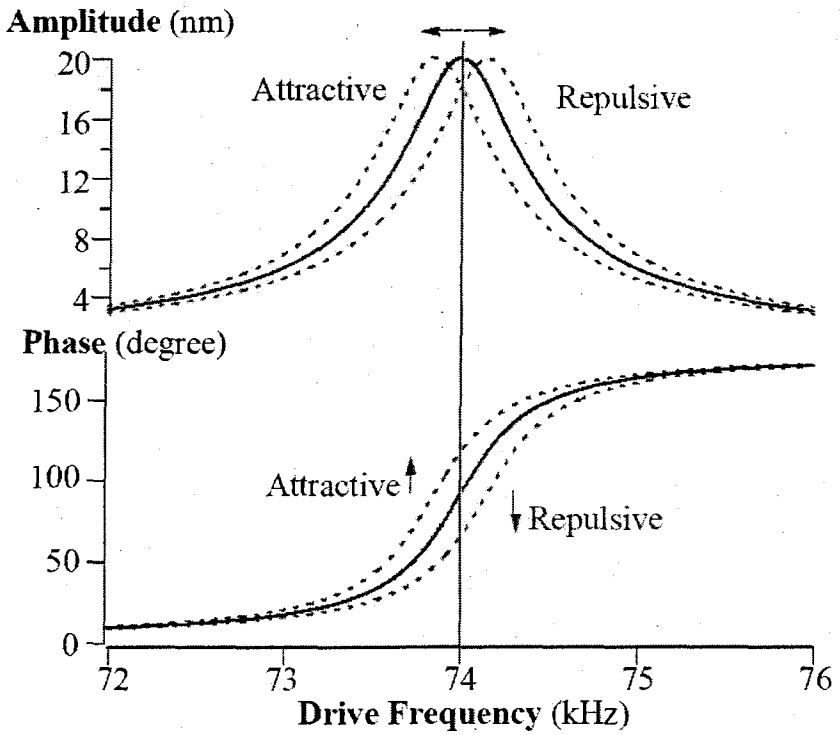

Figure 4.8: Resonance Curves show the effect of attractive and repulsive force gradients on the amplitude and phase of an vibrating cantilever using the Simple Harmonic Oscillator (SHO) model. Parameters such as drive frequency scale are typical of ones we used in our measurements [98].

The non-contact mode is similar to the AC mode and also uses vibrating cantilevers. However, the cantilever in non-contact mode vibrates over a smaller range that is in the attractive force regime on the intermolecular-force-distance curve (Fig. 4.7). In contrast to the AC mode, the cantilever retracts before the tip hits the sample surface. Non-contact mode is usually used in vacuum, where the cantilever has a larger Q factor than that in AC

mode.

Conductive AFM imaging

Conductive AFM is a powerful technique for studying the conductivity of resistive materials. It can map the sample's topography and current distribution simultaneously. For electrical measurements, a current amplifier capable of handling pA to nA currents is necessary. One technique widely used in the electrical measurements by AFM is called "tip-bias scanning," where the conductive AFM is operated in contact mode or tapping mode with a bias on the tip to obtain the sample's topography and electrical signal image simultaneously. In contact mode, the current flowing through the tip is just the DC current. However, the intermittent electrical signal in tapping mode is related to the amplifier response time, frequency of oscillation, and unknown time of contact. It thus gives only qualitative conductivity information. If drift is small enough, conductive AFM can locate the tip stably over points of interest on the sample, and one can do current-voltage (IV) measurements by sweeping the voltage applied to the tip. The current-voltage curves are very helpful for understanding the electrical properties of materials.

The MFP-3D AFM also has a module (Orca-58 cantilever holder, Asylum Research) for conductive AFM imaging. It consists of a specially designed cantilever holder that includes a transimpedance amplifier, with a gain of 0.5 V/nA. The output is digitized by one of the auxiliary 100 kHz ADCs and then digitally low-pass filtered at a bandwidth B=1 kHz. The measured RMS noise for these settings was 0.5 pA, slightly above the Johnson-noise of the resistor used in the transimpedance amplifier, which can be estimated as: $\langle I^2 \rangle^{1/2} = \sqrt{4k_B T B/R} \approx [4 \times 4 \times 10^{-21} \times 10^3/5 \times 10^8]^{1/2} \approx 0.2$ pA. The ORCA module is also used for a variety of electrical measurements. For example, IV curves can be obtained at different force conditions to study how the electrical properties relates to the conformation changes of samples due to the different external forces applied. We do this by sweeping the voltage sinusoidally at a given amplitude and frequency with the different cantilever deflection (force) maintained by a feedback loop. We can also combine conductivity measurements with force measurements, as discussed later.

The conductive probe itself is another important aspect of the c-AFM conductivity measurements. We first used commercial probes (0.2 N/m, 13 kHz) [104] with PtIr5 coating layer for the measurements of octanedithiol using our home-made, contact-mode-only

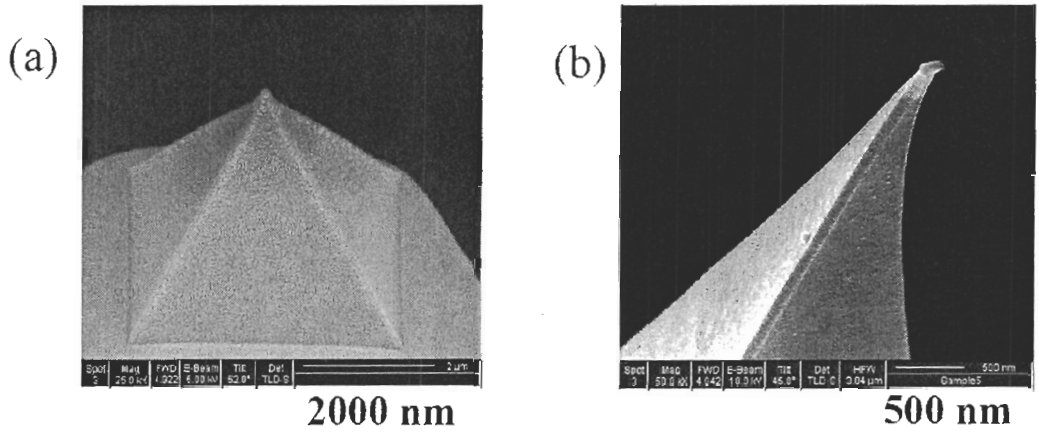

Figure 4.9: Scanning electron microscopy (SEM) images of conductive AFM probes. (a) Si_3N_4 probe sputter-coated with a 30-nm platinum layer. (b) Commercial probe coated with a Pt-Ir layer from Asylum Research.

AFM. We found that the conducting layer of these probes is easily damaged during imaging process. Thus, we tried to make conductive probes by coating non-conductive Si_3N_4 probes with noble metal. Platinum was sputter-coated on the Si_3N_4 probes to a thickness of 30 nm. The probes become conductive, but they do not reflect enough laser light for the AFM signal and are bad for imaging. To solve this problem, we tried to coat the Si_3N_4 probes with a 10 nm titanium adhesive layer and 50 nm gold layer by sputtering. These probes last longer and give a reasonable reflective-laser signal. After we switched to the MFP-3D AFM, we found that commercial probes can last long enough when used only in AC-mode, because of the reduced lateral force. Two kinds of commercial conductive AFM probes were used. The first (Ti-Pt coated) probes have a resonance frequency around 80 kHz and a nominal force constant of 0.8 nN/nm [105]; the second (Pt-Ir coated) probes have a resonance frequency around 75 kHz and a nominal force constant of 2.5 nN/nm [106]. The radius for both types of AFM tips is about 35 nm. While scanning in AC mode, the cantilever is oscillated at a frequency close to its resonance frequency and can be changed to contact mode from AC mode for IV and Force-distance measurements.

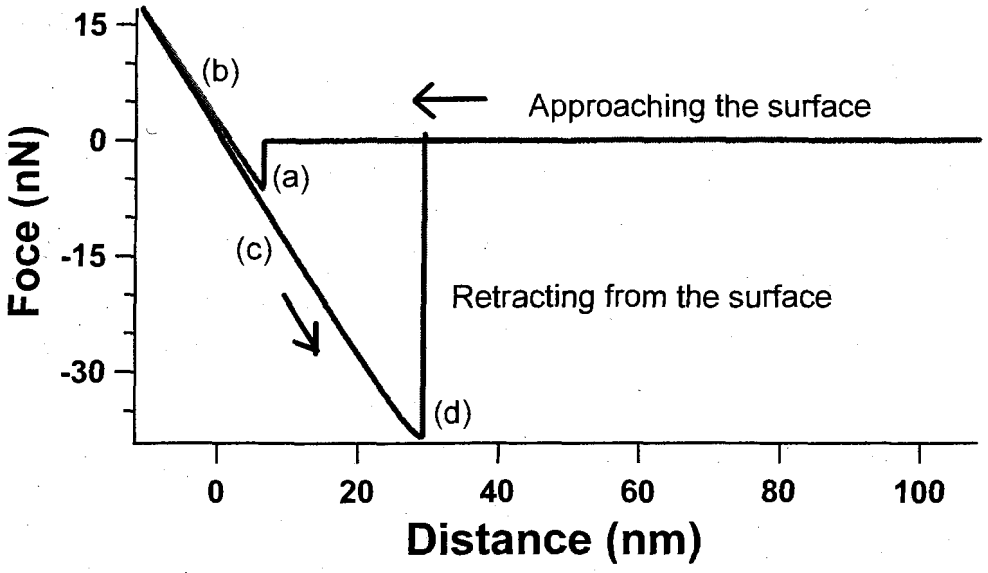

Figure 4.10: Typical force-distance curve measured in open loop.

Force-distance curves

Force curves (force plots) are used to measure the interaction between the AFM tip and the surface as the Z piezo ramps the tip towards and away from the surface. Generally, the force-distance curve is a plot of the deflection of cantilever versus the extension of the piezoelectric scanner.

The PSD signal is converted into a cantilever force by combining the spring constant of the cantilever. The MFP-3D uses the thermal power-spectral-density (PSD) method to determine the spring constant of a cantilever [99]. At the same time, since the piezo element has a nonlinear voltage response, the MFP-3D uses a linear voltage displacement transformer (LVDT) sensor to measure more precisely where the piezo is in the Z direction during the force plot.

A typical force-distance (FD) curve is shown in Fig. 4.10. On the right side, as the piezo approaches the sample surface, the tip does not yet interact with the surface, and the cantilever is undeflected. When the tip extends farther and gets close enough to the surface, at point (a), it will suddenly jump into contact with the surface because of the attractive van der Waals force. The point (a) is called the "snap-in" point in a FD curve. As the

scanner continues to extend, the cantilever deflects away from the surface approximately linearly like a spring, as shown in region (b) of Fig. 4.10. After reaching the extreme left-hand point of the curve, the piezo starts to retract from the surface, following the region (c) in Fig. 4.10. The difference between (b) and (c) is caused by hysteresis in the piezo actuator. When the piezo passes point (a) during retraction, the tip is usually still in contact with the surface and does not come off the surface until it retracts to point (d) in Fig. 4.10. The overshoot is caused by a strong adhesion force between the tip and sample surface (or water monolayer on surface), which holds the tip in contact with the surface. The point (d) is known as the "snap-back" point. As the scanner retracts beyond the snap-back point, the cantilever remains undeflected and moves away from the surface in free space.

Force-distance curves are widely used to analyze the viscosity, lubrication thickness, and local variation in elastic properties of surfaces [100]. Special programming for the control software enables ORCA module of MFP-3D to have other functions combined with the FD curve. One technique used in our measurements on dsDNA molecules is called current-voltage curve/force-distance (IV/FD), which collects the current-voltage (IV) curves at different positions during a force-distance curve. When the Z piezo ramps towards or away from the surface, the total travel distance of the Z piezo is divided into many small steps. A series of IV curves with programmed amplitude and frequency was measured at each position. The IVs at different positions during the approaching or retracting of tip are very helpful for understanding the relation between electrical properties and conformation changes of the dsDNA-GNP complex in a dynamic process.

Other aspects of AFM

Although AFM is widely used in research at the nanometer scale, AFM images are subject to many kinds of artifacts. These artifacts are important to know about and, fortunately, are easy to identify. One of the most common artifacts is known as tip convolution or tip imaging. It is related to the sharpness and the aspect ratio of AFM probes [101]. When an AFM constructs an image of a sample surface, each data points represents a spatial convolution of the shape of AFM tip with the feature of sample surface. If the edge of a feature is sharper than the AFM tip, or if the feature has a higher aspect ratio than the tip, the feature will seem to be larger (Fig. 4.11(a)). Features such as deep trenches will also be altered (Fig. 4.11(b)). Indeed, the AFM tip is imaged by the feature on sample instead of

imaging the feature. The broadening effect is more obvious for conductive tips, which are usually blunt, because of the metal coating on normal non-conductive tips. In spite of the broadening effect, measurements of vertical features are still accurate. This is also true for scanning tunneling microscopy (STM).

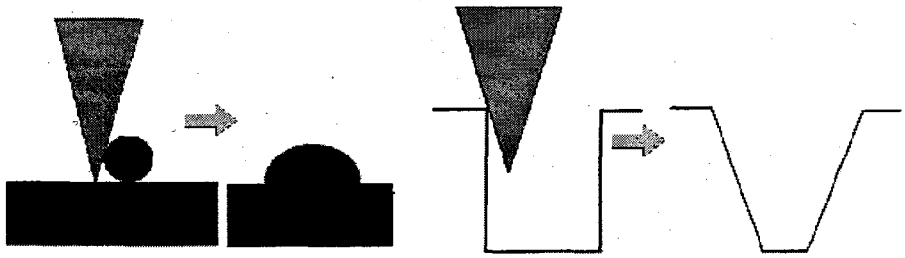

Figure 4.11: Diagram illustrating the tip-convolution effect of AFM. (a) Broadening of features; (b) tip-aspect-ratio effect.

If two atoms on a tip have the same distance away from the surface, all of the features will appear doubled, which is called "multiple-tip imaging." This usually happens when the tip picks up molecules from the sample surface, especially for soft materials. The best way to alleviate this effect is to apply a voltage pulse to change the tip configuration by field emission [101]. If this method fails, we can also use ultraviolet (UV) light radiation (185 nm) to clean the contaminated tip [102]. UV radiation not only destroys chemical bodies directly, it also converts oxygen to ozone, which reacts with organic contaminants [103].

Since it is important to keep the AFM probe stable over GNPs for single-molecule conductivity measurements, we need to eliminate the drift effects of AFM, which can change the relative position between the AFM probe and GNPs. The drift especially in the X-Y plane is as large as 20–25 nm/minute when the AFM system is first set up for measurements. After several hours, the AFM system stabilizes and is subject to only slow drifts. For the home-made, contact-mode-only AFM, the drift is 1–2 nm/minute after it is operated for four hours or longer. The MFP-3D has a better control over the drift, it can be as small as 0.5–0.7 nm/minute after three hours' operation, For a GNP with 10 nm diameter, the drift is small enough that we can make sure the measurements actually are done on the target GNP.

Chapter 5

Experimental Results

In this chapter, I discuss the results of our conductivity measurements on single molecules. First, I discussed the issues about the gold films that are our substrates for octanethiol and ssDNA molecules. I will consider factors that are important for making atomically flat gold surfaces reproducibly, including the issue of contamination particles. Second, I show the results of self-assembled nanojunction experiments on octanedithiol, which confirm the work of Cui *et al.* Then, I show the results of DNA measurements, which give the thickness of the ssDNA monolayer, the topography of the GNPs-dsDNA-Au sample, constant-tip-bias scanning images, and current-bias (IV) curves measured on the GNPs. We find that IV curves show a systematic asymmetry. After ruling out DNA sequence as a possible explanation, we propose an alternative "switching mechanism" to explain our results.

5.1 Au (111) substrate

To produce Au (111) surfaces, we used a thermal evaporator to deposit gold films on mica substrates. After the mica had been heated at 370 °C for 12 hours, the evaporation was done at this temperature with an evaporation rate $\approx$ 0.6 nm/s for a 100 nm thickness, at a vacuum pressure about 1.2×10^{-6} Torr. After flame-annealing or furnace-annealing, we can obtain an atomically flat gold surface. Figure 5.1 is an STM image of a Au (111) surface prepared using this protocol by flame-annealing. The gold film consists of islands with flat tops. The grains are crystalline and (111) terminated on top of the film. The straight step edges with 60° angles in Fig. 5.1 are characteristic of the symmetry of the (111) plane of an FCC

lattice. The edges of the flat regions clearly show a step height of only one gold atom (0.24 nm). These large atomically flat terraces (with a size of 300 nm × 300 nm) on Au (111) surface make gold films good substrates for the formation of self-assembled monolayers and for measurements using scanning probe microscopy.

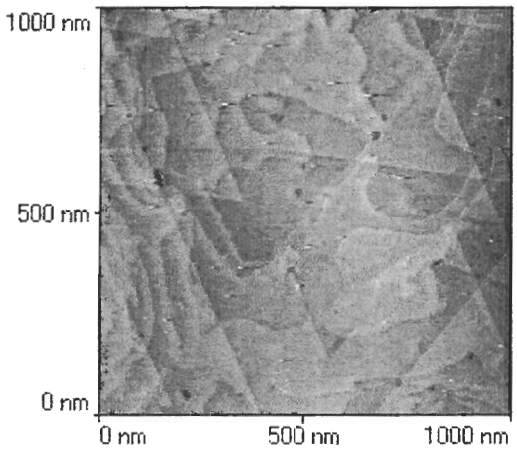

Figure 5.1: STM image of an example of a good-quality Au (111) film.

To show the effect of the temperature of the mica substrate, we deposited two gold films at different temperatures (room temperature and 370 °C). STM images of these two films, without annealing, are shown in Fig. 5.2. The size of gold grains on the films deposited at 370 °C (Fig. 5.2(b)) is 200–300 nm, in contrast to the 10-nm grains of the room-temperature sample (Fig. 5.2(a)). Annealing is the most important step for the formation of Au (111) surfaces. Flame-annealed and furnace-annealed gold films (deposited at 370 °C) are shown in the STM images of Fig. 5.3. The large flat terraces and triangular step interactions in Fig. 5.3(a) and (b) reflect the formation of Au (111) surfaces after both annealing methods. Compared to that in Fig. 5.2(b), these two annealing methods can both cause the gold grain boundaries to diffuse and merge together to form larger grains.

After investigating Au (111) surfaces with AC-mode AFM, we found an aspect of the gold films that was not present in the STM images. Although the gold films seem flat and clean in the STM images, the real gold surfaces are not clean at all. Compare the STM and AC-mode AFM images taken on the same gold film in Fig. 5.4. The sample seems to have a clean surface in the STM image of Fig. 5.4(b), but the AC-mode AFM image in Fig. 5.4(a)

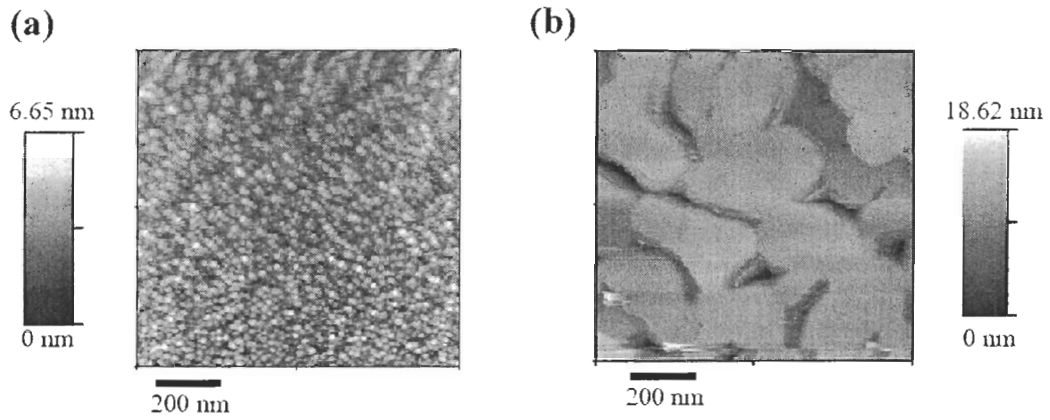

Figure 5.2: STM images of the gold films deposited at different temperatures. (a) Room temperature; (b) 370 $^{\circ}C$. Other evaporation parameters are the same: 0.6 nm/s, 1.2 $\times 10^{-6}$ Torr, 100 nm thickness; no annealing was done.

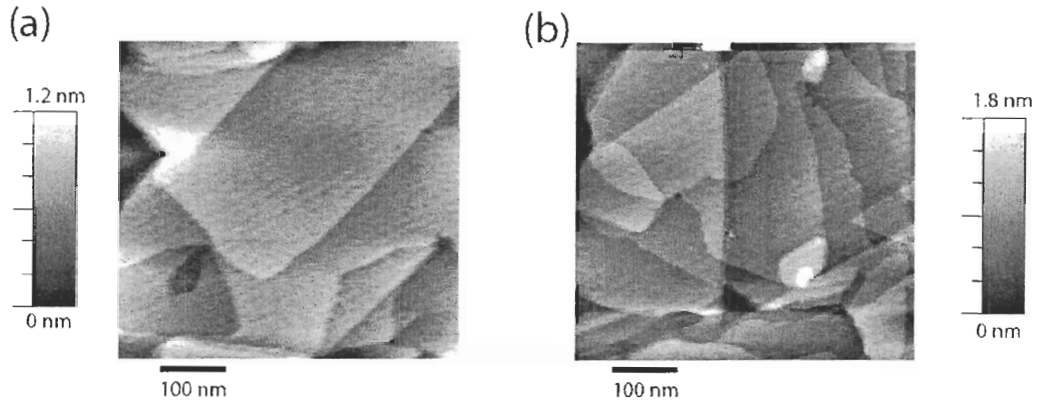

Figure 5.3: STM images of two Au (111) films after annealing. (a) Surface after furnace annealing in a tube at $\approx$ 660 °C for 4 minutes. (b) Surface after flame annealing with a Bunsen burner. Both samples are from the same batch, deposited at 370°C, 0.5–0.6 nm/s, 100 nm thickness.

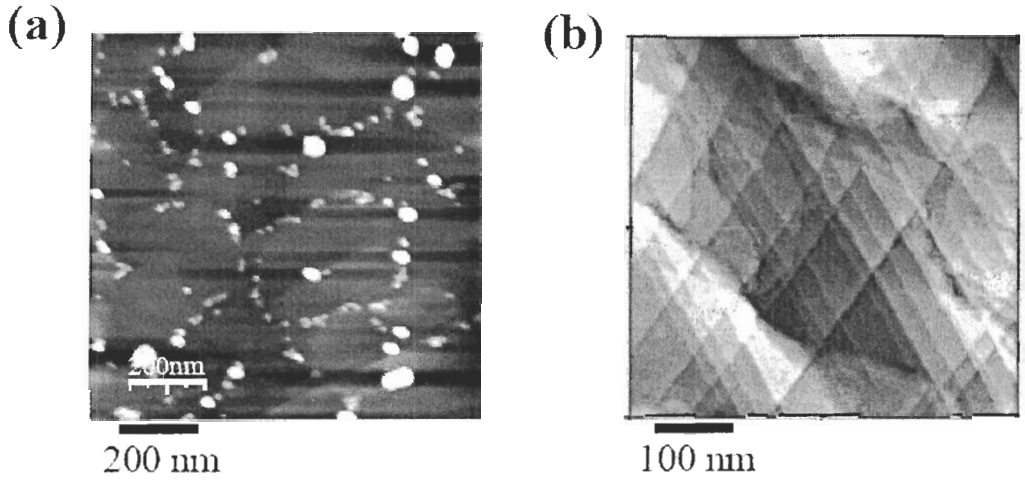

Figure 5.4: Flame-annealed Au (111) surface imaged by two different methods. (a) AC-mode AFM; (b) STM. The particles on the AC-mode AFM image do not appear on the STM image. The larger particles have a height of 4–6 nm, while smaller ones are 2 nm high.

shows that the Au (111) surface is covered by two kinds of particles, with diameters 2 nm and 5 nm. To explain the different images, we recall that, as discussed in Chapter 4, AC-mode AFM exerts a very small lateral force on the tip and merely changes the sample surface; but the STM tip is so close to the surface that it can sweep away the particles on the surface, exerting a large lateral force, when it scans. Thus, the AC-mode AFM images give a better description of the sample's real surface than do those of the STM. The gold films are covered by contamination particles.

The 4–6-nm-diameter particles can be associated with the consumption of the alumina coating layer on the molybdenum evaporation boat. When the boat was heated to a very high temperature for evaporating gold, alumina atoms were added to the gold vapor and were deposited in the gold films. After the gold films were annealed by the flame or furnace, the atoms formed particles on the reconstructed Au (111) surfaces. We found that contamination from 4–6 nm particles usually became worse after the boat had been used for several evaporations. Thus, it is better to replace the boat once being used for several times. After the old evaporation boat is replaced with a new one, the 4–6nm-diameter-

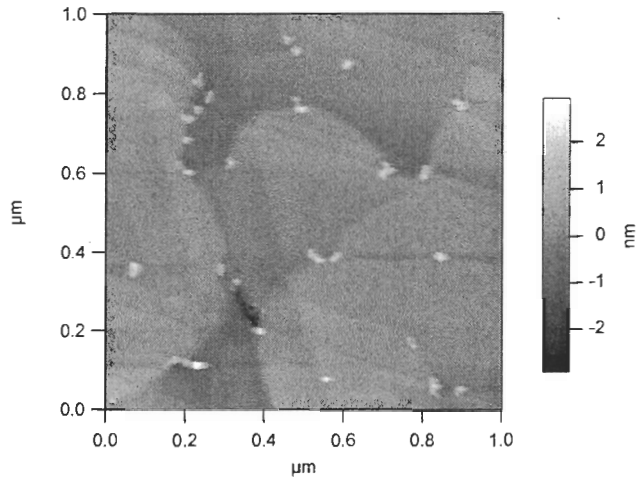

Figure 5.5: AC-mode AFM image of a Au (111) surface with only contamination of 1–2-nm-diameter-particles. The 4–6-nm-diameter-particles disappeared after the old boat was replaced by a new one.

particles disappear. An AC-mode AFM image of a gold film that has only particles with 1–2 nm diameters is shown in Fig. 5.5. The 2-nm particles are probably from air; they appeared on the gold surfaces after the films were annealed to a high temperature, by flame or furnace. Furnace annealing in a better-sealed and nitrogen-protected environment can possibly resolve this problem, which we have not tried yet.

5.2 Measurements of octanedithiol molecules

In our first set of measurements, we studied octanedithiol, in order to confirm the results of Cui *et al.* Once the Au (111) substrates were prepared, they were immersed immediately in a solution of octanethiol molecules. Octanethiol molecules were adsorbed from solution onto the Au (111) surface because of the high affinity of thiols for noble metals. The adsorbates organize spontaneously into crystalline structures [82]. After 24 hours incubation, a self-assembled monolayer (SAM) of octanethiol was formed on the gold surfaces. Figure 5.6 shows the well-known morphology of octanethiol SAM on a Au (111) substrate. There are a large number of pit-like depressions in the SAM, as shown in Fig. 5.6(a). These pit-like defects have diameters of 3.5 $\pm$ 1.5 nm and a depth of 0.24 nm; they are called

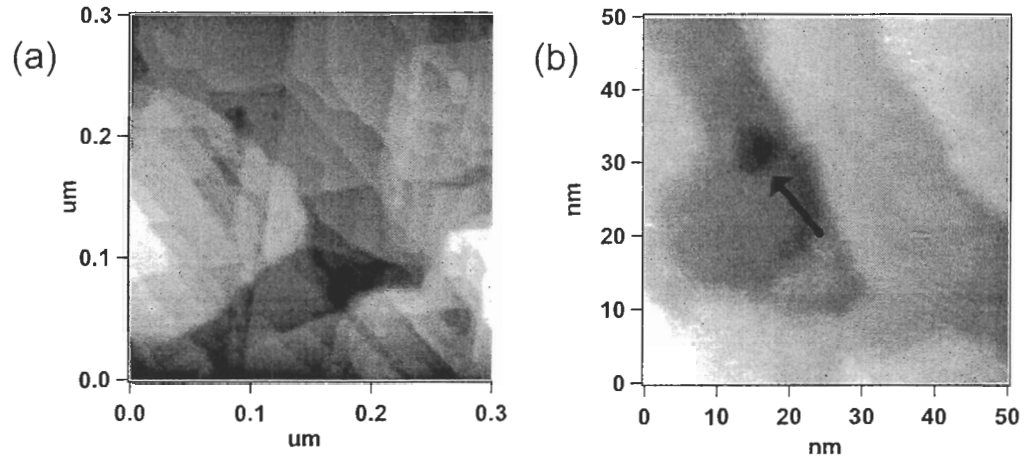

Figure 5.6: Characterisitic morphology of octanethiol SAM formed on Au (111) surface. (a) 300 nm × 300 nm STM topography; (b) 50 nm × 50 nm STM topography. The arrow points to an etch pit in the monolayer.

"etch pits" or gold-vacancy islands [82, 107, 108]. On a smaller scale, Fig. 5.6(b) shows that the octanethiols form a well-ordered, closely packed structure with different domains outside the etch pits. The depth of etch pits is consistent with the Au (111) single-atom step height, suggesting that the pits are defects in the Au surface layer [109]. A widely accepted model for the formation of gold vacancy islands was proposed by Poirier *et al.* in 1997 [110]. In their model, the Au (111) surface is reconstructed during the alkanethiol adsoption, and some gold atoms are released on the surface terraces. The released Au atoms can diffuse rapidly and merge at neighboring step edges. Meanwhile, the vacancies nucleate and coalesce into etch pits one atom deep in the gold terraces [110].

Since we use the octanethiol as a molecular insulator to isolate electrically the octanedithiol molecules from each other, it is important to test whether the octanethiol monolayer is insulating. Current-voltage (IV) curves were measured on the SAM by a conductive AFM probe with a fixed force in contact mode. A typical IV curve on the octanethiol SAM is shown in Fig. 5.7. The current in the IV curve is as small as 100 pA when a bias voltage up to 3 V is applied. The result shows that the octanethiol monolayer is a good insulator.

Exposing the octanethiol SAM to octanedithiol solution results in the replacement of some octanethiol by octanedithiol molecules. Gold nanoparticles (GNPs) with-2 nm di-

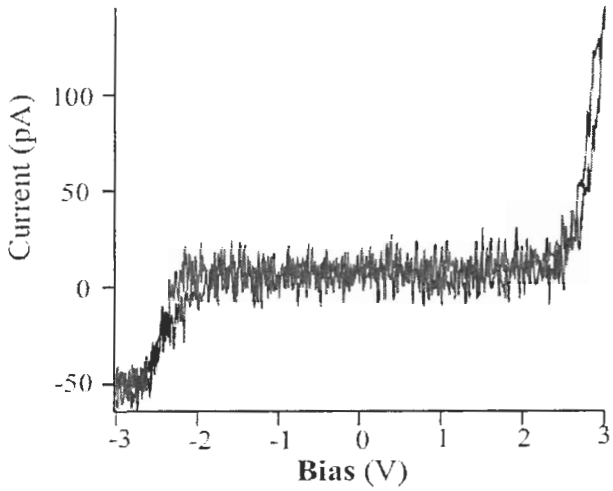

Figure 5.7: A typical current-voltage (IV) curve on octanethiol monolayer measured by conductive- atomic force microscopy (c-AFM), it shows the monolayer is insulating over a large voltage range (−2 V to 2.5 V).

ameters can be attached to the thiol groups at the top of these octanedithiol molecules with Au-S bonds. STM topography images of GNP-octanedithiol-Au system are shown in Figs. 5.8(a) and (b). The heights of the nanoparticles in the profiles are from 1.7 nm to 3 nm, which is consistent with the size of GNPs used for labeling. The width of the particles is enlarged by the convolution effect of the STM tip (Chapter 4.3.3). Since these measurements of octanedithiol samples had been done before we realized that the Au (111) surface can be contaminated by 1–2 nm particles, we had difficulty in distinguishing between the GNPs and the contamination particles. However, as we mentioned, the contamination particles do not appear in STM images (Fig. 5.3), while the GNPs do, because of the strong Au-S bonds. Thus, we believe that the nanoparticles in Figs. 5.8(a) and (b) are the GNPs that were used to label the octanedithiol molecules.

To study the electrical properties of octanedithiol molecules, we first applied the technique of "constant-tip-bias scanning" (Chapter 4.3.3). The GNP-monolayer-Au samples were scanned under a constant-voltage bias on a conductive-AFM probe, yielding topography and current signal images simultaneously. A typical current image is shown in Fig. 5.9. When the tip was over the octanethiol monolayer, at most a very small current passed

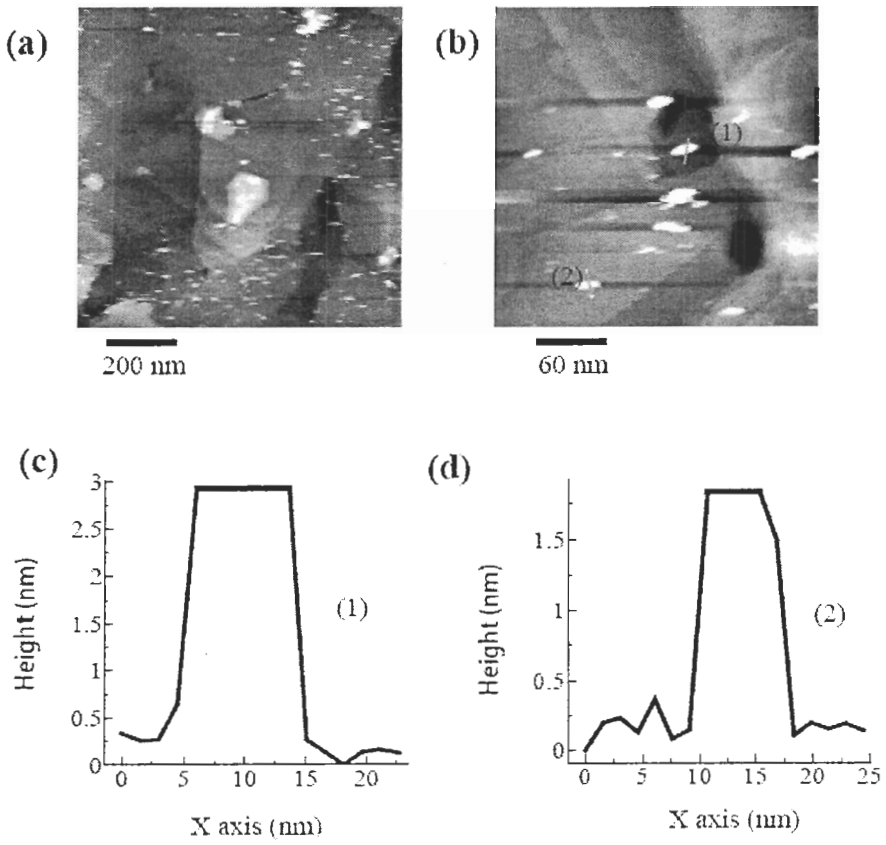

Figure 5.8: STM images and height profiles of the GNP-octanedithiol-Au sample. (a) 1 μm $\times$ 1 μm topography; (b) 300 nm $\times$ 300 nm; (c) Height profile across the nanoparticles (1) shown in (b); (d) Height profile across the nanoparticles (2) shown in (b). The apparent diameter of GNPs is increased because of the finite size of the STM tip.

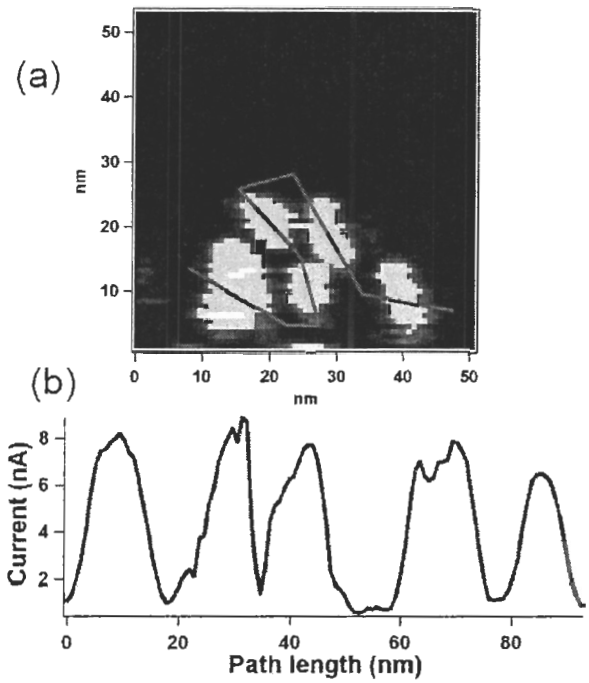

Figure 5.9: (a) c-AFM current image of GNPs-monolayer-Au sample under a constant bias of 1 V. Gray scale indicates the magnitude of current signal, with light areas being more conductive. (b) Line profiles along the indicated path show that the conductivity is nearly constant across a given nanoparticle.

through the AFM tip because of the insulating behavior of the octanethiol monolayer. Thus, the positions over octanethiol monolayer appeared dark, as shown in Fig. 5.9. On the other hand, when the tip was over the GNPs, the AFM probe can make a good metal-metal contact with the GNPs, which increases the conduction dramatically. Thus, the positions over GNPs showed a larger current and appeared brighter in Fig. 5.9. In these measurements, the Si_3N_4 AFM probes were made conductive by sputter-coating a 30-nm platinum layer. As shown in the line profile of Fig. 5.9, the currents through the GNPs are usually about several nA under a 1 V bias. This is much higher than the current detected on the octanethiol monolayer in Fig. 5.7 ($\leq$ 15 pA). Thus, the chemical contact between the octanedithiol and the GNPs can greatly decrease the tunneling barrier between the AFM probe and alkane molecules.

Once the GNPs were identified on the topography or current images, the AFM probe

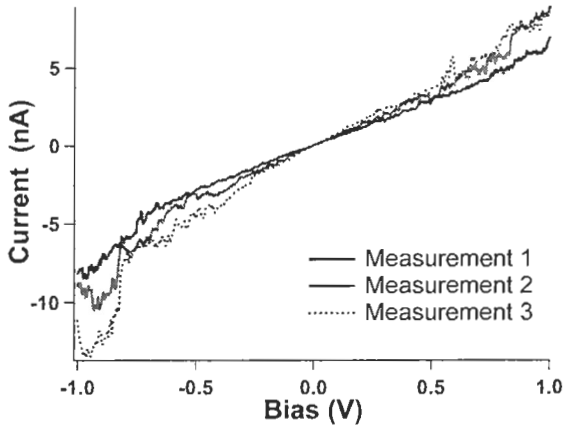

Figure 5.10: Typical current-voltage (IV) curves measured on the same gold nanoparticle successively, using an Si_3N_4-AFM tip sputtering-coated with a 10 nm adhesive layer of titanium and a second layer of 50 nm Au.

was positioned over one of the GNPs. The metal tip was pushed down into contact with the GNPs with a force set by the AFM controller. By sweeping the voltage on the AFM tip, we collected current-voltage (IV) curves, which characterize the conduction behavior of octanedithiol molecules. The interval between surface imaging and IV measurements must be short enough (1–2 minutes) to guarantee that the AFM tip is still on GNPs after the thermal drift in this period (Chapter 4.3.3). Typical IV curves on the GNPs are shown in Fig. 5.10, which shows a series of measurements on the same nanoparticle. The IV curves all had nearly the same resistance. However, a small increase in current was observed when comparing the first to the last IV curve. This can probably be accounted for by a better contact between the AFM tip and GNP during the measurements. However, the drift of the AFM probe relative to the GNP makes it impossible to measure more than five IV curves on the same GNP, which is a limitation of the equipment.

The magnitude of the currents (nA) in the IV curves shown in Fig. 5.10 is comparable to that measured by Cui *et al.* [21]. More IV curves measured on different nanoparticles and on different days were plotted together in Fig. 5.11. We found that the different curves overlap with each other when they are divided by numbers such as 2/2, 2/3, 2/4, and 2/6. These numbers can be explained as corresponding 2, 3, 4, and 6 octanedithiol molecules attached to a single GNP respectively. Since the smallest conductance that we measured

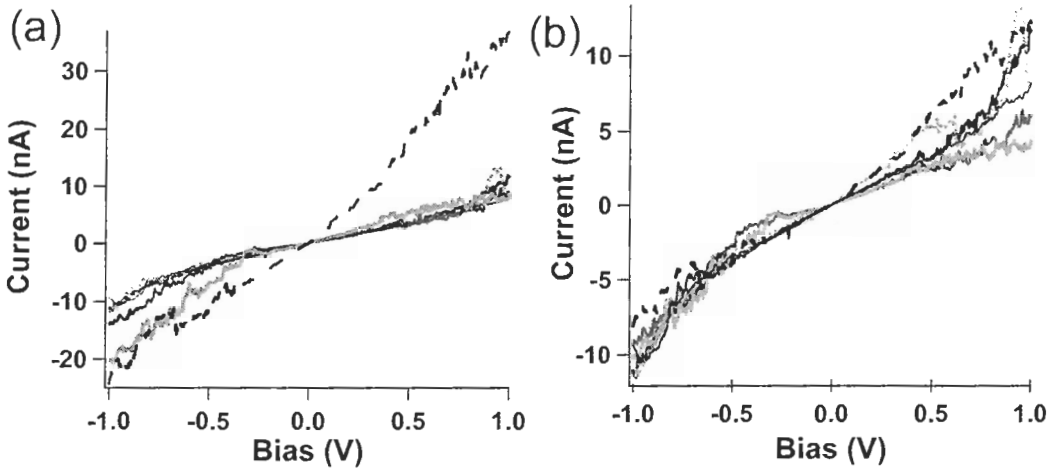

Figure 5.11: Different IV curves measured on different GNPs and different days. (a) Before normalization; (b) After normalization, where the IV curves were divided by 2/2, 2/3, 2/4, and 2/6.

is as twice as that reported by Cui *et al.*, we thought there are at least two octanedithiol molecules connected with a single GNP in our experiments. The factors are chosen to make the IV curves consistent in negative current side. This quantization of IV curves is very similar to the integral multiples for different families of IV curves in the work of Cui *et al.* [21]. Thus, we have not only confirmed the basic results of Cui *et al.*, we have also shown that our own setup performs at a comparable level.

5.3 Measurements of DNA molecules

Having demonstrated that we can make single-molecule conductivity measurements, we turned our attention to our primary goal, measuring the conductivity of DNA molecules. The geometry of our DNA sample is shown in Fig. 4.4(c).

5.3.1 Self-assembled monolayer of ssDNA

We began by adsorbing single-stranded DNA (ssDNA) molecules on atomically flat gold substrates. Self-assembled ssDNA monolayers then formed on the Au (111) surfaces through

Au-S bonds. In order to realize the idealized junction configuration shown in Fig. 4.1, the ssDNA coverage on the gold surface should be dense enough to prevent nonspecific interactions of the DNA backbone with the metal after hybridization [94, 111, 112]; but it should also be loose enough to allow efficient hybridization with complementary DNA strands [113]. The surface of adsorbed ssDNA oligomers on the gold substrate was imaged by AFM in AC mode under ambient conditions. In order to see the structure of the ssDNA monolayer, we imaged a square in contact mode, using a large force (20 nN). The imaging forces were large enough to scratch away the monolayer. Then, in AC mode (which exerts only small lateral forces) we imaged a larger area. In Fig. 5.12(a), we see clearly the part of the monolayer that was removed by the contact-mode imaging. Figure 5.12(b) shows a height profile across the image. From the profile, we infer a monolayer height of 3–4 nm. (Note the bulges at the edge of the contact region, which presumably contain material removed from the central region.) The result for the monolayer thickness is consistent with that of Nogues *et al.* [78]. Large flat grains of gold surface are also visible in the image of ssDNA monolayer. The monolayer is homogeneous and displays close-packed protrusions, which are likely individual ssDNA molecules. The particles on the surface of Fig. 5.12(a) are from the contamination of Au (111) surface before the adsorption of ssDNA.

Chains of ssDNA molecules are soft and have a short persistence length (2 nm) [116]. Thus, the ssDNA molecules are easy to pack closely together to form a monolayer that is not conductive. We found that the ssDNA monolayer is insulating up to 3 V in our IV measurements, as shown in Fig. 5.13. Thus, the ssDNA monolayer can serve as a molecular insulator to isolate dsDNA molocules in the setup of Fig. 4.1.

5.3.2 GNP-dsDNA-Au samples

Next, the ssDNA monolayer was incubated with complementary strands labeled with GNPs to form dsDNA molecules standing between the Au surface and GNPs. The diameter of the GNPs is about 10 nm, which is larger than the ones used to label the octanedithiol molecules. Following Nogues *et al.* [78], we decided to increase the size of the nanoparticles to allow for a better discrimination between contamination particles on gold surfaces (2 nm in diameter) and our GNPs. The GNPs can work as topographic labels to characterize the DNA hybridization on gold substrates at a high lateral resolution [114]. The morphology of

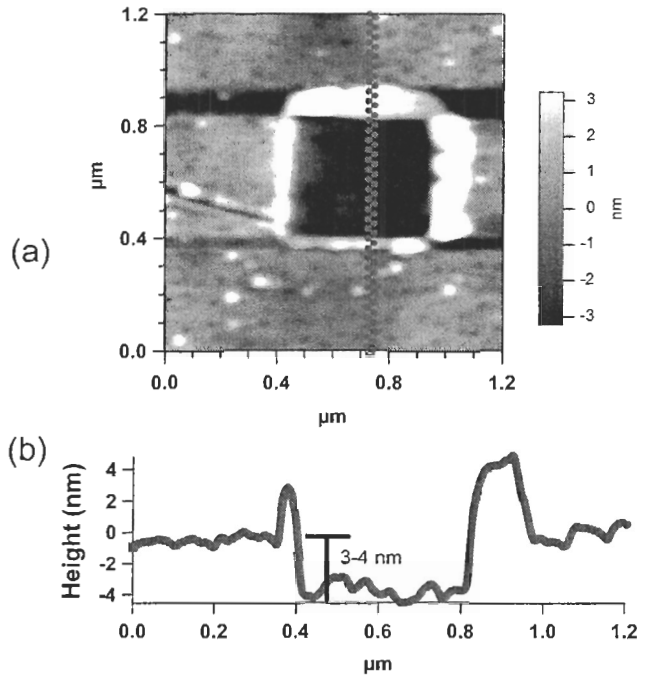

Figure 5.12: (a) AC-mode AFM image of ssDNA monolayer on Au (111) surface, ssDNA in the central square area (400 nm × 400 nm) was removed using contact-mode imaging for the thickness measurements. (b) Line profile displays the thickness of ssDNA monolayer (3–4 nm).

the samples is shown in Fig. 5.14 in AC mode. The gold nanoparticles clearly stand out in the topography image relative to the background of the ssDNA monolayer. The line profile across the GNPs in Fig. 5.14 shows that the height of GNPs is roughly 10 nm above the monolayer (the range is from 8 nm–12 nm). These sizes are consistent with the diameter of the GNPs used for labeling, as determined by transmission electron microscopy. The height of the GNPs also implies that the chains of dsDNA molecules do not protrude above the 4 nm thick ssDNA monolayer. Considering that the 26 base pairs dsDNA is rigid and 9 nm long, the dsDNA must tilt at an angle ($\approx 66°$) with respect to the normal direction of surface. Because the thiol linkers groups are flexible, this configuration is reasonable [80]. This suggests that the configuration for GNP-dsDNA-Au resembles Fig. 5.15(a) rather than Fig. 5.15(b).

Most of our samples (eg. Fig. 5.16(a)) had a density of gold nanoparticles much higher

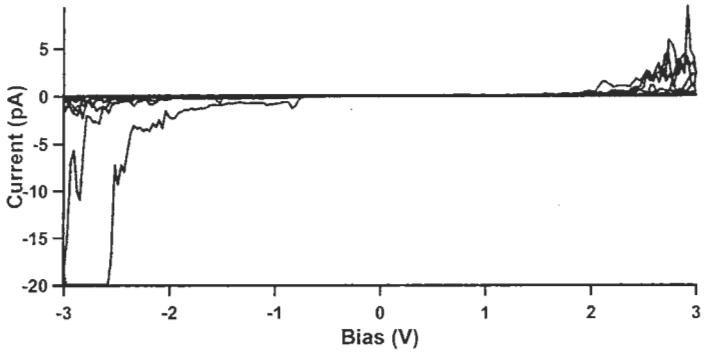

Figure 5.13: Current-voltage curves measured on an ssDNA monolayer (pressing force ≈ 15 nN) show that the monolayer conducts very small current up to a bias voltage of 3 V.

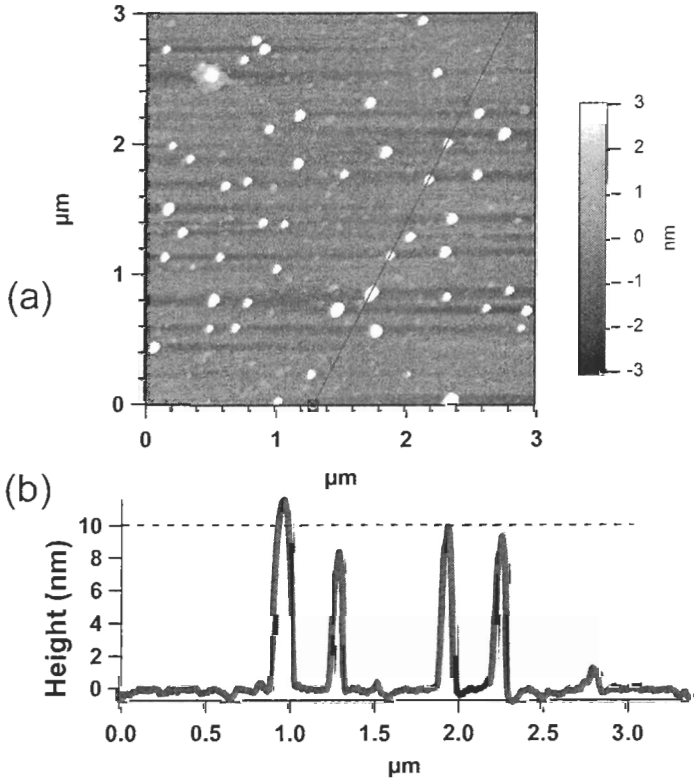

Figure 5.14: (a) AC-mode AFM image of the GNP-dsDNA-Au sample, the gold nanoparticles partially cover the ssDNA monolayer. (b) Line profile over the GNPs show the height of the GNPs relative to the ssDNA monolayer.

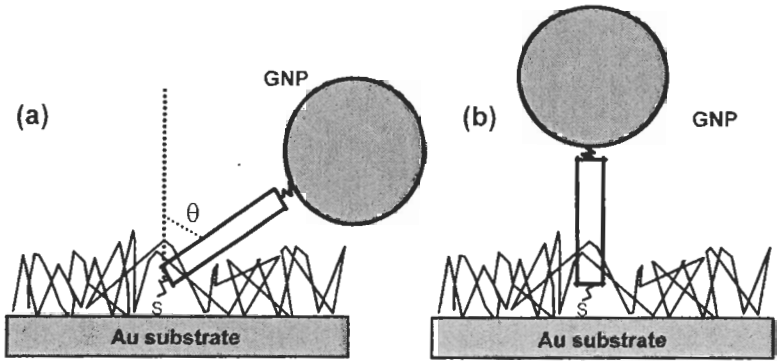

Figure 5.15: (a) The dsDNA tilts at an angle ($\Theta \approx 66°$) relative to the ssDNA monolayer surface normal. (b) An alternate configuration where the dsDNA protrudes above the ssDNA monolayer is not supported by our observations.

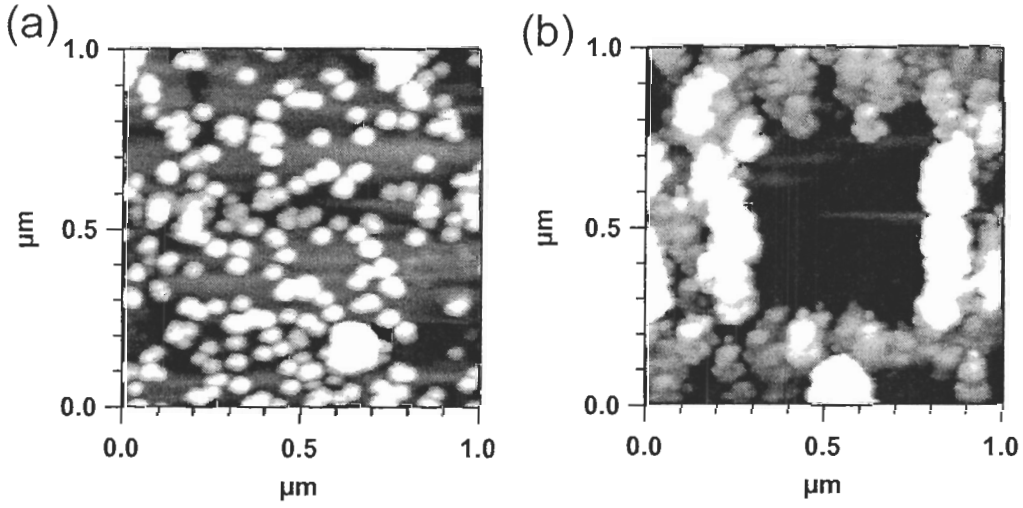

Figure 5.16: (a) AC-mode image of the sample shows the high density of GNPs on the sample. (b) The central 500 nm × 500 nm area of the sample was first scanned in contact mode. Then, a larger area was imaged in AC mode, showing that the GNPs in the center were completely removed by the tip.

than that shown in Fig. 5.14. We also found the density in the central part of sample is lower than that close to the edge (the typical sample size was ≈ 40 mm^2). It is necessary that single isolated GNPs be located on the topographic images for the conductivity measurements. The surface in Fig. 5.16(b) was obtained in a way similar to that in Fig. 5.12. The inner 500 nm $\times$ 500 nm area was imaged in contact mode. Then a larger area (1 μm $\times$ 1 μm) was imaged using AC mode. The GNPs were removed because of the large lateral forces from the AFM tip in contact mode, where the lateral force is usually about several tens of nN. This force is much higher than the $\approx$ 150 pN force required to break the hybridization bonds in DNA molecules [115]. The lateral force is nearly zero in AC mode and does no damage to the surface. Figure 5.16(b) clearly demonstrates that it is better to image the DNA samples using AFM in the AC mode rather than in contact mode.

For the reasons mentioned above, the conventional technique of "tip bias scanning" used for octanedithiol in contact mode is not appropriate for the dsDNA molecules, owing to the larger size of the GNPs. In an alternate technique, developed by Nogues *et al.* [78], AC mode is applied to measure the conductivity behavior. The AFM probe in AC mode taps the surface for just a short time during the oscillation cycle, and the current flowing through the tip can be measured during this short time without apparent damage to the sample. However, in order to perform the current measurements within this limited time, the setpoint of the oscillation amplitude should be greatly reduced to make the tip contact with the surface for a longer time during the oscillation cycle [78]. The current is averaged by the bandwidth of the IV converter, which low-pass filters the current spike. It can be used to qualitatively map a current image during AC-mode scanning.

Using this modified constant-tip-bias imaging technique, we obtained simultaneous topographical and current images of the GNP-dsDNA -Au sample (Fig. 5.18). In Fig. 5.18(b), the currents are low ($\approx$ 10 pA)) because of the averaging effects discussed above. Nevertheless, comparing the topographical and current images, one can easily find the contrast between the insulating ssDNA layer and positions with larger current. The positions showing larger currents in Fig. 5.18(b) correspond to the positions of GNPs in the topography image of Fig. 5.18(a). No current signal was recorded on the ssDNA monolayer in regions without the GNPs. This means there is no detectable leakage current through the ssDNA monolayer. However, there are also some GNPs in Fig. 5.18(a) that have no current flowing through and appear to be as dark as the ssDNA monolayer in Fig. 5.18(b). We hypothesized

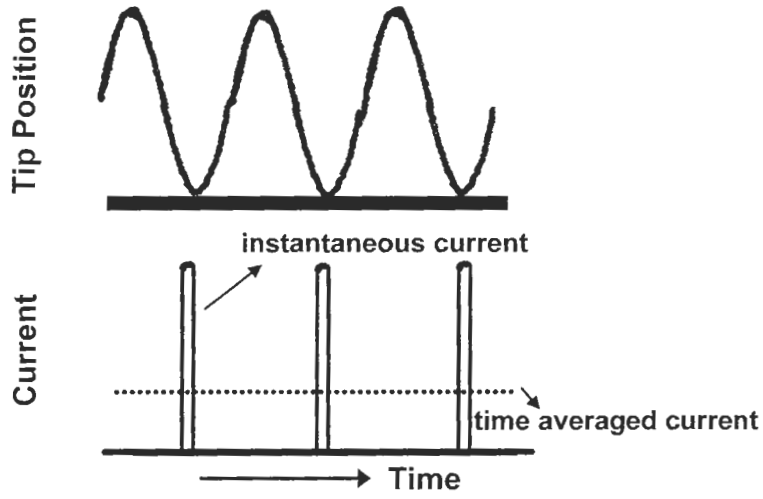

Figure 5.17: Schematic diagram for tip-bias scanning technique in AC mode. The current spikes were low-pass filtered and averaged by the bandwidth of the IV converter.

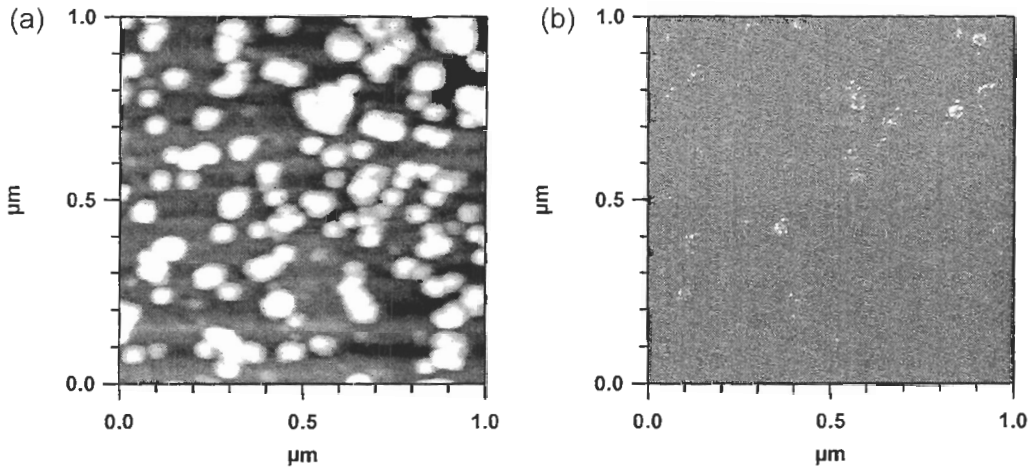

Figure 5.18: AC-mode AFM images of the GNP-dsDNA-Au sample using the technique of tip bias scanning. (a) Topography showing the GNPs on monolayer. (b) Current signal image under a −4 V bias on the sample; the current here is 5–30 pA scale.

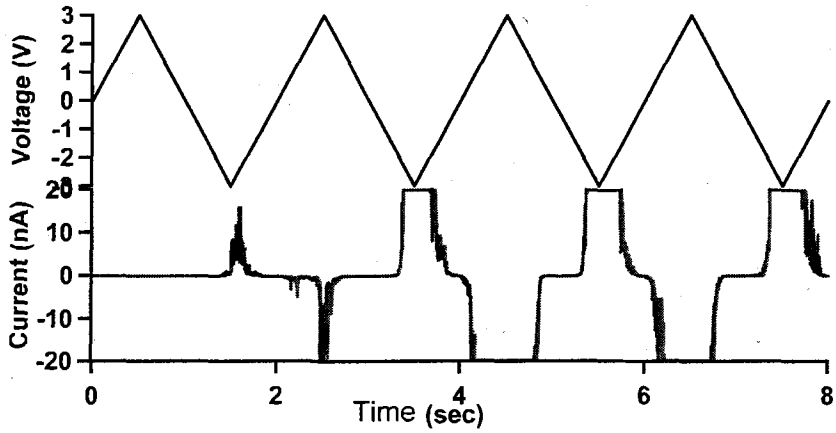

Figure 5.19: Typical current response as the voltage was swept linearly between −3 V and +3 V. The applied force is attractive (−25 nN).

that these are non-specifically bound GNPs that were not hybridized with the other ssDNA molecules on the gold substrate. Thus, there was no dsDNA helix formed to provide a pathway for the current signal. This observation is consistent with the results in [78]. In that work, Nogues *et al.* also did control experiments where ssDNA molecules were incubated with GNPs labeled by non-complementary ssDNA molecules. They did not detect any current above the noise level on all of their GNPs.

Once the GNPs were located on the topographical or current images, the AFM probes can be brought into contact with the GNPs in contact mode using a controlled contact force. IV curves were then measured quantitatively to explore the electrical properties of the dsDNA molecules. The AFM software has a very good control over the force applied on the GNPs while performing electrical measurements (± 50 pN). A typical series of current events is shown in Fig. 5.19 as a function of time. The first one or two cycles in the current series measured on a GNP usually show insulating behavior between −3 V and +3 V. This behavior may be caused by the insulating ssDNA molecules surrounding the gold nanoparticle. In this case, the AFM tip must penetrate the ssDNA layer to make good electrical contact with the GNPs. It could also be due to the residues of contamination on the tip, which can be removed after the voltage sweep is applied. The current plateaus at ± 20 nA are caused by the range limit of the current-voltage amplifier.

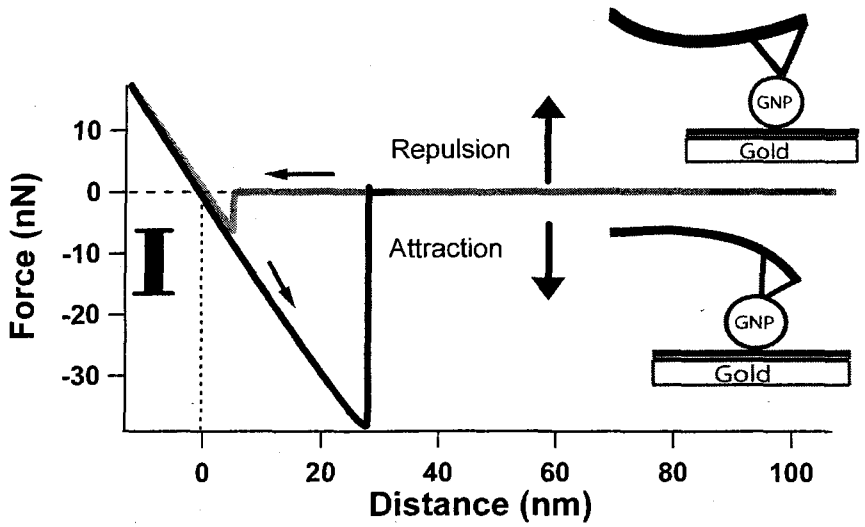

Figure 5.20: Typical force vs tip-sample distance curve. The regimes of repulsive and attractive forces are indicated by arrows. For the IV measurments, an attractive force indicated by the shaded box was maintained.

In contrast with the case of octanedithiol, the shape of IV curves on the GNPs depends sensitively on the force applied on the AFM metal tip in contact mode. In particular, the IV curve depends on whether the force between the AFM tip and GNPs is attractive or repulsive. When it is an attractive force, as in the lower part of FD curve in Fig. 5.20, the IV curve usually shows an S shape characteristic of a semiconductor. When the force is repulsive, as in the upper part of F-D curve in Fig. 5.20, the current changes linearly with the voltage and shows a small resistance. We interpret this "high force" result as implying that the force on the GNPs changes the conformation of dsDNA molecules. Since the dsDNA molecules have a persistence length of 50 nm [116], they can be thought as rigid rods. The force more likely changes the tilt angle between the dsDNA rods and ssDNA surface. We prefer not to push the dsDNA molecules toward substrate for their electrical property measurements. Thus, a net attractive force, as indicated in Fig. 5.20 is maintained for reproducible IV measurements of dsDNA. The force can be monitored via the deflection voltage of the AFM's photodetector.

5.3.3 Asymmetry of the IV curves

In the IV curves measured on GNPs, the voltage gaps on the positive side are always smaller than the ones on the negative side (Fig. 5.21b). In other words, the dsDNA molecules seem to have an asymmetric behavior for charge transport, conducting better along one direction than the other. Considering the DNA molecules used in our experiments, the reason may lie in the asymmetry of the DNA sequence. One way to test this hypothesis would be to measure the current-voltage behavior of DNA molecules with a symmetric sequence. This would require synthesizing new DNA molecules with a symmetric sequence, a relatively expensive and time-consuming procedure. An easier test uses the DNA molecules we already have. The idea is to reverse the end connection of the two complementary strands, as shown in Figs. 5.21(a) and (c). If the asymmetry of the IV curves were caused by the asymmetry of the DNA sequence, the shape of the IV curves would change. However, we observed that the IV curve corresponding to the situation in Fig. 5.21(d) retains its shape (compare with Fig. 5.21b). The voltage gap on positive side is still smaller than that on the negative side. Thus, we conclude that the asymmetry of the IV curves is not due to the asymmetry of DNA sequences and must have some other cause.

Another idea is that the asymmetry may be caused by a conformation switching mechanism. Rant *et al.* and Kelly *et al.* have reported that short dsDNA tethered to a gold surface in an electrolyte solution can switch between a "lying" and a "standing" state by applying alternating electrical bias potentials to the gold surface [116, 117]. The conformation change arises because of the electrostatic interaction between the intrinsic negative charges on the DNA strands and the induced charges on the metal surface. Because the persistence length for dsDNA molecules is about 50 nm, the 26 bp ($\approx$ 9 nm) DNA molecules can be thought of as rigid rods, which are connected to the Au surface by flexible linkers ($(CH_2)_3$–SH) (Fig. 5.22). The charges on the gold surface due to the bias can interact with the negative charges on DNA strands. This will change the orientation of the dsDNA molecules relative to the flexible linker. The switching mechanism may also happen in our system when the voltage on gold substrate was swept to perform the IV measurements on GNPs. It may be a possible explanation for the asymmetry of IV curves. Although the DNA is in a relatively "dry" form in our experiment, DNA remains negatively charged due to the water molecules of humidity in air and water layer on DNA sample. When the gold

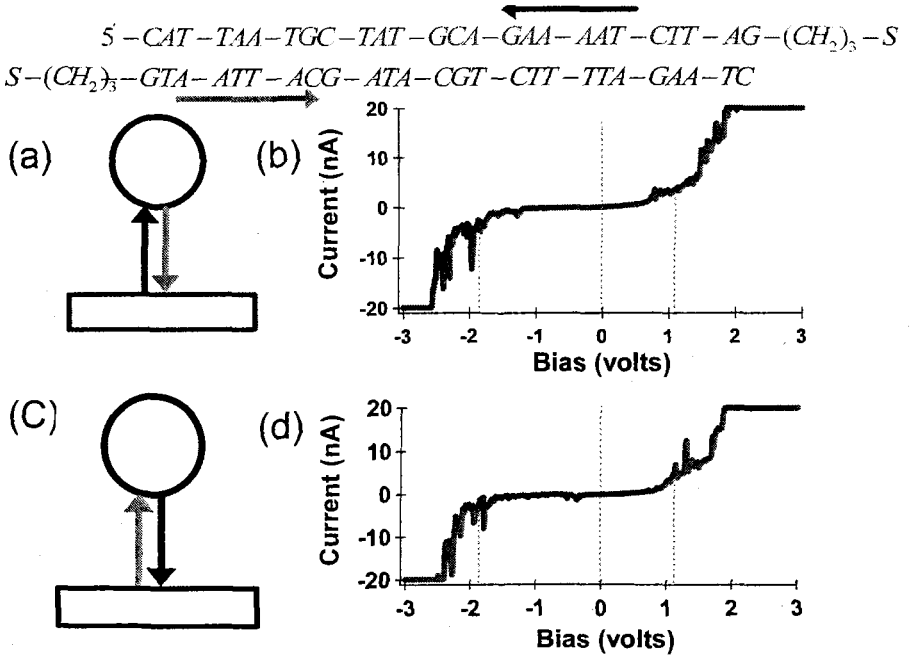

Figure 5.21: Asymmetric IV curves measured on GNPs in different configurations. (a) Schematic diagram for the sample of original dsDNA sequence. (b) Asymmetric IV curve measured on the GNP corresponding to the configuration in (a). (c) Schematic diagram for the sample of reversed dsDNA sequence, where the two types of DNA strand are interchanged. (d) Asymmetric IV curve measured on GNP corresponding to the configuration in (c).

surface is biased negatively, the dsDNA molecules are in the standing state, and the current can only pass along the stacking base pairs of dsDNA and the linker. When the gold surface is biased positively, the dsDNA molecules will lie down and be closer to the gold surface. This may provide some leakage channel for the current to be directly passed to the gold surface. Thus, the dsDNA molecules appear more conductive when the sample surface is biased positively. In other words, it would appear more conductive when the dsDNA molecules are closer to the gold substrate. This is consistent with the different results for the IV curves in net repulsive and attractive forces. When a repulsive force is applied to the GNPs, it can press the dsDNA rods closer to the gold surface, creating a larger conductance than the attractive-force case.

To further test whether the conformation change is a possible explanation for the asym-

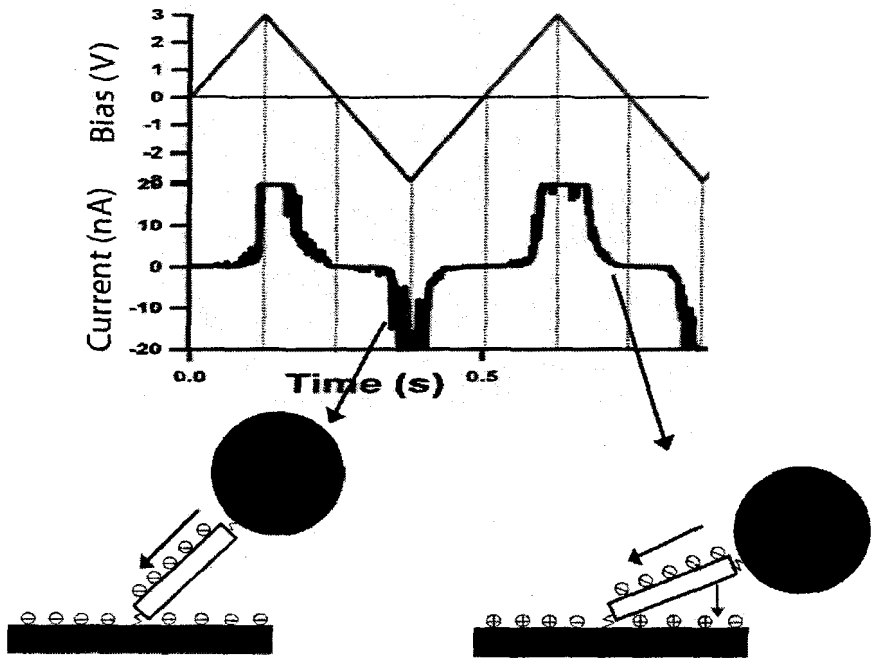

Figure 5.22: Diagram of the switching-mechanism hypothesis for the asymmetry in the I-V curves.

metry of IV curves, we investigated how the conductivity behavior changes with the orientation of the dsDNA molecules relative to the gold surface. Such changes can be achieved by the current-voltage/ force-distance (IV-FD) technique discussed in Chapter 4.3.3. This technique allows us to collect many cycles of IV curves at different positions along the FD curve. Three points along the approach are shown in the FD curve in Fig. 5.23 (points 1, 2, 3). At each point, 15 cycles of IV curves were measured. Voltage gaps were extracted from these curves, using the intersections between current curves and the voltage axis, and plotted as time events, as shown in Fig. 5.23(b), (c), and (d). Comparing the magnitude of voltage gaps at different points, one notices that the voltage gaps become smaller as the force pressing the GNP into the gold substrate increases from point (1) to (3). IV curves before point (1) show insulating behavior between $\pm$ 3 V, while IV curves after point (3) show a large, linear conductance. They have no voltage gaps any more. These results are consistent with the IV behavior at different forces, too. Thus, switching between standing and lying states is a possible explanation for the asymmetry of the IV curves.

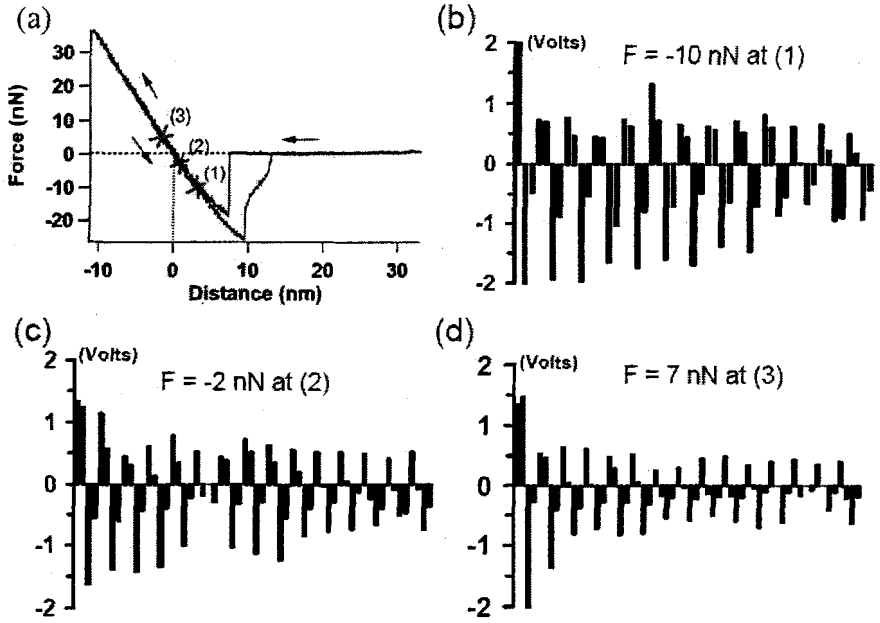

Figure 5.23: Analysis of the voltage gaps collected from the IV curves at different steps in a FD curve on the GNP. (a) Force-distance curve during which an AFM tip is brought to approach and retract to the GNP. (1), (2), and (3) are three points in the approaching process. (b) Voltage gaps collected from 15 cycles of IV curves at position (1), At lower forces, the IV curves always show insulating behavior between $\pm$ 3 V. (c) Voltage gaps collected from 15 cycles of IV curves at position (2). (d) Voltage gaps collected from 15 cycles of IV curves at position (3). At higher forces, the IV curves show a large linear conductance.

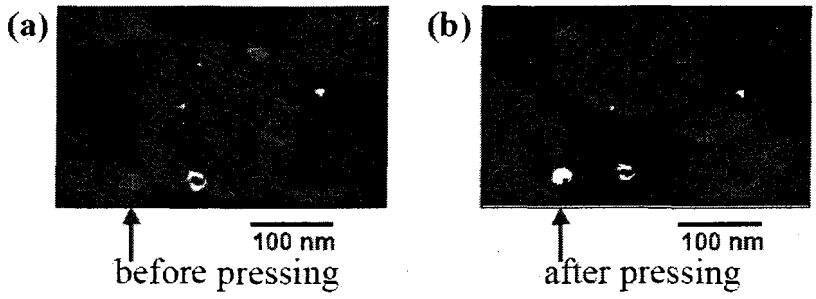

Figure 5.24: Current images under a 1.5 V tip bias. (a) Before a 35-45 nN force was applied on the GNP indicated by the arrow. (b) After the force was applied to the GNP.

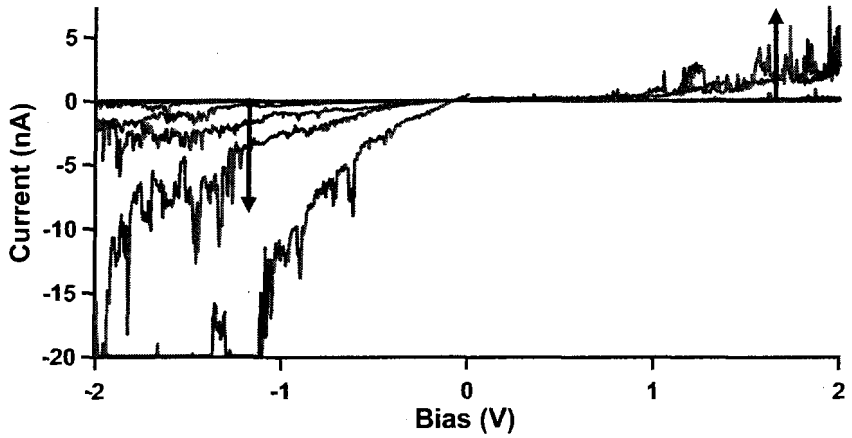

Figure 5.25: Current-voltage curves measured on the GNPs-dsDNA-Au sample (MCH modified) at postions without GNPs, using an attractive force ($\approx$ -15 nN). It shows leakage current after 3 cycles of IV. Arrows indicate that the currents increase with time.

We also investigated the effect on the GNP-dsDNA-Au structure from the force applied by the AFM probe. How rigid is the ideal configuration shown in Fig. 4.1 for conductivity measurements? Can a force change the structure and damage it? Figure 5.24 shows current images before and after a large force was applied on a GNP indicated by the arrow, using the constant-tip-bias scanning technique. The force applied to the GNP was 35–45 nN, which is even larger than the force at the extreme left-hand point of the FD curve in Fig. 5.23(a). Figure 5.24 shows the current through the GNP indicated by the arrow dramatically increased after the 35-45 nN force was applied to it. This indicates that the GNP could be pushed hard enough to attach to the gold substrate. Once made, the gold-gold contact between GNP and substrate is permanent, remaining even when the force is removed. Thus, after being pressed hard, the GNP appears to be much more conductive than other GNPs in Fig. 5.24(b).

Although the evidence we have presented so far is consistent with the switching mechanism, the switching mechanism would imply that current can pass directly to the gold surface and would mean that the ssDNA molecules are not functioning as a good insulator for the dsDNA molecules. The IV curves measured on ssDNA monolayer in Fig. 5.13, which show insulating behavior, would seem to rule out this possibility. However, we also

measured the electrical properties of ssDNA molecules on the GNP-dsDNA-Au samples at positions without GNPs. The current-voltage curves in Fig. 5.25 show that significant leakage current at lower bias is possible. This change of electrical behavior of ssDNA molecules may be caused by the hybridization of complementary strands or by other reasons. In our experiment, MCH molecules (with 6 carbon chains) are used to remove the non-specifically adsorbed ssDNA molecule and improve the hybridization between the ssDNA and complementary strands. This is supposed to help form the configuration shown in Fig. 4.1. On the other hand, it may also change the density of ssDNA molecules on the gold surface. We have not systematically studied how the MCH molecules will affect the electrical properties of the ssDNA monolayer, but thinner MCH monolayer is expected to be more conductive than a ssDNA monolayer. However, we found that the IV curves on GNPs are the same and have the same asymmetry, whether the GNP-dsDNA-Au samples are MCH-modified or not. The question of the origin of the leakage current needs further investigation. Moreover, the IV curves for leakage currents measured on the monolayer have asymmetries that differ from those measured on the GNPs (compare Fig 5.25 to Fig. 5.21(a) and (c)). Thus, we cannot yet decide whether leakage plays an important role in the IV curves on GNPs. If the entire IV curve were merely an effect of leakage current from the GNP through the monolayer, the interpretation of our results and those by the group of Naaman [78–80] would be called into question. Again further investigation is needed.

Chapter 6

Conclusion

In this thesis, we have studied the electrical properties of single DNA molecules for its possible applications to molecular electronics. The self-assembled-nanojunction method developed by Cui *et al.* for alkanedithiol molecules was first tested on our own system and then applied to measure the conductance of DNA molecules, using different techniques of conductive- atomic force microscopy.

First, we have developed a protocol for preparing atomically flat gold (111) substrates reproducibly, using thermal evaporation. The optimal values for the mica substrate temperature and evaporation rate have been determined to be 370 °C, and 0.6–0.7 nm/s, respectively. We also developed two annealing techniques (flame and furnace), which is very important for Au (111) reconstruction. Although the Au (111) surfaces can be contaminated by particles, the films are good enough to serve as substrates for self-assembled monolayers of ssDNA molecules.

Next, we studied the conductivity of octanedithiol molecules to confirm the work of Cui *et al.* Etch-pits were found in the self-assembled monolayers formed by octanethiol molecules. The close-packed monolayer shows insulating behavior, which is a requirement for the self-assembled-nanojunction method. For GNP-octanedithiol-Au samples, current images were obtained using a tip-bias-scanning technique with a contact-mode AFM. The current image shows that conduction increases dramatically when the tip scans over the GNPs. Thus, a chemical-bond contact using GNPs can greatly decrease the tunneling barrier for conduction measurements of single molecules. We also measured the current-voltages curves on different GNPs as well as their normalization factors, which are similar

to the results obtained by Cui *et al.*.

Using the method of self-assembled nanojunctions, we also studied the conductance of single dsDNA molecules. Like octanethiol, ssDNA molecules can form a close-packed insulating monolayer. The thickness of the ssDNA monolayer was measured to be 3–4 nm using an AFM technique combining contact and AC modes. After the ssDNA monolayer was incubated with complementary strands labeled by 10 nm GNPs, the dsDNA molecules formed by the hybridization of two strands were also labeled by the GNPs. Images of GNP-dsDNA-Au samples show that the height of the GNPs above the ssDNA monolayer is the size of the GNPs. This implies that the dsDNA molecules tilt relative to the sample surface. We also showed that the contact-mode-imaging with AFM is not suitable for the GNP-dsDNA-Au samples. Using a modified technique of constant-tip-bias scanning in AC mode, we obtained simultaneous topography and current images. They show a correlation between the positions with larger conduction in the current image and positions with GNPs in the topography image.

In contrast to the case of octanedithiol, the electrical properties measured on GNPs depend sensitively on the force applied by the AFM metal tip. If a repulsive force is applied, current-voltage curves show a large linear conductance. Thus, an attractive force is required for reproducible conductivity measurements. Asymmetry was also found in the IV curves measured on the GNPs in the preferred force range. The voltage gaps on the positive voltage side are always smaller than the ones on the negative side. We reversed the end connection of the two complementary strands, but the IV curve retains its shape. Thus, we concluded that the asymmetry of the IV curves is not due to the asymmetry of DNA sequences. We then proposed a "switching mechanism" between a "lying" and a "standing" state to explain the asymmetry in the IV curves. Analysis of the voltage gaps collected by the IV-FD technique shows a larger conduction for the configuration where dsDNA molecules tilt closer to the monolayer. Experiments using large forces also support this model. Thus, the switching mechanism is a possible explanation for the asymmetry.

Why does the self-assembled-nanojunction method work well for octanedithiol but less so for DNA molecules? It is useful to discuss some differences between the self-assembled nanojunction measurements on octanedithiol and dsDNA molecules. First, the ssDNA molecules are longer and softer than octanethiol molecules. Thus, they are tangled together to form a monolayer instead of "standing" separately and closely like the octanethiol

molecules on the metal substrates. Second, the dsDNA molecules are longer (9 nm) and more rigid than ssDNA molecules (2 nm persistence length). There is some freedom for the motion of these dsDNA rods, but octanedithiol molecules cannot move much because their length is the same as that of the octanethiol molecules. Third, DNA molecules have intrinsic negative charges on their strands, which can make the configuration more complicated. Finally, in the DNA experiments, we used larger GNPs than in the octanedithiol experiments. However, we believe that the larger GNPS do not produce any artifacts (beyond the potential for large lateral forces).

In the future, we need to find more direct evidence to test the hypothesis for a switching mechanism, Measuring the AFM-cantilever deflection during the IV measurements on the GNPs would be one way to directly correct currents with forces. We also need to investigate the origin of the leakage current and to systematically study how the MCH molecules and DNA hybridization would affect the electrical properties of ssDNA monolayer. The effects of the leakage current on the IV curves of GNPs also need to be studied. Furthermore, we can study the electrical properties of dsDNA molecules with different sequences and obtain more knowledge about the mechanisms of charge transport in DNA.

If the technical difficulties highlighted in this thesis can be resolved, there are a number of intriguing applications that can be imagined. For example, Fahlman *et al.* have demonstrated that two kinds of modified DNA structures known as "aptamers" can alter their conformation in the presence of analytes such as adenosine molecules and hence change their electrical conductivities [118]. If we can detect these conductivity changes with the self-assembled nanojunction method using c-AFM, we would have a biosensor for detecting the targeted molecular analyte. It would be an exciting application of DNA to molecular electronics.

Bibliography

[1] G. E. Moore, "Cramming more components onto integrated circuits", *Electronics* **38**, 4 (1965).

[2] V. Balzani, A. Credi, and M. Venturi, "The bottom-up approach to molecular-level devices and machines", *Chem. Eur. J.* **8**, 5525 (2002).

[3] A. hand, "High-index lenses push immersion beyond 32 nm", Semiconductor International (2006).

[4] Intel's 65nm process is founded upon an eight-layer metal technology incorporating copper, low-k dielectric materials and strained silicon. Intel has introduced processors with this 65 nm technology in summer 2006.

[5] D. G. Cahill, W. K. Ford, K. E. Goodson, G. D. Mahan, A. Majumdar, H. J. Maris, R. Merlin, and S. R. Phillpot, "Nanoscale thermal transport", *J. Appl. Phys* **93**, 793 (2003)

[6] R. L. Carroll and C. B. Gorman, "The genesis of molecular electronics", *Angew. Chem. Int. ED* **41**, 4378 (2002).

[7] Richard Feynman, "There's Plenty of Room at the Bottom", Annual meeting of the American Physical Society at the California Institute of Technology, December 29th, 1959.

[8] A. Aviram and M. A. Ratner, "Molecular rectifiers", *Chem. Phys. Lett.* **29**, 277 (1974)

[9] G. Cuniberti, G. Fagas, and K. Richter, *Introducing Molecular Electronics (Lecture Notes in Physics)*, Springer (2005).

[10] J. M. Tour, *Molecular Electronics (Commercial Insights, Chemistry Devices, Architecture and Processing)*, World Scientific (2003).

[11] C. Joachim, J. K. Gimzewski, and A. Aviram, "Electronics using hybrid-molecular and mono-molecular devices", *Nature* **408**, 541 (2000).

[12] G. Maruccio, R. Cingolani, and R. Rinaldi, "Projecting the nanoworld: concepts, results and perspectives of molecular electronics", *J. Mater. Chem.* **14**, 542 (2004).

[13] G. M. Whitesides and B. Grzybowski, "Self-assembly at all scales", *Science* **295**, 2418 (2002).

[14] S. Zhang, "Fabrication of novel biomaterials through molecular self-assembly", *Nature Biotech.* **21**, 1171 (2003).

[15] M. J. Robertson and R. J. Angelice, "Adsorption of aryl and alkyl isocyanides on powdered gold", *Langmuir* **10**, 1488 (1994).

[16] J. Texter and M. Tirrell, "Chemical Processing by self-assembly", *AICHE J.* **47**, 1706 (2001)

[17] W. Shenton, S. A. Davis, and S. Mann, "Directed self-assembly of nanoparticles into macroscopic materials using antibody-antigen recognition", *Adv. Mater.* **11**, 450 (1999).

[18] N. C. Seeman, "Nanotechnology and the double helix", *Scientific American* **June**, 65 (2004).

[19] J. R. Heath and M. A. Ratner, "Molecular electronics", *Physics Today* **56**, 43 (2003).

[20] R. Tsui, "Molecular electronics: the experimentalist view", *Nanotech.* **2**, 308 (2002).

[21] X. D. Cui, A. Primak, and S. M. Lindsay, "Reproducible measurement of single-molecule conductivity", *Science* **294**, 571 (2001).

[22] X. D. Cui, A. Primak, X. Zatate, J. Tomfohr, O. F. Sankey, A. L. Moore, T. A. Moore, D. Gust, L. A. Nagahara, and S. M. Lindsay, "Changes in the electronic properties of a molecule when it is wired into a circuit", *J. Phys. Chem. B* **106**, 8609 (2002).

[23] B. Q. Xu and N. J. Tao, "Measurement of single-molecule resistance by repeated formation of molecular junctions", *Science* **301**, 1221 (2003).

[24] R. M. Metzger, B. Chen, U. Holpfner, M. Lakshmikantham, D. Vuillaume, and G. J. Ashwell, "Unimolecular electrical rectification in hexadecylquinolinium tricyanoquinodimethanide", *J. Am. Chem. Soc.* **119**, 10455 (1997)

[25] P. Avouris, J. Appenzeller, R. Martel, and S. J. Wind, "Carbon nanotube electronics", *Proceedings of the IEEE* **91**, 1772 (2003).

[26] V. Derycke, R. Martel, J. Appenzeller, and Ph. Avouris, "Carbon nanotube inter- and intramolecular logic gates", *Nano Lett.* **1**, 453 (2001).

[27] A. Bachtold, P. Hadley, T. Nakanishi, and C. Dekker, "Logic circuits with carbon nanotube transistors", *Science* **294**, 1317 (2001).

[28] S. Iijima and T. Ichihashi, "Single-shell carbon nanotubes of 1-nm diameter", *Nature* **363**, 603 (1993).

[29] S. J. Tans, A. R. M. Verschueren, and C. Dekker, "Room-temperature transistor based a single carbon nanotube", *Nature* **393**, 49 (1998).

[30] M. A. Reed and T. Lee, *Molecular Nanoelectronics*, American Scientific Publishers (2003).

[31] T. Jenuwein and D. C. Allis, "Translating the histone code", *Science* **293**, 1074 (2001).

[32] E. Braun, Y. Eichen, U. Sivan, and G. Ben-Yoseph, "DNA-templated assembly and-electrode attachment of a conducting silver wire", *Nature* **391**, 775 (1998).

[33] C. R. Treadway, M. G. Hill, and J. K. Barton, "Charge transport through a molecular *pi*-stack: double helical DNA", *Chem. Phys.* **281**, 409 (2002).

[34] J. D. Watson and F. H. C. Crick, "A structure for Deoxyribose Nucleic Acid", *Nature* **171**, 737 (1953).

[35] M. D. Ventra and M. Zwolak, "DNA electronics", *Encyclopedia of Nanosci. and Nanotech.* **X**, 1 (2004).

[36] B. Yurke, A. J. Turberfield, A. P. Mills, F. C. Simmel, L. N. Jennifer, "A DNA-fuelled molecular machine made of DNA", *Nature* **406**, 605 (2000).

[37] B. Q. Xu, P. M. Zhang, X. L. Li, and N. J. Tao, "Direct conductance measurement of single DNA molecules in aqueous solution", *Nano Lett.* **4**, 1105 (2004).

[38] D. Dunlap, R. Garica, E. Schabtach, C. Bustamante, "Masking generates contiguous segments of metal-coated and bare DNA for scanning tunneling microscope imaging", *Proc. Natl. Acad. Sci. USA* **90**, 7652 (1993).

[39] P. J. de Pablo, F. Moreno-herrero, E. Artacho, "Absence of dc-conductivity in λ-DNA", *Phys. Rev. Lett.* **85**, 4992 (2000).

[40] A. J. Storm, J. V. Noort, S. d. Vries, and C. Dekker, "Insulating behavior for DNA molecules between nanoelectrodes at the 100 nm length scale", *Appl. Phys. Lett.* **79**, 3881 (2001).

[41] D. Porath, A. Bezryadin, S. d. Vries, C. Dekker, "Direct measurement of electrical transport through DNA molecules", *Nature* **403**, 635 (2000).

[42] A. Rakitin, P. Aich, C. Papadopoulos, and J. M. Xu, "Metallic conduction through engineered DNA: DNA nanoelectronic building blocks", *Phys. Rev. Lett.* **86**, 3670 (2001).

[43] H. Watanabe, C. Manabe, K. Shimotani, and M. Shimizu, "Single molecule DNA device measured with triple-probe atomic force microscope", *Appl. Phys. Lett.* **79**, 2462 (2001).

[44] H. W. Fink, C. Schoenenberger, "Electrical conduction through DNA molecules", *Nature* **398**, 407 (1999).

[45] L. T. Cai, H. Tabata, and T. Kawai, "Self-assembled DNA networks and their electrical conductivity", *Appl. Phys. Lett.* **77**, 3105 (2000).

[46] K. H. Yoo, D. H. Ha, J. -O. Lee, J. W. Park, J. Kim, J. J. Kim, H. -Y. Lee, T. Kawai, and H. Y. Choi, "Electrical conduction through poly(dA) · poly (dT) and poly(dG) · poly(dC) DNA molecules", *Phys. Rev. Lett.* **87**, 198102 (2001).

[47] A. Y. Ksumov, M. Kociak, S. Gueron, B. Reulet, and H. Bouchiat, "Proximity-induced superconductivity in DNA", *Science* **291**, 280 (2001).

[48] P. F. Schwab, M. D. Levin, and J. Michl, "Molecular rods. 1. simple axial rods", *Chem. Rev.* **99**, 1863 (1999).

[49] S. Datta, " Electronic transport in mesoscopic systems", *Cambridge University Press*, 1995.

[50] E. Emberly and G. Kirczenow, "Electrical conductance of molecular wires", *Nanotech.* **10**, 285 (1999).

[51] M. Buttiker, "Coherent and sequential tunneling in series barriers", *J. Res. Develop.* **32**, 63 (1998).

[52] J. G. Simmons, *DC conduction in thin films*, Mills and Boon Ltd, London (1971).

[53] R. L. McCreery, " Molecular electronics junctions" , *Chem. Mater.* **16**, 4477 (2004).

[54] D. J. Wold and C. D. Fribie, "Fabrication and characterization of metal-molecule-metal junctions by conducting- probe atomic force microscopy", *J. Am. Chem. Soc.* **123**, 5549 (2001).

[55] K. Slowinski, K. U. Slowinska, M. J. Majda, "Electron tunneling across hexadecanethiolate monolayers on mercury electrodes: reorganization energy, structure, and permeability of the alkane/water interface", *J. Phys. Chem. B* **103**, 8544 (1999).

[56] D. B. Hall and J. K. Barton, "Sensitivity of DNA-mediated electron transfer to the intervening pi-Stack: a Probe for the integrity of the DNA base stack", *J. Am. Chem. Soc.* **119**, 5045 (1997).

[57] S. J. Bending and M. R. Beasley, "Transport process via localized states in thin α-Si tunnel barriers", *Phys. Rev. Lett.* **55**, 325 (1985).

[58] H. Sies, W. A. Schulz, S. Steenken, "Adjacent guanines as preferred sites for strand breaks in plasmid DNA irradiated with 193 nm and 248 nm UV laser light", *Photochem. Photobiol. B* **32**, 97 (1996).

[59] C. A. M. Seidel, "Nucleobase-specific quenching of fluorescent dyes. 1. nucleobase one-electron redox potentials and their correlation with static and dynamic quenching efficiencies", *J. Phys. Chem.* **100**, 5541 (1996).

[60] H. Sugiyama and I. Saito, "Theoretical studies of GG-specific photocleavage of DNA via electron transfer: significant lowering of ionization potential and 5'-localization of HOMO of stacked GG bases in B-form DNA", *J. Am. Chem. Soc.* **118**, 7063 (1996).

[61] G. B. Schuster and U. Landman, "The mechanism of long-distance radical cation transport in duplex DNA: lon-gated hopping of polaron-like distortions", *Top. Curr. Chem.* **236**, 139 (2004).

[62] B. Giese and A. Biland, "Recent developments of charge injection and charge transfer in DNA", *Chem. Commun.* **7**, 667 (2002).

[63] P. Thordarson, R. Atkin, W. H. J. Kalle, G. G. Warr, and F. Braet, "Development in using scanning probe microscopy to study molecules on surface – from thin films and single-molecule conductivity to drug-living cell interactions", *Aust. J. Chem.* **59**, 359 (2006).

[64] M. Taniguchi and T. Kawai, "DNA electronics", *Phys. E* **33**, 1 (2006).

[65] Y. Xia, J. A. Rogers, K. E. Paul, and G. M. Whitesides. "Unconventional methods for fabricating and patterning nanostructures", *Chem. Rev.* **99**, 1823 (1999)

[66] A. F. Morpurgo, C. M. Marcus, and D. B. Robinson, "Controlled fabrication of metallic electrodes with atomic separation", *Appl. Phys. Lett.* **74**, 2084 (1999).

[67] J. Fujita, Y. Ohnishi, Y. Ochiai, and S. Matsuil, "Ultrahigh resolution of calixarene negative resist in electron beam lithography", *Appl. Phys. Lett.* **68**, 1297 (1996).

[68] M. T. Cygan, T. D. Dunbar, J. J. Arnold, L. A. Barmm, J. M. Tour, and P. S. Weiss, "insertion, conductivity, and structures of conjugated organic oligomers in self-assembled alkanethiol monolayers on Au (111)", *J. Am. Chem. Soc.* **120**, 2721 (1998).

[69] S. Lindsay, "Single-molecule electronic measurements with metal electrodes", *J. Chem. Ed.* **82**, 727 (2005).

[70] D. Porath, G. Cuniberti, and R. D. Felice, " Charge transport in DNA-based devices", *Top. Curr. Chem.* **237**, 183 (2004).

[71] J. Jortner and M. Bixon, "Charge transfer and transport in DNA", *Proc. Natl. Acad. Sci. USA* **95**, 12759 (1998).

[72] B. Giese, "Long-distance charge transport in DNA: the hopping mechanism", *Acc. Chem. Res.* **33**, 631 (2000).

[73] R. G. Endres, D. L. Dox, and R. P. Singh, "Colloquium: The quest for high-conductance DNA", *Rev. Mod. Phys.* **76**, 195 (2004).

[74] J. Bechhoefer and D. Sen, "Comment on insulating behavior of λ-DNA on the micron scale", *Phys. Rev. Lett.* **93**, 239801 (2004).

[75] L. Cai, H. Tabata, and T. Kawai, "Probing electrical properties of oriented DNA by conducting atomic force microscopy", *Nanotech.* **12**, 211 (2001).

[76] Y. Zhang, R. H. Austin, J. Kraeft, E. C. Cox, N. P. Ong, "Insulating behavior of λ-DNA on the micron scale", *Phys. Rev. Lett.* **89**, 198102 (2002).

[77] K. W. Hipps, "Molecular electronics: it's all about contacts", *Science* **294**, 536 (2001).

[78] C. Nogues, S. R. Cohen, S. S. Daube, and R. Naaman, "Electrical properties of short DNA oligomers characterized by conducting atomic force microscopy", *Phys. Chem. Chem. Phys* **6**, 4459 (2004).

[79] C. Nogues, S. R. Cohen, S. Daude, N. Apter, and R. Naaman, "Sequence dependence of charge transport properties of DNA", *J. Phys. Chem. B* **110**, 8910 (2006).

[80] H. Cohen, C. Nogues, R. Naaman, and D. Porath, "Direct measurement of electrical transport through single DNA molecules of complex sequence", *Proc. Natl. Acad. Sci. (PNAS)*, **102**, 11589–11593 (2005).

[81] C. Kittel, "Introduction to solid state physics: Seventh Edition", *John Wiley and Sons, Inc., New York, USA*, 673 (1996).

[82] J. C. Love, L. A. Estroff, J. K. Kriebel, R. G. Nuzzo, and G. M. Whitesides, "Self-assembled monolayers of thiolates on metals as a form of nanotechnology", *Chem. Rev.* **105**, 1103 2005.

[83] C. Nogues, M. Wanunu, "A rapid approach to reproducible, atomically flat gold films on mica", *Surf. Sci.* **573**, 383 (2004).

[84] U. Hopfner, H. Hehl, and L. Brehmer, "Preparation of ordered thin gold films", *Appl. Surf. Sci.* **152**, 259 (1999).

[85] J. A. DeRose, T. Thundat, L. A. Nagahara, and S. M. Lindsay, "Gold grown epitaxially on mica: conditions for large area flat faces", *Surf. Sci.* **256**, 102 (1991).

[86] J. Hwang, M. A. Dubson, "Atomically flat gold films grown on hot glass", *J. Appl. Phys* **72**, 1852 (1992).

[87] M. Levlin, A. Laakso, H. E. Niemi, and P. Hautojarvi, "Evaporation of gold thin films on mica: effect of evaporation parameters", *Appl. Surf. Sci.* **115**, 31 (1997).

[88] C. A. Widrig, C. A. Alves, and M. D. Porter, "scanning tunneling microscopy of ethanethiolate and n-octadecanethiolate monolayers spontaneously adsorbed at gold surfaces", *J. Am. Chem. Soc.* **113**, 2805 (1991).

[89] M. H. Dishner, M. M. Ivey, S. Gorer, J. C. Hemminger, and F. J. Feher, "Preparation of gold thin films by epitaxial growth on mica and the effect of flame annealing", *J. Vac. Sci. Technol. A* **16**, 3295 (1998).

[90] Integrated DNA Technologies, Toronto, Canada. http://www.idtdna.com.

[91] Z. H. Liu, N. M. D. Brown, "Studies using AFM and STM of the correlated effects of the deposition parameters on the topography of gold on mica", *Thin Solid Films* **300**, 84 (1997).

[92] M. S. Xu, R. G. Endres, S. Tsukamoto, M. Kitamura, S. Ishida, Y. Arakawa, "Conformation and local environment dependent conductance of DNA molecules", *Small* **1**, 1168 (2005).

[93] (1) RTD sensor (thermocouple) is a 4-wire, 100 Ω, 1/8" × 2' long, from Valax Manufacturing Inc., Delta, BC, Canada (2) Digital multimeter is Keithley model 2001 from Keithley Instruments Inc.(http://www.keithley.com). (3) Gold was obtained from a commercial bullion dealer, the purity levels are the same as the gold sold by scientific supply houses, at prices that are 5 to 6 times cheaper. (4) Evaporation boat is the type of EVS2BAOMO from Kurt J. Lesker company (www. lesker.com). (5) Quartz crystal (60 MHz, gold), LI008010G10, Kurt J. Lesker company (www. lesker.com).

[94] T. M. Herne and M. J. Tarlov, "Characterization of DNA probes immobilized on gold surfaces", *J. Am. Chem. Soc.* **119**, 8916 (1997).

[95] E. Meyer, H. J. Hug, and R. Bennewitz, "Scanning Probe Microscopy: The Lab on a Tip", *Springer*, (2004).

[96] F. J. Biessibl, "Advances in atomic force microscopy", *Rev. Mod. Phys.* **75**, 949 (2003).

[97] J. N. Israelachvili, "Intermolecular and surface forces", *Academic Press*, (1991).

[98] MFP-3D atomic force microscope installation and operation manual, Asylum Research.

[99] J. L. Hutter and John Bechhoefer, "Calibration of atomic-force microscope tips", *Rev. Sci. Instrum.* **64**, 1868 (1993).

[100] A. Alessandrini and P. Facci, "AFM: a versatile tool in biophysics", *Meas. Sci. Technol.* **16**, R65 (2005).

[101] R. Howland and L. Benatar, "A Practical Guide to Scanning Probe Microscopy", *Park Scientific Instruments*, (1993).

[102] PSD-UV-Benchtop UV/Ozone cleaner, Novascan Technologies, Inc., Ames, IA, USA.

[103] W. Kern, "Handbook of seminconductor wafer cleaning technology (science, technology, and applications)", *Noyes Publications*, New Jersey, USA (1993).

[104] Contact Mode-PtIr5 coating, NanoWorld AG, Switzerland.

[105] NSC19/Ti-Pt, Micromasch USA, Wilsonville, OR, USA.

[106] Part NO.805.ASY.CAFM, Asylum Research, Santa Barbara, CA, USA.

[107] G. Yang and G. Liu, "New insights for self-assembled monolayers of organothiols on Au (111) revealed by scanning tunneling microscopy", *J. Phys. Chem. B* **107**, 8746 (2003).

[108] G. E. Poirier, "Characterization of organosulfur molecular monolayer on Au (111) using scanning tunneling microscopy", *Chem. Rev.* **97**, 1117 (1997).

[109] K. Edinger, A. Golzhauser, K. Demota, Ch. Woll, and M. Grunze, "Formation of self-assembled monolayers of n-alkanethiols on gold: a scanning tunneling microscopy study on the modification of substrate morphology", *Langmuir* **9**, 4 (1993).

[110] G. E. Poirier, "Mechanism of formation of Au vacancy islands in alkanethiol monolayers on Au (111)", *Langmuir* **13**, 2019 (1997).

[111] R. Georgiadis, K. P. Peterlinz, and A. W. Peterson, "Quantitative measurements and modeling of kinetics in nucleic acid monolayer films using SPR spectroscopy", *J. Am. Chem. Soc.* **122**, 3166 (2000).

[112] A. B. Steel, R. L. Levicky, T. M. Herne, and M. J. Tarlov, "Immobilization of nucleic acids at solid surfaces: effect of oligonucleotide length on layer assembly", *Biophys. J.* **79**, 975 (2000).

[113] J. H. Watterson, P. A. E. Piunno, C. C. Wust, and U. J. Krull, "Effects of oligonucleotide immobilization density on selectivity of quantitative transduction of hybridization of immobilized DNA", *Langmuir* **16**, 4984 (2000).

[114] A. Csaki, R. Moller, W. Straube, J. M. Kohler, and W. Fritzsche, "DNA monolayer on gold substrates characterized by nanoparticle labeling and scanning force microscopy", *Nucl. Acids Res.* **29**, e81 (2001).

[115] C. Bustamante, S. B. Smith, J. Liphardt and D. Smith, "Single-molecule studies of DNA mechanics", *Curr. Opin. Struct. Biol.* **10**, 279 (2000).

[116] U. Rant, K. Arinaga, S. Fujita, N. Yokoyama, G. Abstreiter, and M. Tornow, "Dynamic electrical switching of DNA layers on a metal surface", *Nano Lett.* **4**, 2441 (2004).

[117] S. O. Kelley, J. K. Barton, N. M. Jackson, L. D. McPherson, A. B. Potter, E. M. Spain, M. J. Allen, and M. G. Hill, "Orienting DNA helices on gold using applied electric fields", *Langmuir* **14**, 6781 (1998).

[118] R. P. Fahlman and D. Sen, "DNA conformational switches as sensitive electronic sensors of analytes". *J. Am. Chem. Soc.* **124**, 4610 (2002).